Interface Modifications for Applications in Organic and Hybrid Photovoltaics

Katherine A. Mazzio

A dissertation

submitted in partial fulfillment of the

requirements for the degree of

Doctor of Philosophy

University of Washington

2014

Reading Committee:

Christine K. Luscombe, Chair

Peter J. Pauzauskie

Lih Y. Lin

Xiaohu Gao

Program Authorized to Offer Degree:

Materials Science and Engineering

University of Washington

Abstract

Interface Modifications for Applications in Organic and Hybrid Photovoltaics

Katherine A. Mazzio

Chair of the Supervisory Committee:

Professor Christine K. Luscombe

Department of Materials Science and Engineering

Considerable research has been conducted in the area of organic photovoltaics due to several intrinsic advantages, including their high throughput solution processability, light weight, and their applicability on flexible substrates. Product development has been limited, however, due to the low mobilities and short exciton diffusion lengths of organic materials relative to inorganic materials used for photovoltaics. In this dissertation, we look at interfacial phenomena in attempt to control the charge transport dynamics in different parts of photovoltaic systems. The first chapter provides an overview of the field of organic photovoltaics, including their benefits, operating procedures, and a brief history of materials and device development. Chapter 2 examines some donor-acceptor small molecules as the electron donors in all organic bulk heterojunction solar cells with soluble fullerene derivatives as the electron

acceptors. The donor-acceptor small molecules are unique because their energy levels agree well with the theoretical optimal HOMO and LUMO energy levels required for high efficiency organic photovoltaics. Even with energy level matching, however, we found that we were only able to obtain modest device efficiencies due to the formation of large domains that are greater than the exciton diffusion length and result in large interfacial areas. In chapter 3 we examine some of the optical, physical, and charge transport properties of a series of fully conjugated brush copolymers that are comprised of a carbazole-diketopyrrolorpyrrole donor-acceptor backbone copolymerized with different lengths of poly(3-hexylthiophene) pendant chains. It was found that there was a sufficient break in conjugation between the two copolymers such that the absorbance characteristics of both could be realized independently. In addition, the physical and charge transport properties could be tuned to primarily show influence from either the ambipolar low band gap backbone or the p-type pendant chains. Chapter 4 examines the synthesis of poly(3-methylthiophene) via surface initiated Kumada catalyst transfer polymerization from indium tin oxide where it was found that the thickness of the polymer layers could be controlled by controlling the monomer concentration in solution. These films proved to be robust interface layers that exhibit work functions that are tunable by electrochemical doping; when in the doped state, they show fast electron dynamics, while in the neutral state, they may be applicable as electron blocking layers for organic photovoltaics. In chapter 5, a new method for the in-situ functionalization of CdSe quantum dots with π-conjugated ligands during synthesis is presented. This technique is useful for controlling the composition of the surface of colloidal CdSe quantum dots when traditional ligand exchange processes prove difficult. This synthetic

technique is then used in chapter 6 to functionalize CdSe nanocrystals with poly(3-hexylthiophene) in an attempt to promote good interfacial charge transport properties for use in hybrid photovoltaics. The photophysics of a series of these hybrid CdSe/polymer materials were investigated by steady state and time-resolved spectroscopies, and ultimately it was found that there is a strong propensity for fluorescence resonance energy transfer between the two materials owing to their intimate contact, good resonance, and large spectral overlap. Finally, a brief future work section is presented that is required to wrap up the study of the photophysical processes for these hybrid materials.

Table of Contents

Figures

Schemes

Tables

Equations

Chapter 1: Introduction to Organic Photovoltaics

1.1 The need for alternative energy resources

1.1.1 Current status of PV technologies

Interest in renewable energy resources has been gaining momentum in an effort to alleviate the global demand for fossil fuels due to their decreased availability and a greater understanding of the long-term effects of CO_2 and other green house gas emissions. Global energy consumption is predicted to increase from approximately 17 TW in 2010 to approximately 27 TW by 2040, with the majority of projected demand coming from developing countries.[4] While improvements in energy efficiency and conservation can help improve the global energy outlook by reducing the demand for fossil fuels, it is clear that investments in alternative energy resources are paramount to meeting future global energy needs. Photovoltaics are an established, though under-utilized, method for electricity generation. Figure 1 shows the certified best efficiencies for a variety of photovoltaic technologies, with championship efficiencies for inorganic multijunction cells under solar concentration exceeding 44%, and with single crystalline silicon and multicrystalline silicon cells exceeding 25% and 20% efficiency, respectively.[5] While these high efficiencies are promising, this is not the only metric for determining the potential value of these technologies. Perhaps the most important factor for the wide scale deployment of these technologies is their cost. These inorganic photovoltaic technologies overwhelmingly have production limitations due to direct competition for materials with the microelectronics industry, materials toxicity, high production costs due to the amount of material required for these devices and vacuum

processing required for production, in addition to their high installation costs, which are directly linked to the weight of these cells. Organic photovoltaics based on π-conjugated polymers and small molecules have seen increasing interest in recent years as an alternative to inorganic photovoltaics because they offer a suite of promising properties. These include favorable electronic properties and component versatility, as well as low production and installation costs because they promise to be light-weight, solution processable, and applicable for large area and flexible devices.

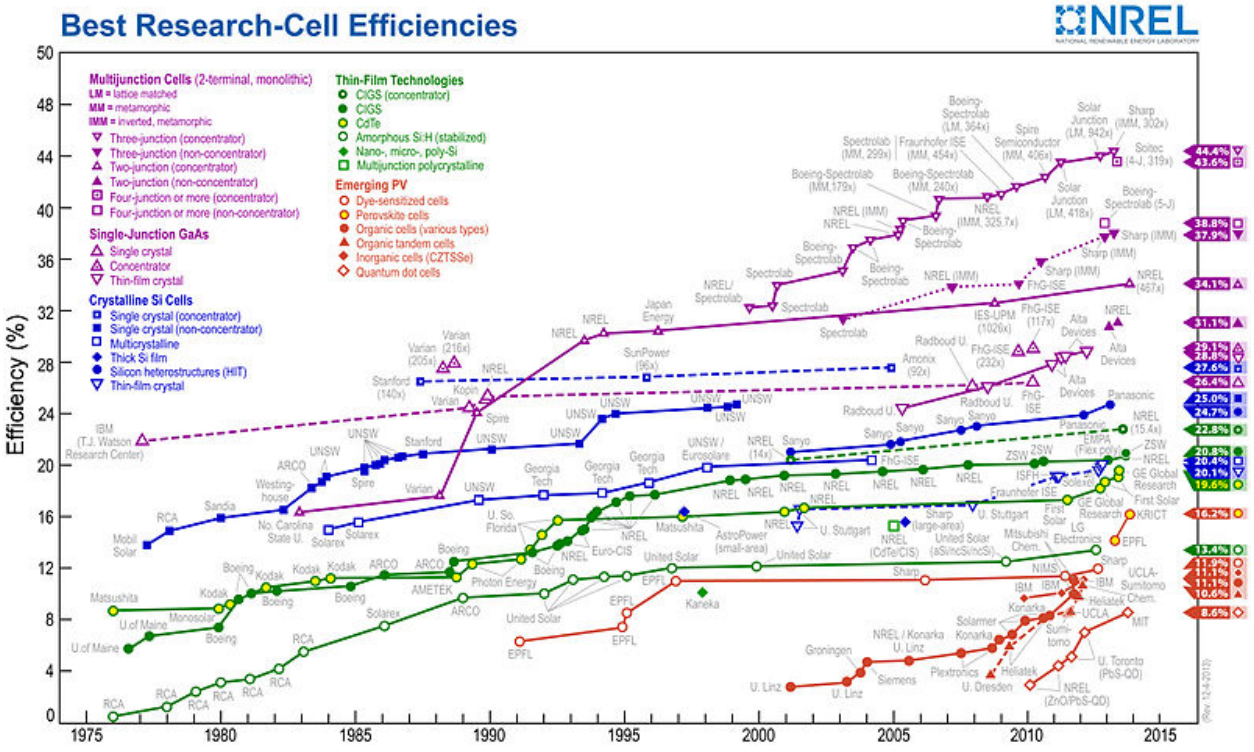

Figure 1: Certified best power conversion efficiencies over time for a variety of photovoltaic technologies, provided by NREL.

1.1.2. Levelized Cost of Energy

Two metrics that are useful for evaluating and comparing these different

photovoltaic technologies, in conjunction with their power conversion efficiency, include key economic indicators such as their Levelized Cost of Energy (LCOE) and their energy payback time (EPBT). The LCOE is a metric used to compare how cost-effective different types of energy sources are, with units of ¢/kWh. It is determined by the ratio of the total life cycle cost, including all costs associated with construction, operation, maintenance, and decommission, and the total amount of energy produced over the lifetime of the system, as outlined according to equation 1.

$$LCOE = \frac{life\ cycle\ cost}{energy\ produced} \quad (1)$$

Factors that affect the LCOE include the efficiency, cost, and lifetime of the solar cell, along with hardware and soft costs such as labor and overhead. The LCOE is highly dependent on public policy such as investment tax credits that can drive the LCOE of various alternative energy sources down to costs on the order of traditional fossil fuel sources. Due to the relative maturity of the various inorganic solar cell technologies, their LCOEs are not projected to drop in price enough to compete directly with traditional fossil fuel energy sources, and it is clear that there is much improvement needed.[6] Emerging organic solar cell technologies have the benefits of high throughput manufacturing and low cost materials, which will dramatically reduce their manufacturing costs. In addition, their light weight and flexibility will streamline module installation, eliminate racking, and reduce shipping costs, making them poised to exhibit dramatically reduced LCOEs that will be competitive, if not lower than those of traditional fossil fuel sources.

1.1.3 Energy Payback Time

The EPBT of a solar cell is the time required for a device to produce an amount of energy that is equivalent to the sum of the energy required to both manufacture and decommission that device. The EPBT has been investigated for various inorganic PV technologies available on the market, and several studies have also looked at potential EPBTs for organic PV.[7] These calculations determine the EPBT as the ratio of the energy consumed over the life of the module and the energy that it generates over its lifetime. In order to do so, several assumptions must be made, including an average global insolation of approximately 1700 kWh/m^2, and an average lifetime of 15 years for OPV, which is lower than the 20-30 year lifetime assumed for inorganic PV. These calculations also take into account energy efficiencies for each module, which are chosen to reflect devices that are currently at the manufacturing stage for inorganic photovoltaics, and forecasted efficiencies for organic photovoltaics that are not currently on the market. For mature technologies, such as mono- and poly-crystalline silicon photovoltaics, the EPBT has been estimated to be on the order of years.[8] In contrast, the EPBT for organic photovoltaics, while being more difficult to predict due to their nature as an emerging technology, has been estimated to be on the order of days.[7] For more specific details regarding the estimation of EPBT, the interested reader is referred to a recent article by Espinosa *et al*.[7] While the forecasted efficiencies for OPV are quite low, they still have a short EPBT relative to their inorganic counterparts. This is a result of the same benefits discussed for reducing their LCOE: high throughput processing methods and reduced material consumption required during the manufacture of OPV relative to inorganic PV.

At present, OPV modules exhibit prohibitively low efficiencies and have issues associated with module stability and large scale materials manufacturing that need to be addressed prior to taking advantage of their many inherent benefits. Historically, increases in OPV device performance have been accompanied by breakthroughs in materials design or materials processing. In this introduction, we attempt to examine the advancement of the OPV field from an historical perspective in order to discuss issues that need to be addressed prior to successful commercialization of OPV.

1.2 Operating Principles of organic electronics

1.2.1 Photovoltaic process (overview)

The photovoltaic process for OPV differs from that in inorganic photovoltaics. With

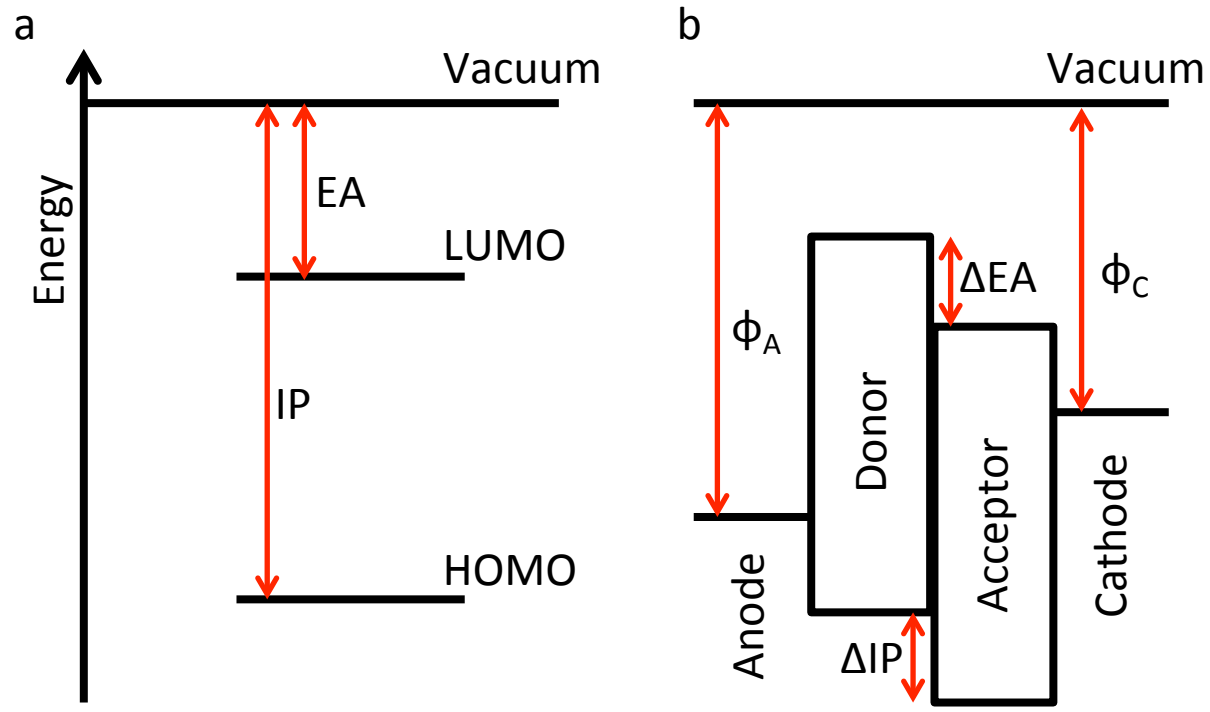

Figure 2: Basic energy level diagrams. a) of an organic semiconductor and b) of a heterojunction solar cell.

inorganic materials, the absorption of photons with energies greater than the band gap results in the direct generation of free charge carriers (electrons and holes) that are able to separate at a p-n junction, where they may then diffuse under an externally applied electric field to their respective electrodes. Organic materials characteristically have a much lower dielectric constant than their inorganic counterparts, which prevents screening of the coulombic attraction between electrons and holes. This results in the generation of excitons, or coulombically bound electron/hole pairs upon photoabsorption, rather than free charge carriers. In order for these excitons to be useful in doing work through an external circuit, they must first be dissociated into free charge pairs. If the exciton is not able to dissociate within the lifetime of the exciton, the exciton will decay back to its ground state, resulting in the loss of that absorbed energy. In OPVs, exciton dissociation relies on the presence of a two-component system containing an electron donor and an electron acceptor that is similar to that of a p-n junction.[9] The electron donor is typically characterized by a large ionization potential, while it is desirable for the electron acceptor to have a high electron affinity.

Figure 2 provides schematics of basic energy level diagrams used to describe OPV. The ionization potential (IP) of a neutral organic material is the energy required to remove an electron from its highest occupied molecular orbital (HOMO) to vacuum. The electron affinity (EA) is a measure of a materials ability to act as an electron acceptor, and is often approximated as the LUMO level relative to vacuum of an organic material. The HOMO/LUMO gap, or band gap, of a conjugated organic material is the minimum energy required to promote an electron from its HOMO to its LUMO. Figure 2b shows representative work functions for anode and cathode materials in OPV, in addition to

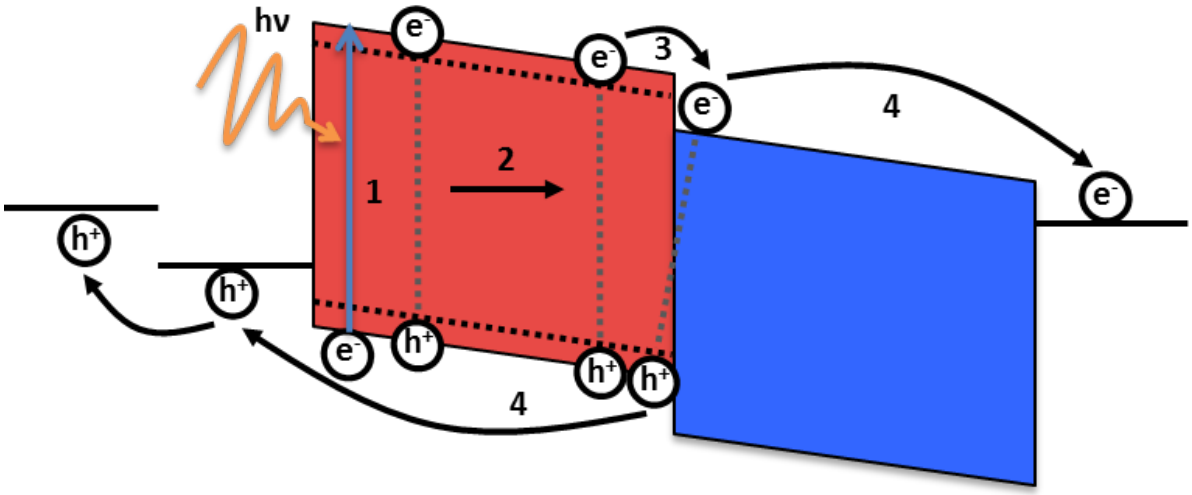

Figure 3: Schematic of the operating principles of OPV.

highlighting energetic offsets between donor and acceptor HOMO (ΔIP) and LUMO (ΔEA) levels, which are important for understanding charge transport mechanisms. Figure 3 provides a simplified schematic of the photovoltaic process for OPV that is broken down into four steps. Upon photoabsorption, the first step, an electron can be excited from the donor highest occupied molecular orbital (HOMO) to its lowest unoccupied molecular orbital (LUMO), forming an exciton. This exciton must then diffuse to a donor/acceptor interface via a chemical potential gradient (step 2) where the electron can transfer to the LUMO of the acceptor material, forming a charge transfer (CT) complex, which will be favorable to occur when the energy difference between the donor LUMO and the acceptor LUMO is greater than the binding energy of the exciton. This energy difference is typically on the order of a couple hundred meV, depending on the materials employed, and any absorbed energy in excess of this exciton binding energy will be lost in these systems. This is reflected by the theoretical maximum attainable voltage output of these cells being dictated by the difference between the

donor HOMO and acceptor LUMO to a first approximation, and represents an important materials design consideration. The CT state can be described as having charge carriers that are coulombically bound across a donor/acceptor interface (referred to as geminate pairs), such that the energy of the CT state is highly dependent on the Coulombic attraction of the charge carriers, and in turn, on the distance that separates these species. The CT state can become a charge separated (CS) state, or free charge carriers, as step 3 in the photovoltaic process if the distance between the electron and hole becomes greater than the coulomb capture radius. However, if unable to escape the coulomb capture radius, the geminate pair will recombine across the donor/acceptor interface (referred to as geminate recombination), which is a competing process with free charge carrier generation and constitutes another loss mechanism in these devices. Any dissociated charges can then be transported through p-type or n-type domains to the electrodes, with holes being collected at the anode and electrons being collected at the cathode in step 4, where they can be used to do work in an external circuit. The final and leading loss mechanism in OPV is that of charge recombination, whereby free charge carriers recombine with unassociated charge carriers within a device, a process that is in direct competition with charge transport to the electrodes. A key objective in OPVs is the minimization of energy and charge loss processes in order to enhance the efficiency of devices. While the exciton dissociation process is actually far more complex than depicted, these simplified schematics are useful for generating a conceptual understanding of the photophysical processes occurring in OPVs.

1.2.2 Characterization of PV process

All photovoltaics are photodiodes, which are capable of generating current or voltage from incident light when operating in reverse bias (where the voltage at the anode is higher than that at the cathode) and can be described according to the equivalent circuit model, as shown schematically in Figure 4a. In general, when a forward bias is applied to a diode, there is an exponential increase in current flow, whereas with the application of a reverse bias, there is a small saturation current that can be approximated as linear up to a large reverse bias voltage where breakdown will occur. In the dark, almost no current flows until large forward bias, and under ideal circumstances the applied bias is related to the current flow according to equation 2.

$$J_{dark} = J_0 \left(e^{\frac{qV}{k_B T}} - 1 \right) \quad (2)$$

where J_{dark} is the photodiode dark current density (or the current flow through the device), J_0 is the reverse saturation current density (a constant), q is the elementary electron charge, V is the applied bias voltage, k_B is Boltzmann's constant, and T is the absolute temperature.

When under illumination, the J-V curve shifts down in an amount equal to the photocurrent, J, and the device can generate power. The maximum power point (MP) is the location on the J-V curve where the product of the current density and voltage is maximized. Under short circuit conditions (J_{SC}), the current flow is at a maximum and there is no applied bias. The J_{SC} is primarily dependent on factors related to the efficiencies of each stage in the photovoltaic process, including the efficiency of light

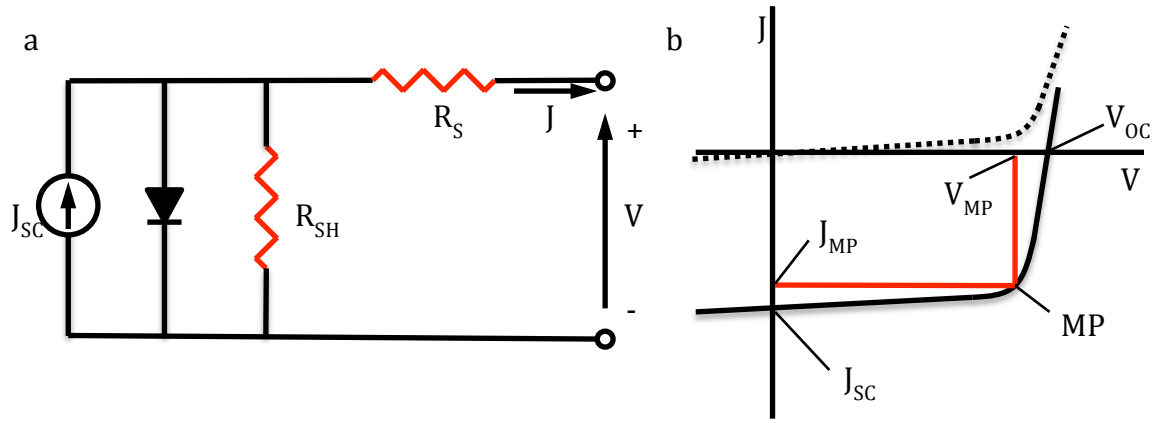

Figure 4: a) Equivalent circuit model for OPV and b) Current density-voltage (*J-V*) curves of an organic solar cell (dark, - - -; illuminated, -). The characteristic intersections with the abscissa and ordinate are the open circuit voltage (V_{OC}) and the short circuit current density (J_{SC}), respectively.

absorption, exciton diffusion, exciton dissociation, charge transport, and charge collection. Open circuit conditions (V_{OC}) characteristically have no current flow, and this is the point of maximum electrochemical potential of the cell. The V_{OC} in inorganic photovoltaics is determined by the difference in the quasi Fermi levels of the p- and n-type junctions, while in organic photovoltaics, this value has been found to be dependent to a first approximation on the difference between the HOMO of the donor and the LUMO of the acceptor. Figure 4b provides a schematic of the current density-voltage (*J-V*) response of a photodiode operating in the dark (dashed line) and under illumination (solid line).

The primary figure of merit for solar cells is the power conversion efficiency, η_e, which is the ratio of the maximum electrical power generated by the device to the total incident optical power, P_{in}, and is defined according to equation 3.

$$\eta_e = \frac{Pm}{Pin} \times 100\% = \frac{Voc * Isc * FF}{Pin} \times 100\% \qquad (3)$$

where P_m is the maximum generated power, P_{in} is the total incident power, and *FF* is the Fill Factor, defined by equation 4.

$$FF = \frac{Jmp*Vmp}{Jsc*Voc} \quad (4)$$

where J_{MP} is the current density at the maximum power point and V_{MP} is the voltage at the maximum power point. The *FF* gives an indication of how easily charges can be removed from a cell and is often described as the "squareness" of the J-V curve, and in the ideal case will have a value of unity. There are several factors that can affect the *FF* of a solar cell and they often interact in complex ways. The series and shunt resistances are two important factors that affect the fill factor of a cell. When these are taken into account, the equivalent circuit model can mathematically describe the total current according to Kirchoff's law for current, as defined by equation 5

$$J = J_{SC} - J_{dark} - J_{SH} = J_{SC} - J_0\left(e^{\frac{q(V+JR_S)}{k_BT}} - 1\right) - \frac{V+JR_S}{R_{SH}} \quad (5)$$

where J_{SH} is the shunt current, R_S is the series resistance, and R_{SH} is the shunt resistance. R_S accounts for bulk and interface resistances for each layer of the cell and the contacts. It is usually determined by taking the slope of the *J-V* curve around V_{OC}, and under ideal circumstances R_S will be zero, allowing all photocurrent to flow through the diode. R_{SH} is a result of current leakage in the cell, generally as a result of trap states, pinholes, and edge effects. It is desirable to maximize R_{SH} such that there is no current flowing through this resistor in the equivalent circuit model, and in an ideal case, R_{SH} will be infinite.

1.2.3 External Quantum Efficiency (EQE)

The external quantum efficiency (EQE) is a measure of how much current will be produced by a particular wavelength of light and is given by the ratio of collected photogenerated charges and the number of incident photons. It is the probability that the absorption of one photon will result in the generation of one electron that is able to flow through an external circuit, and is typically integrated over the solar spectrum. The EQE describes the overall efficiency of the four main processes in the photovoltaic process for OPV, including absorption, exciton diffusion, charge separation, and charge collection, as defined by equation 6.

$$EQE(\lambda) = \eta_{abs}(\lambda) \times \eta_{diff}(\lambda) \times \eta_{CT}(\lambda) \times \eta_{coll}(\lambda) \qquad (6)$$

where η_{abs} is the photoabsorption efficiency, η_{diff} is the exciton diffusion efficiency to the donor/acceptor interface, η_{CT} is the charge transfer efficiency, η_{coll} is the charge collection efficiency, and λ is the wavelength of interest. EQE values closest to 1 for a specified wavelength indicate efficient current generation for light absorbed at that wavelength, with limited recombination losses. Increasing recombination or reflection losses result in lower EQE values.

1.2.4 Solar spectra

Historically, test conditions for solar cells were not standardized, and there exist a variety of results in the early literature with seemingly inflated values due to discrepancies in testing conditions. Photovoltaics are now generally tested under standard conditions developed by the American Society for Testing and Materials (ASTM) in conjunction with research and development laboratories in order to influence

reporting of comparable results. Briefly, laboratory testing is performed under the AM 1.5 G Solar spectrum, as outlined in Figure 5,[10] at an incident power of 1000 W/m^2. The AM 1.5 G spectrum was developed for flat plate modules and represents the annual average solar irradiance at mid-latitudes, and takes into account 1.5 times the thickness of Earth's atmosphere normal to the surface. In contrast, the AM 1.5 D spectrum was developed for use with solar concentrators, with an incident power of 900 W/m^2 and includes not only the direct beam from the sun, but also a circumsolar component that accounts for a disk 2.5 degrees around the sun. Both of these standardized spectra have significantly reduced spectral irradiance relative to the top of the atmosphere, where the AM 0 solar spectrum, with an incident power of 1366 W/m^2, will be of interest.

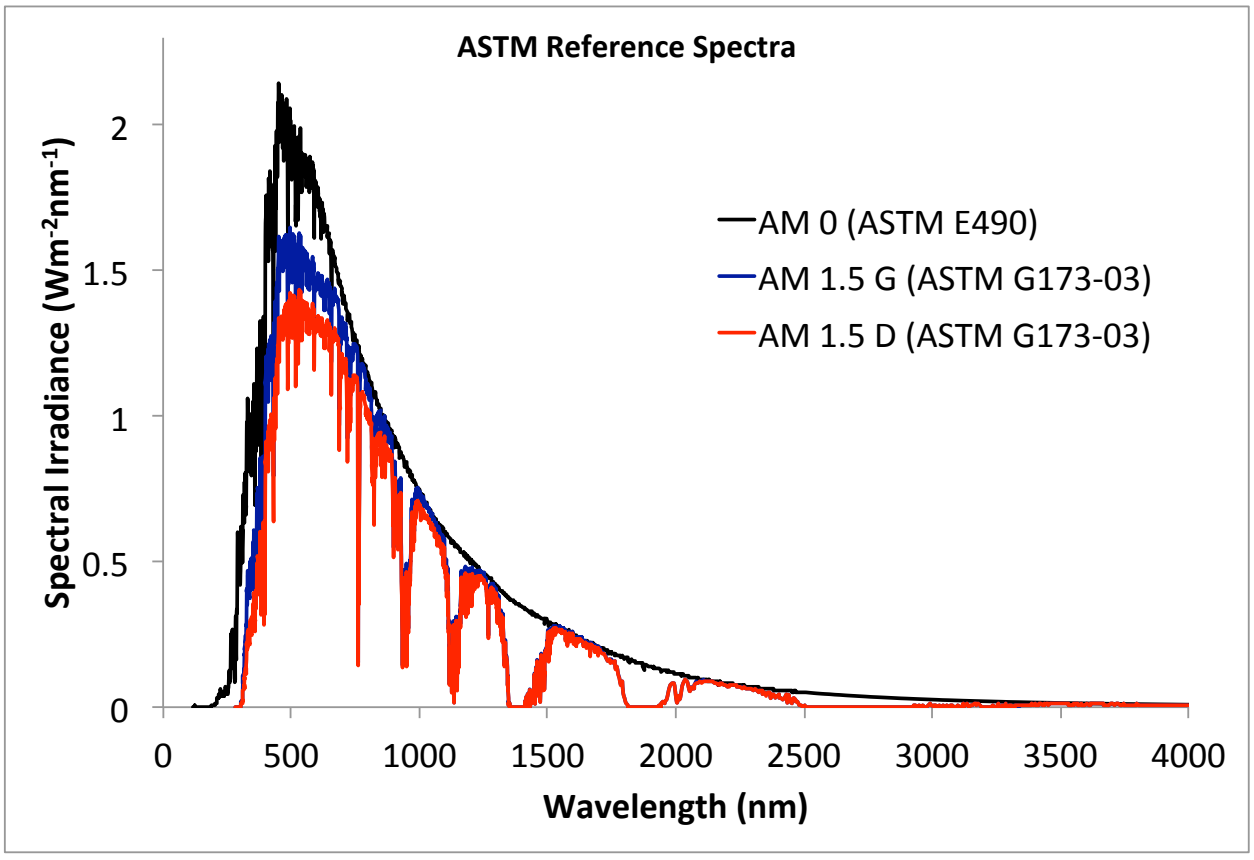

Figure 3: AM 0 (black), AM 1.5 G (blue), and AM 1.5 D (red) solar spectra.[10]

1.3 Characterization of charge transport properties

1.3.1 Organic Field Effect Transistors (OFETs)

Organic field effect transistors are a common device structure used to characterize the charge transport properties of organic polymers and small molecules. OFET devices consist of 4 layers, including the substrate/gate, dielectric, semiconductor, and electrodes. Figure 6 provides a schematic of the commonly used top contact bottom gate geometry OFET. In a typical device, the substrate will consist of a doped-Si/SiO_2 wafer that also serves as the gate electrode and insulating dielectric layer. The semiconductor layer will typically be spin coated or thermally evaporated, followed by sequential thermal evaporation of the electrode contacts. OFETs transfer charge in accumulation mode, which means that application of the gate bias results in the build up of charge carriers that can then be transported through the semiconductor with a potential offset between the source and drain electrodes. Voltages are typically applied to the gate (V_g) and drain (V_d) in reference to the grounded source electrode (V_S = 0V), and the current (I_d) that develops between the source and drain electrodes is

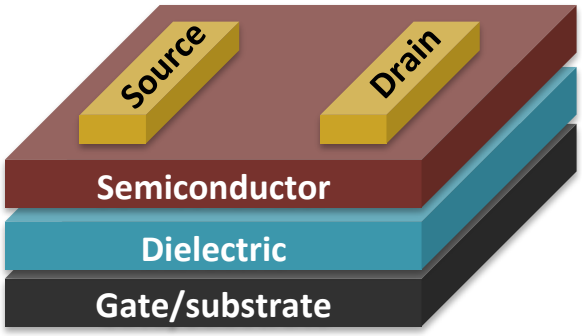

Figure 6: Schematic representation of an OFET device in the top contact bottom gate geometry

dependent on both V_g and V_d.

The key charge transport parameters that are obtainable through the analysis of OFETs include the charge carrier mobility (μ), the threshold voltage (V_T), and the on/off current ratio ($I_{ON/OFF}$). Figure 7 a and b[11] provide examples of typical I_d vs V_d family of curves for different V_g and an example of an I_d vs V_g curve, respectively. From the family of curves, we can find the linear and saturation regimes. The linear regime is the area of the output curve that has an approximately linearly increasing slope. This corresponds the region where V_d is much smaller than V_g. The current saturates when V_d is much greater than V_g.

The field effect mobility in the saturation regime can be calculated according to

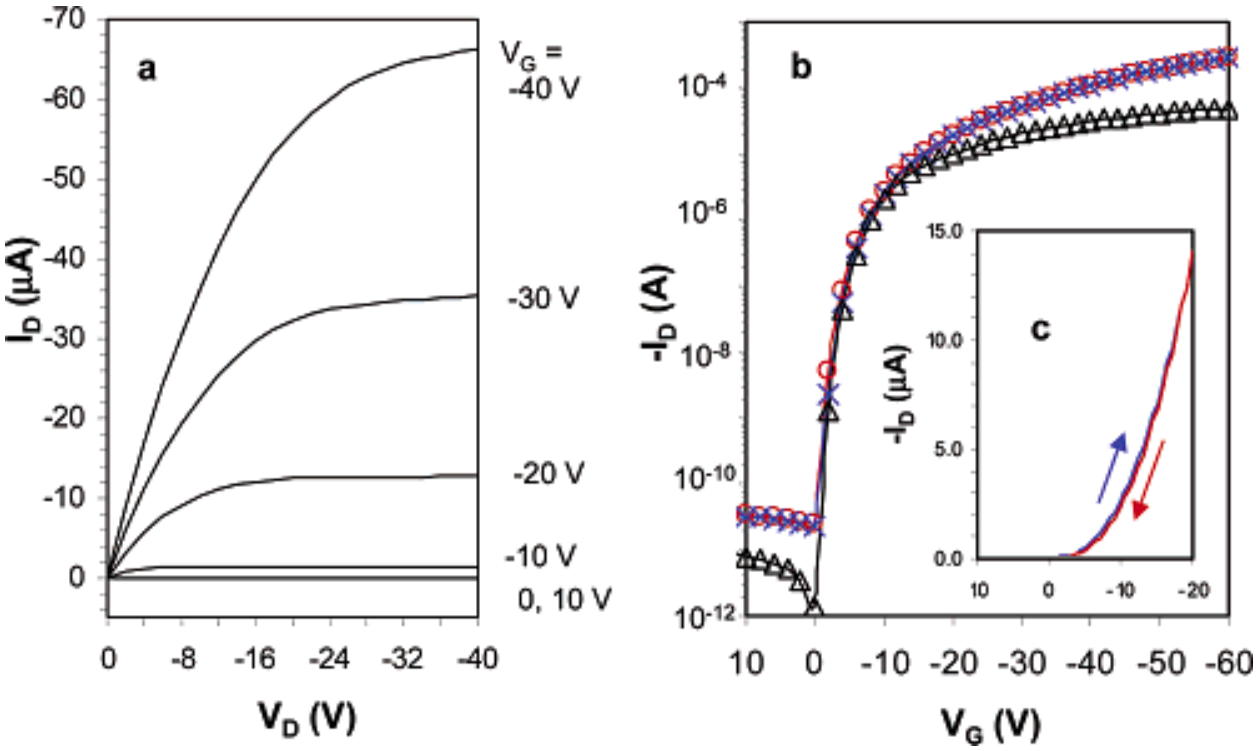

Figure 7: a) typical I_d vs V_d family of curves for different V_g and b) I_d vs V_g curve. Reprinted with permission from J. Am. Chem. Soc. Copyright 2004 American Chemical Society. [11]

Equation 7.

$$I_d = \frac{WC_i}{2L}\mu\left(V_g - V_T\right)^2 \quad (7)$$

where I_d is the drain current, W is the channel width between electrodes, C_i is the capacitance density of the dielectric layer, L is the channel length, μ is the mobility, V_g is the gate voltage, and V_T is the threshold voltage. V_T can be determined as the point where an extrapolation of the linear regime in the I_d vs V_g plot crosses the x-axis. The on/off ratio can be determined as the ratio between the maximum I_d when the transistor is on to the minimum Id when the transistor is off.

1.4 OPV device architectures

Because organic materials tend to require an energetic offset to dissociate excitons, attempts at using single layer architectures have been relatively unsuccessful, with these single layer device architectures affording with device efficiencies on the order of 0.1% or less.[12] The seminal work of Tang in 1979 introduced the concept of a two component donor/acceptor active layer for organic photovoltaics that relied on layers of thermally evaporated small molecules.[13,14] These bilayer structures were primarily limited by the exciton diffusion length, and only excitons generated near the donor/acceptor interface lived long enough to dissociate at this interface.[15] This work paved the way for the development of other donor/acceptor type architectures with increased donor/acceptor interfacial areas, including the solution processed bulk-heterojunction (BHJ) type architecture, as first reported with a fullerene acceptor by Yu *et al.* in 1995, and which is considered the state of the art active layer morphology to

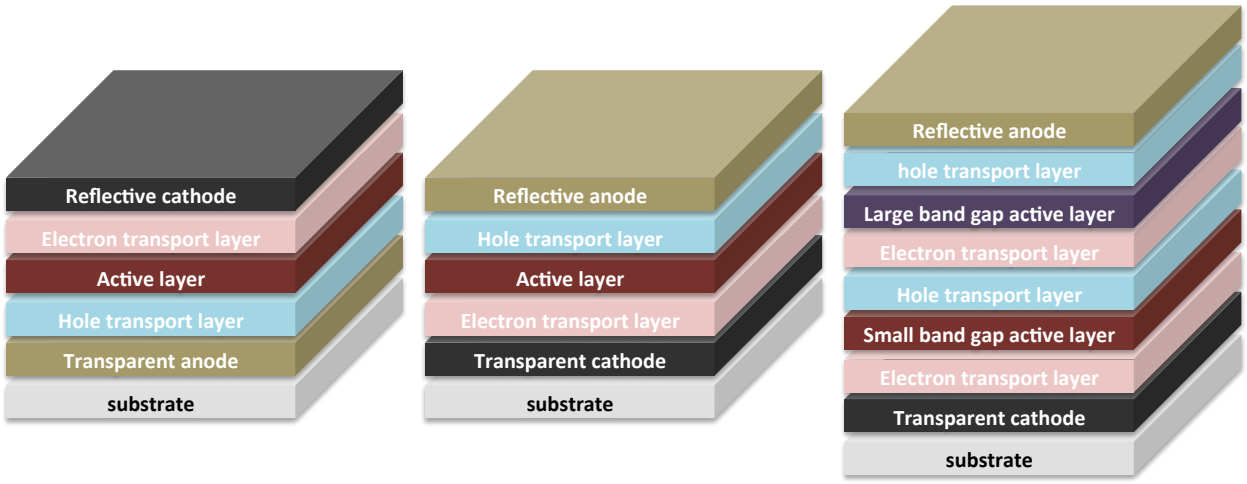

Figure 8: (left) Standard bulk heterojunction device architecture, (middle) inverted architecture, (right) tandem geometry.

this day.[16] The BHJ architecture relies on finding a balance between charge generation and transport and can be limited by charge carrier lifetimes. Figure 8 provides schematic illustrations of three common OPV device architectures, including standard BHJ, inverted BHJ, and tandem devices, each of which has its own benefits and areas that need improvement.

In a typical BHJ type solar cell,[17] the active layer is sandwiched between an anode and a cathode, as outlined in Figure 8. With standard architectures, holes are transported to the anode and electrons are transported to the cathode. The anode in this case typically consists of a substrate that is coated with a high work function transparent conducting electrode, and modified with an interfacial hole selective/electron blocking layer between the electrode and the active layer. The most commonly observed materials in the OPV field used for these electrodes are tin-doped indium oxide (ITO) on glass substrates modified with a ~40 nm thick poly(ethylenedioxythiophene):poly(styrene sulfonic acid) (PEDOT:PSS) interfacial layer.

These materials are favorable due to their large optical transparency and good charge transport properties. There exist several issues with this combination, however, including the brittleness of both glass and ITO not allowing for roll to roll processing, the rarity and price of indium, and the acidity of PEDOT:PSS tending to degrade devices. The cathode is typically comprised of a low work function metal with an electron selective interlayer between the active layer and the metal electrode. The most frequently encountered cathode in the literature is aluminum, and popular interlayers have evolved over time, where LiF has waned in popularity with the rise of the Ca interlayer. The aluminum cathode is attractive due to its low work function and high reflectivity, but the low work function gives it highly reductive properties and it may react with polymers, or any water or oxygen in the system, resulting in an additional degradation pathway.

The inverted BHJ architecture was developed to help alleviate device degradation through both the use of different electrodes and encapsulation. The inverted architecture results in the reversal of the roles of the charge collecting nature of the electrodes. This effectively eliminates the need for a low work function, air-sensitive electrode, while simultaneously removing PEDOT:PSS from the ITO surface, which has been shown to introduce both chemical and morphological degradation at the ITO interface due to its acidic nature.[18] The key to development of alternative architectures lies in the tunability of the ITO work function based on interlayer modifications. In the inverted structure, ITO is typically coated with a low work function material, such as ZnO or other transition metal oxides, in order to reduce its work function and make it applicable as the cathode. The anode typically consists of a stable metal, such as Ag or

Au that is functionalized with a high work function transition metal oxide interlayer, such as V_2O_5 or MoO_3, both of which exhibit better stability to oxidation. In addition to better stability, the inverted architecture is generally more compatible with high throughput processing and provides better flexibility for the development of tandem architectures.

Tandem architectures have been developed in order to address two specific issues associated with OPV. The first is in regard to the limits in active layer thickness that do not allow for a maximum amount of solar insolation to be absorbed, and which are imposed due to the relatively low charge carrier mobilities associated with the components of the active layer. The second relates to how the active layer materials absorb light, where any light not absorbed within the often narrow band gap of the organic absorber will be transmitted through the cell, and therefore lost. Tandem architectures consist of at least two independent active layers stacked on top of each other, one of which absorbs high-energy photons and transmits low energy photons through that can then be absorbed in another layer. Each independent active layer is separated from the other active layers by an interconnect layer that allows holes from one sub layer to recombine with electrons from another. Overall, the tandem structure is able to absorb more light because each layer can have complimentary absorption spectra, while maintaining relatively thin active layers, therefore not being limited by the thickness of the active layer. It is desirable for each independent active layer in a tandem solar cell to deliver similar currents in order to maximize the efficiency of these devices. It has been hypothesized that tandem architectures should be able to produce 30% better efficiencies than their single junction counterparts. Tandem organic solar cell efficiencies have reached a 12% benchmark, as produced by Heliatek, and these

devices are expected to exceed 15% efficiency in the near future.[19]

The development of alternative device architectures will continue to be important as the OPV field progresses towards commercialization. Each of the main architectures discussed has its own benefits, including the ease of processing and rich history of the standard BHJ architecture, the better stability and flexibility of the inverted architecture, and the better efficiency characteristics of the tandem architecture, but it is clear that more effort must be put forth in developing materials for each layer in these architectures in order to realize the commercialization of OPV. In the following section, we focus on the development of constituents for the active layer, leaving electrode and interlayer materials for the focus of other reviews. [20]

1.5 Materials

Significant achievements have been made in OPV device performance through materials design, as the device performance parameters are highly dependent on the optical and electronic properties of the constituents of the active layer. The primary concerns for the development of effective donor and acceptor materials include developing materials with appropriate band gaps and energy levels in order to maximize both the J_{SC} and V_{OC}, promoting good charge carrier mobilities through the planarization of polymers along with good π-π stacking characteristics, and developing stable materials, all while maintaining their solution processability. Figures 9 and 10 provide some examples of popular polymer and small molecule donor materials that have been used for OPV. In addition to producing polymers with good optoelectronic properties, other concerns for polymer design can include controlling the regioregularity, molecular weight, and dispersity of the polymers. The regioregularity of a polymer is defined as the

ratio of monomers adopting head-to-tail (HT) coupling relative to those adopting head-to-head (HH) coupling in the polymer chain, as outlined in Figure 9. It is an important property for polymers derived from asymmetrically substituted monomers, such as 3-hexylthiophene, but is not applicable for polymers synthesized with symmetric monomers. The molecular weight of a polymer is different than that of a small molecule, because polymer molecular weights comprise a molecular weight distribution due to how they are synthesized. The number average molecular weight, M_n, is defined as the total weight of all polymer molecules in a sample divided by the total number of polymer chains in that sample and is an important parameter for physical properties that are not dependent on the size distribution of the polymers, as described by equation 8.

$$M_N = \frac{\sum M_i N_i}{\sum N_i} \tag{8}$$

where M_i is the molecular weight of the *i*th polymer and N_i is the number of *i*th polymers. When size distribution is important, we need to consider the weight average molecular weight of the sample. This is a more abstract concept because it is the molecular weight per unit weight of polymer, as described by Equation 9.

$$M_W = \frac{\sum M_i^2 N_i}{\sum M_i N_i} \tag{9}$$

M_n is always lower than M_w. The dispersity, *Đ*, of a polymer is an indicator of the size heterogeneity of a sample, with a low *Đ* (closest to 1) representing a narrower molecular weight distribution within the sample than a higher *Đ* sample. It is defined as the ratio between the weight average molecular weight and the number average molecular weight, according to equation 10.

$$Đ = \frac{M_W}{M_N} \quad (10)$$

1.5.1 Polymers

Most of the materials used in the fledgling OPV community were designed for organic light emitting diode (OLED) applications, as this is where the majority of academic and industrial organic electronics research was focused at the time. As a result, popular OLED materials, such as poly(*p*-phenylene vinylene) based materials (PPVs) dominated the field in its early stages, and indeed, the first few points on the best research cell efficiency table in Figure 1 reflect this polymer backbone. In 1995, Yu *et al*. used poly[2-methoxy-5-(2'-ethyl-hexyloxyl)-1,4-phenylene vinylene] (MEH-PPV) in combination with C_{60} and some of its functionalized derivatives, including phenyl-C_{61}-butyric acid methyl ester (PCBM) in the first reported BHJ solar cells.[16] Later, in 2001, Shaheen *et al.* used another PPV derivative, poly[2-methoxy-5-(3′,7′-dimethyloctyloxy)-1,4-phenylenevinylene] (MDMO-PPV) and PCBM to show the importance of active layer morphology on device performance, as discussed in the following section.[21] During this time, significant improvements were achieved in the control of the synthetic reproducibility of these polymers, as well as in their regioregularity, molecular weight,

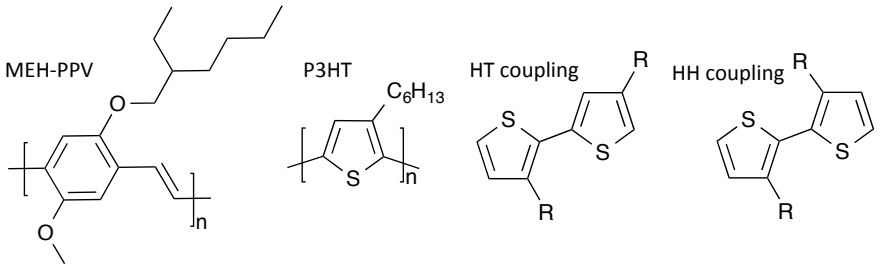

Figure 9: Popular polymer donor materials, highlighting different monomer coupling modes.

and *Đ*. However, it became clear that the relatively large band gap of PPV-based materials, along with their low charge carrier mobilities would impose significant limitations on the maximum achievable power conversion efficiencies of photovoltaics made with these donor materials. As a result, interests shifted towards new polymer donor materials, especially poly(alkyl-thiophenes), including the now benchmark material poly(3-hexylthiophene) (P3HT).

P3HT has proven to be a better material for OPV relative to PPVs due to its increased optical absorption, higher hole mobility, and its good solution processability. The performance of P3HT/PCBM solar cells depends critically on materials properties and processing conditions. The first encouraging results for P3HT/PCBM solar cells was published in 2002 by Schilinsky *et al.*, who were able to make devices with a maximum EQE of 76%.[22] This was followed by improving device performance in P3HT/PCBM solar cells via postproduction treatments by Padinger *et al.*, who showed that thermal annealing and simultaneous thermal annealing and application of an external electric field could be used to produce devices with maximum PCE of 3.5%, as a result of better morphology.[23] Kim *et al.* showed a strong dependence of the performance of P3HT/PCBM solar cells on the regioregularity of P3HT.[24] They found that increasing the regioregularity of the polymer resulted in better performance as a result of increased molecular order due to better π-π stacking, resulting in both enhanced optical absorption and better charge transport properties. Schilinsky *et al.* showed the importance of molecular weight, by showing that P3HT/PCBM devices performed better as the molecular weight of P3HT increased.[25] The increase in performance was primarily due to increased J_{SC}, and this was attributed to an increased mobility with

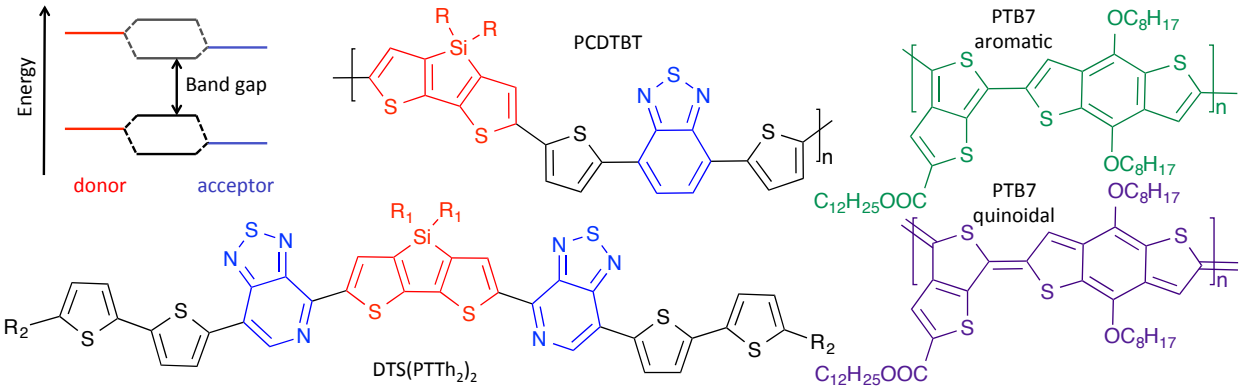

Figure 10: Examples of small band gap polymers and a small molecule, including different resonance structures.

polymer aggregation in the thin films with higher molecular weight P3HT. While P3HT remains the most studied polymer for OPV, it has been recognized that a smaller band gap polymer with a lower HOMO, and greater hole mobilities would be required to advance the field.

Two popular ways to decrease the band gap of semiconducting polymers have arisen in recent years, including the development of polymers with alternating electron-rich and electron-poor heterocycles along the polymer backbone, or so-called donor/acceptor (D/A) type polymers, as well as through the stabilization of the quinoidal form of conjugated backbones. In D/A polymers, the decrease in band gap arises from the orbital mixing of these internal donor and acceptor units, as schematically illustrated in Figure 10. One of the most successful examples of this type of D/A polymer is poly[*N*-9′-heptadecanyl-2,7-carbazole-*alt*-5,5-(4′,7′-di-2-thienyl-2′,1′,3′-benzothiadiazole)] (PCDTBT), which has 2,7-carbazole electron rich units and benzothiadiazole electron deficient units that are bridged by a conjugated thiophene unit, the combination of which results in an absorption spectrum that spans out to around 900 nm and devices made with this polymer have achieved efficiencies up to 7.5%.[26] There exist two ground state

resonance structures in highly conjugated polymers, including the aromatic and quinoidal forms, as shown schematically in Figure 10. The quinoidal resonance structure promotes better planarity of the polymer backbone, enhancing charge carrier mobility, and has a smaller band gap than the aromatic resonance structure, providing better overlap with the highest photon flux in the solar spectrum, but this resonance is less energetically stable. Thienothiophene is perhaps the most popular unit used to promote the quinoidal form of a polymer, with PTB7 perhaps being most widely studied polymer in this class. PTB7 was reported by Liang *et al.* as the first polymer used in OPV to have a PCE exceeding 7%, and with further optimization has achieved over 9% efficiency.[27,28] The high efficiency was primarily attributed to good J_{SC} and *FF*, owing to both high EQE and IQE, which show that this system has excellent exciton dissociation, charge transport, and charge extraction characteristics, making this class of quinoidal stabilized polymers a promising class of donor materials for OPV.

1.5.2 Small molecules

While polymers have come to show tremendous promise for applications in OPVs, they tend to suffer from batch to batch variations, including disparities in molecular weight, end group contamination, and *Đ*. Small molecules have recently emerged as promising alternatives to polymers for OPV applications. In addition to consistency in the synthesis of small molecules, they also tend to exhibit higher hole and electron mobilities than their polymeric counterparts due to their propensity to exhibit long-range order. Sun *et al.* recently reported small molecule BHJ solar cells with efficiencies of up to 6.7% using the small molecule donor 5,5'-*bis*{(4-(7-hexylthiophen-2-

yl)thiophen-2-yl)-[1,2,5]thiadiazolo[3,4-c]pyridine}-3,3'-di-2-ethylhexylsilylene-2,2'-bithiophene, or DTS($PTTh_2$)$_2$, as outlined in Figure 10.[29] This small molecule donor is solution processable, strongly absorbing in the 600-800 nm region, exhibits high hole mobilities, and high power conversion efficiencies, showing that small molecules can be active competitors for OPV applications. For further reading on both solution processed and thermally evaporated small molecule organic solar cells, the interested reader is referred to a recent review by Mishra and Bauerle.[30]

1.5.3 Fullerenes

Much of the progress in OPV research has been focused on the donor materials, but the development of novel acceptor materials with stronger absorption in the visible region and tunable energy level alignments can improve both the J_{SC} and V_{OC} of the cell. The most common acceptor materials are fullerene derivatives, as outlined in Figure 11. C_{60} is limited as an acceptor material due to its low solubility in common organic solvents, and as a result, the approach of adding solubilizing moieties to fullerenes has been adopted since the beginning of the field.[16] $PC_{61}BM$ has traditionally

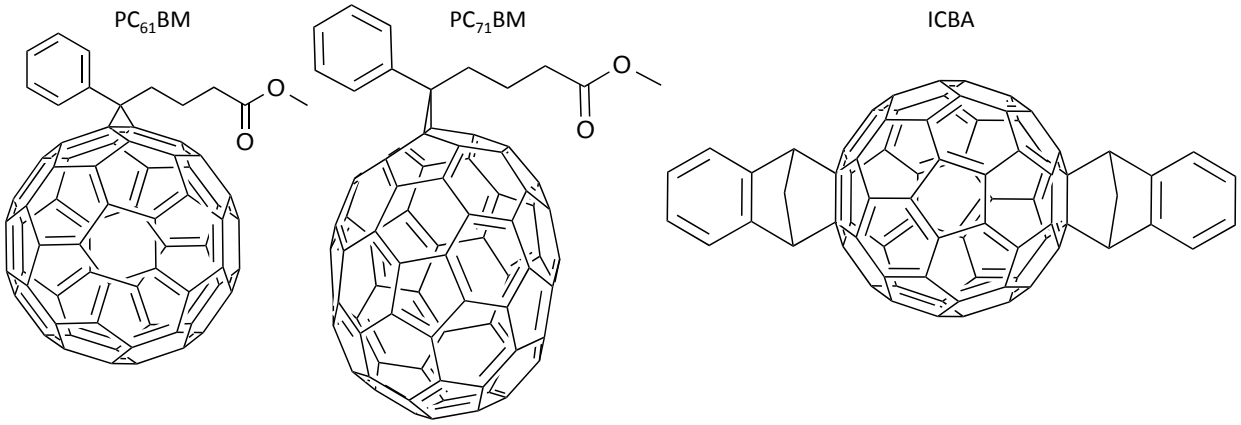

Figure 4: Common fullerene derivate acceptor materials.

been the most commonly used acceptor material, and has the advantages of good solubility in common organic solvents, high electron mobility, and a high electron affinity. However, $PC_{61}BM$ suffers from limited absorption in the visible region and a relatively deep LUMO, which limit its contribution to the J_{SC} of the device and constrains the energy level requirements for donor materials in order to obtain high V_{OC}. One approach to improve the acceptor characteristics is to replace $PC_{61}BM$ with its C_{70} derivative, $PC_{71}BM$. $PC_{71}BM$ is less symmetric than its C_{60} analogue, and therefore has more allowed optical transitions, thus extending its absorption spectrum into the visible, where it can often provide a complimentary absorption profile to the donor materials, and significantly increasing the overall J_{SC}.[31] $PC_{71}BM$ is the most common acceptor material used with low band gap donor polymers, and shows particular enhancement in performance when processed with small amounts of solvent additives that help promote idealized active layer morphologies, as discussed in the following section.[27] Another approach is to adjust the LUMO level of the fullerene, thus providing better energy level matching between donor and acceptor LUMO levels. The indene-C_{60} bis-adduct (ICBA), as first reported by He *et al.*, is the most widely used fullerene taking advantage of this approach.[32] It has a higher solubility in common organic solvents and is easier to synthesize than either $PC_{61}BM$ or $PC_{71}BM$, in addition to having a LUMO level that is 0.17 eV higher than $PC_{61}BM$. Initial P3HT/ICBA devices showed increases in V_{OC} from 0.58 V to 0.84 V and PCE from 3.9% to 5.4% relative to P3HT/$PC_{61}BM$ devices, and confirmed the potential of ICBA as a potential acceptor material for OPV. For further information on fullerene derivatives in OPV, the interested reader is referred to a recent review by He and Li.[33]

1.5.4 Inorganics

Another class of promising acceptor materials is inorganic nanocrystals. There are several different varieties commonly used, including Si, II-VI semiconducting nanostructures, such as CdS, CdSe, PbS, and PbSe, and transition metal oxides such as TiO_2 and ZnO. These materials offer many advantages over their fullerene counterparts, while maintaining the light weight and solution processability required for flexible, roll to roll processable OPV. Inorganics are more environmentally stable than their organic counterparts,[34] which can help alleviate some of the degradation mechanisms in OPV. They also have the potential to contribute to the photoabsorption and therefore charge generation of the solar cell at a greater rate than fullerenes.[35,36] They are capable of generating excitons, which stems directly from their ability to exhibit quantum confinement effects. Their quantum confinement can be controlled by changing the nanocrystal size, shape, and surface chemistry, allowing tailoring of the band gap, and therefore the absorption properties of these materials.[37–40] The ease of control of the absorption spectrum of these materials makes it possible to design donor and acceptor contributions with complimentary absorption profiles over the solar spectrum. Figure 12 provides a schematic of typical inorganic nanocrystal energy levels relative to some common donor materials.[41] In addition, inorganic nanoparticles have been shown to exhibit ultrafast charge transfer to organic semiconductors, often with transport rates faster than competing recombination processes.[42–44] Finally, kinetic control of nanoparticle synthetic has allowed the development of architectures, such as rods and tetrapods that can promote efficient exciton dissociation in conjunction with long charge transport pathways.[45–47] While all of these theoretical advantages sound

promising, they have yet to be fully realized, and current hybrid solar cells offer significantly lower power conversion efficiencies than their fullerene containing counterparts. The major factors limiting these devices are due to the nanoparticle surface chemistry, where nanoparticles are often coated in long chain aliphatic ligands that help stabilize them during colloidal synthesis, as well as a lack of ability to prevent nanoparticle aggregation due to their poor miscibility characteristics with polymers.

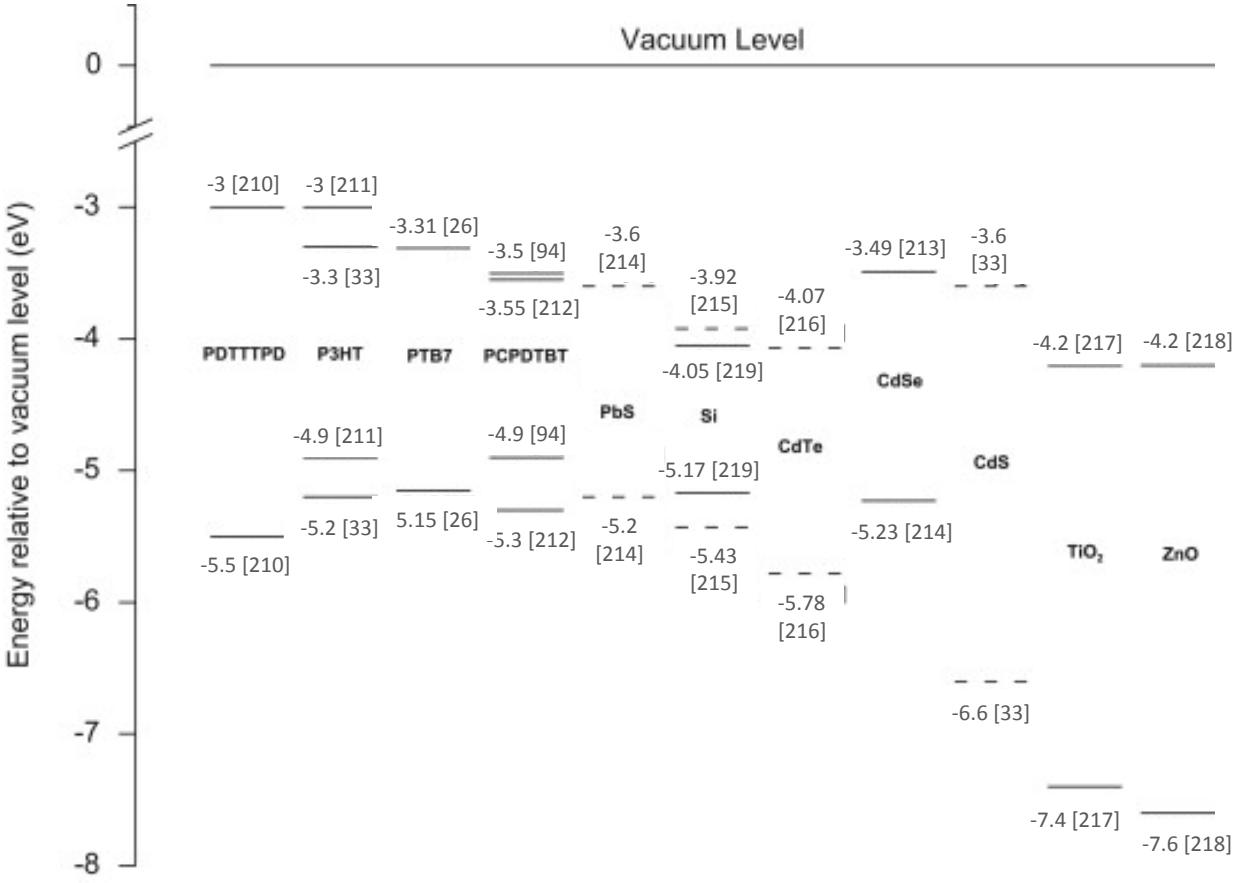

Figure 5: Energy band diagram displaying HOMO and LUMO of possible polymer donor materials, as well as the valence and conduction band edge of multiple inorganic acceptors. Values are taken from the references displayed in the figure. For the inorganic materials, solid lines represent bulk energy values, whilst dotted lines represent nanoparticles exhibiting quantum confinement. All energy levels are measured on isolated materials, using a variety of methods.[27,34,101,216–225] Figure reprinted from Solar Energy Materials and Solar Cells, Copyright 2012, with permission from Elsevier.[41]

1.6 Active Layer Morphology

Outside of materials development, one of the most fundamental issues in OPV processing is control of the active layer morphology. Indeed, extensive device optimization procedures have been followed since the beginnings of the field. A long-standing generalization is that the ideal active layer morphology will have an interpenetrating network of donor and acceptor materials, with domain sizes on the order of the exciton diffusion length, or around 10 nm.[48,49] Essentially, the active layer should have enough interfacial area to dissociate the greatest possible amount of excitons, while also maintaining continuous charge transport pathways to the electrodes. However, as with most idealized principles for OPV operation, the reality is much more complex, and substantial efforts are being directed at understanding how to manipulate the microstructure of the active layer in order to generate desirable photovoltaic properties using a variety of materials and in a predictive manner. Typical parameters that affect the active layer morphology include the solvent, donor/acceptor concentrations, thermal annealing times and temperatures, solvent annealing conditions, additives, and the interlayer surface energies. The active layer morphology affects every device characteristic, and has recently been the study of extensive reviews.[50–52] Here, we highlight some of long standing morphology optimization procedures, and discuss some recent developments in this area.

Because the ability to be solution processed is considered integral for the success of OPV, it is important to understand how solvent choice affects the resulting morphology. Solvent properties, including the vapor pressure, boiling point, viscosity, polarity, solubility, and wettability characteristics dictate much of the initial film forming

properties. The solute properties of the active layer components, including their concentrations, blend ratios, and solubility, are also important. Finally, the method of solution phase deposition is also important, as it is recognized that the requirements of high throughput processing will require alternatives to spin coating due to the large volume of materials and solvent and small areas required for this process. However, because it is the most widely used laboratory scale active layer deposition method, we will focus on the properties of spin coated active layers in this discussion. In 2001, Shaheen *et al.* reported on the nearly three fold improvement of MDMO-PPV/PCBM devices by processing the active layer from chlorobenzene rather than toluene.[21] They found that changing the solvent used for processing allowed for the formation of a more intimately mixed active layer with smaller domain sizes, which can be expected based on the better fullerene solubility in chlorobenzene. Hoppe *et al.* later performed a detailed study on the interplay between solvent, solvent loading, and blend composition.[1] They used varying weight ratios of MDMO-PPV:PCBM of 1:1, 1:2, 1:3, and 1:4 in toluene and 1:2, 1:4, and 1:6 in chlorobenzene. They found that increasing the ratio of PCBM with films cast from toluene resulted in films with increasingly large PCBM aggregates that were surrounded by a thin skin of MDMO-PPV by cross-sectional SEM, as shown in Figure 13. They also found that increasing the total polymer and fullerene content in the solution from 0.5% to 1.5% while maintaining the same weight ratio resulted in both increased film thickness and increased PCBM aggregation. When casting films from chlorobenzene, much better mixing of phases was observed for all weight ratios, and PCBM clustering was not observed until very high loading at 1:6 MDMO-PPV:PCBM, and even these clusters were much smaller than any of the

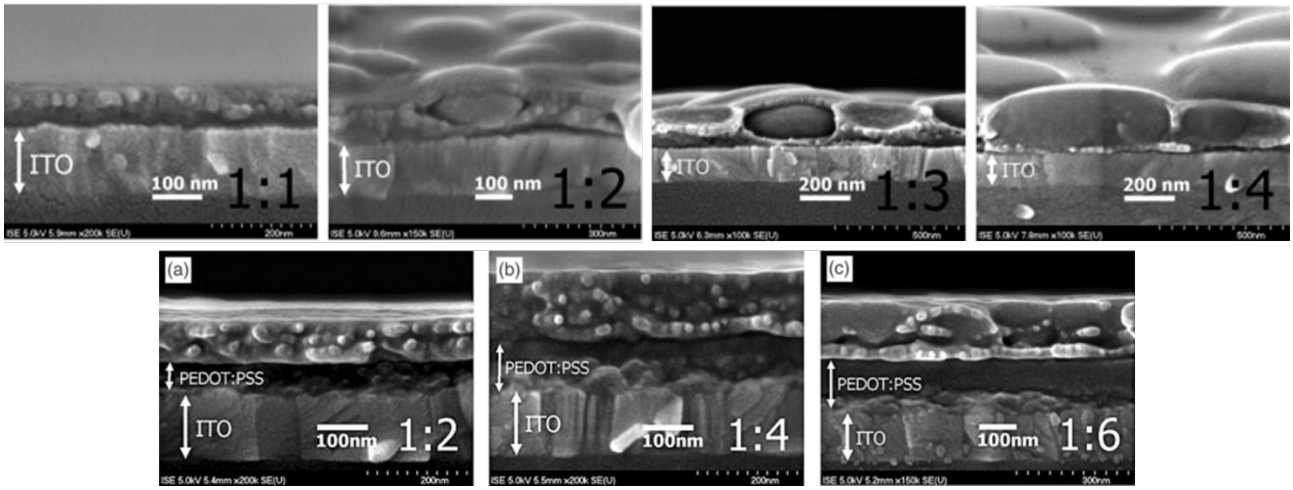

Figure 13: SEM cross sections of devices made with different MDMO-PPV:PCBM concentrations, as denoted in the bottom right of each image, and spun from (top) toluene and (bottom) chlorobenzene.[1] Copyright 2004, Wiley. Used with permission from ref 1, John Wiley and Sons.

clusters observed when processing from toluene. Li *et al.* showed that the solvent evaporation time will dictate the initial film properties, with slow evaporation allowing for phase separation of P3HT and PCBM, or fast evaporation resulting in the formation of an amorphous glass.[53]

Both thermal and solvent annealing have been shown to be effective methods for modification of the active layer morphology, thereby influencing the overall device performance. Both types of annealing have been shown to result in the formation of larger P3HT and PCBM domains, and improve P3HT crystallization in P3HT/PCBM devices, resulting in the extension of the optical absorption into the red and improving the charge transport characteristics due to greater polymer coherence lengths. Thermal annealing relies on heating substrates to temperatures greater than the glass transition temperature of the materials, thereby allowing them to reorient themselves to lower energy conformations. Two methods for thermal annealing have been investigated, including preannealing, where devices are annealed prior to cathode deposition, and

postannealing, where devices are annealed after cathode deposition. Ma *et al.* performed a systematic study of postannealing temperatures and times and showed that the postannealing of P3HT/PCBM solar cells significantly improves both the J_{SC} and *FF*, and they observed a decrease in the series resistance of the cell of more than an order of magnitude (from R_S = 113 Ω cm^2 to R_S = 7.9 Ω cm^2 with post annealing).[54] Mihailetchi *et al.* showed that postannealing enhances the hole mobility of P3HT in P3HT/PCBM solar cells by three orders of magnitude, and that this boost in mobility is the most important factor for the observed increase in performance.[55] They found that the generation of photocurrent in unannealed films is limited by the build-up of space charge, which is primarily a result of unbalanced charge carrier mobilities between P3HT and PCBM. After annealing above 110 °C, there was a 20-fold reduction in the difference between electron and hole mobilities, thereby reducing the space charge limitations due to the more balanced mobilities. Chen *et al.* used a variety of techniques, including GIXD, NEXAFS, and DSIMS, to determine how pre and postannealing affect the active layer morphology.[56] They found that both annealing strategies resulted in the formation of a bicontinuous network of polymer and fullerene with domains on the order of the exciton diffusion length, and observed increased power conversion efficiencies for both cases (PCEs of 0.61%, 1.10%, and 3.37% for as spun, preannealed, and postannealed, respectively). However, the preannealed samples showed an increase in P3HT concentration near the surface of the active layer due to its lower surface energy, and a preferential packing of P3HT in an “edge on” fashion, both of which limited the improvement in device efficiency. In contrast, the postannealed samples showed an increase in PCBM concentration near the cathode and a reorientation of P3HT to the

"face on" orientation, both of which promote efficient charge transfer, and are responsible for the greater improvement in device efficiency with postannealing rather than preannealing. The GIXD spectra highlighting the different propensities for edge on and face on polymer organization with the different annealing methods are shown in Figure 14. The difference in postannealing response is a result of the importance of the difference in interfacial energies between the anode and the cathode.[57]

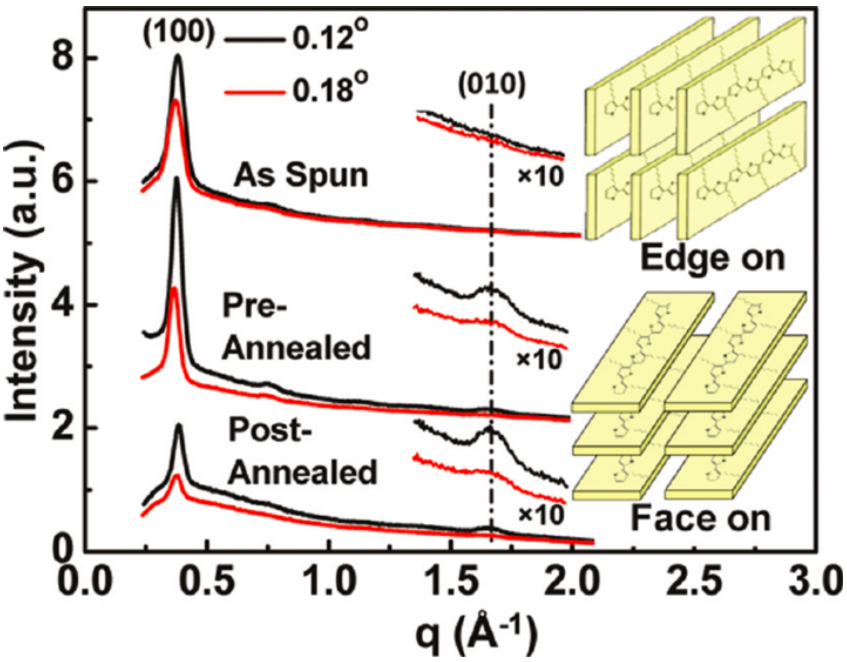

Figure 6: GIXD curves of P3HT/PCBM blend films at different incident angles. As spun; preannealed 30 min; postannealed 30 min. The insets represent the schemes of edge-on and face-on of P3HT chains.[56] Reprinted with permission from reference 56. Copyright 2011 American Chemical Society.

Solvent annealing is an annealing approach that introduces solvent (through soaking) or solvent vapor into the active layer, making both components better able to diffuse through the active layer. This greater mobility promotes both better crystallization of P3HT and diffusion and segregation of PCBM. Choice of solvent is important when solvent annealing, and Cho *et al.* showed that poor solvents (acetone and methylene

chloride) more greatly enhance device performance than good solvents (chloroform, 1,2-dichlorobenzene, chlorobenzene).[58] While good solvents were shown to develop greater self-organization of P3HT, thus extending the optical absorption and promoting more balanced mobilities, the short circuit current density was found to be limited in this case by recombination losses due to the development of too large domains that were greater than the exciton diffusion length. Jo *et al.* used TOF-SIMS to show that solvent annealing promoted segregation of PCBM to the top of their devices, thus promoting better charge transport properties, similarly to those observed for thermal annealing.[59] Chu *et al.* showed that solvent annealing more greatly enhances the EQE due to increased optical absorption relative to thermal annealing.[60] Overall, both thermal and solvent annealing are important approaches for improving the crystallinity and vertical phase segregation within the active layer, increasing the hole mobility, and promoting more balanced charge transport characteristics, which makes annealing one of the most common approaches for enhancing device performance.

More recently, the development of novel low band gap polymers, such as poly[2,6-(4,4-bis-(2-ethylhexyl)-4*H*-cyclopenta[2,1-b;3,4-b']-dithiophene)-*alt*-4,7-(2,1,3-benzothiadiazole)] (PCPDTBT), that do not respond well to annealing post-treatments have been reported. It has been found that using processing additives, such as alkanedithiols, can drastically improve the nanomorhpology with these low band gap polymers.[61] Lee *et al.* examined a series of 1,8-di(R)octanes with various functional (R) groups, and found that their best results were achieved with 1,8-di-iodooctane.[2] This material preferentially dissolves PCBM, tends to remain in solution longer during drying, and therefore promotes the increased development in the PCBM domain, as

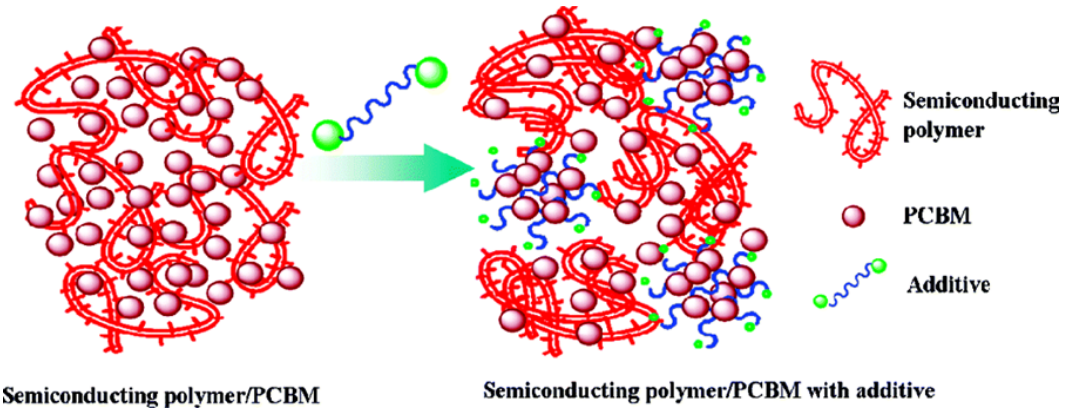

Figure 7: Schematic depiction of the role of the processing additive in the self-assembly of bulk heterojunction blend materials[2]

schematically depicted in Figure 15.[2] They developed two general guidelines that have been identified for additive design: (1) the additive must have a significantly higher boiling point than the primary solvent in order to extend the interaction time of the additive and the components of the active layer during thin film formation, and (2) one of the active layer components should have a much higher solubility in the additive than the other material. The use of solvent additives has become one of the most important methods for controlling the development of crystalline domains with low band gap polymer solar cells.

An interpenetrating network of pure domains approximately 10 nm in diameter has been considered the ideal morphology for the active layer because it strikes a balance between promoting exciton dissociation at donor/acceptor interfaces and transporting charges through the bulk. Recently, however, it has been shown that considering a three phase system that includes crystalline regions of donor and acceptor materials as well as a mixed amorphous region is more realistic. Materials in the mixed region will characteristically have larger band gaps than those in the crystalline regions due to their amorphous nature, as outlined in Figure 16.[62] This mixed

region necessitates changing our understanding of the energetic landscape of the bulk heterojunction architecture. With this three phase architecture, there is a clear driving force for exciton dissociation as well as imposed limitations for geminate recombination due to the energetic cascade caused by the mixed amorphous region. This supports the idea that the primary loss mechanism in BHJ solar cells arises from charge recombination, rather than geminate recombination or exciton decay. This mixed region was first indicated by Watts *et al*. in 2009 when they described the partial miscibility of PCBM in P3HT.[63] It has since become ubiquitous in the field when discussing the active layer microstructure.

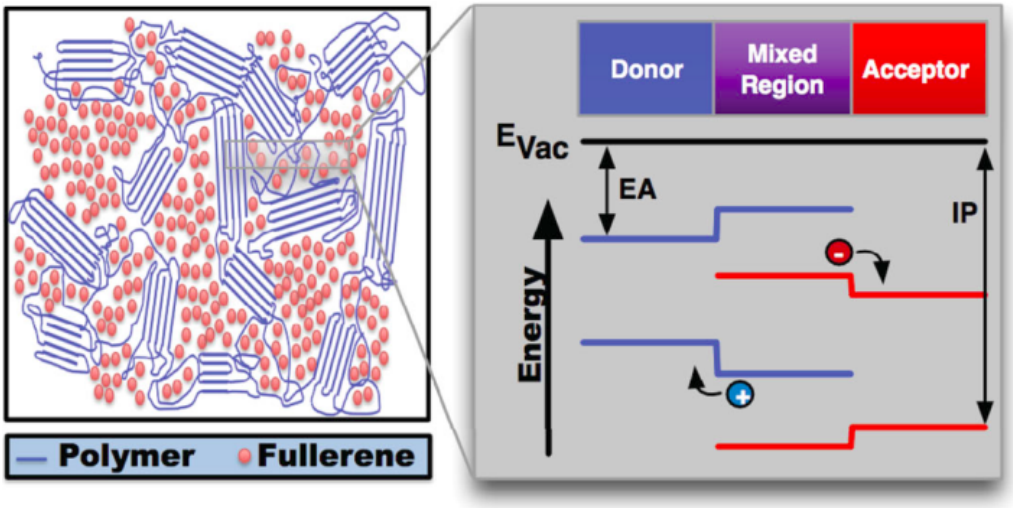

Figure 8: Schematic of a BHJ solar cell including the mixed region. Potential shifts in the local energetic landscape at the border between the donor, mixed and acceptor phases are shown in detail. EA is the electron affinity, IP is the ionization potential.[62] Copyright 2013, Wiley. Used with permission from ref 62, John Wiley and Sons.

1.7 Introduction conclusion and outlook

Much progress has been made in materials development and understanding the structure/property relationships of OPV materials and devices, but there are still many improvements that need to occur prior to the wide scale manufacture of OPV. Following

with the LCOE model, it is clear that improvements need to be made in increasing device efficiency, improving device lifetime, and lowering the cost of devices. While laboratory scale devices have recently been made with efficiencies over 9% in the single junction architecture and over 12% with a multijunction approach, there remains a significant drop in efficiency on the module scale.[19,28] Consequently, there is a strong need to improve module efficiencies, including identifying ways to translate lab scale performance to roll to roll processing and designing large-area modules that are able to reduce electrical losses. The stability of these devices will also need to be improved in parallel. This will require a greater understanding of the interactions at all of the interfaces of a given cell architecture, as well as improvements at both the material and device architecture levels of water and oxygen stability. Finally, the identification of materials that meet the above goals will necessitate large-scale production of these materials with limited batch-to-batch variation in addition to the utilization of these materials in high throughput processes.

Currently, OPVs are applicable only in niche markets that require lightweight, flexibility, and variable angle performance, such as in the consumer electronics market. However, the continued development of inverted and tandem device architectures, as well as improvement in the light harvesting ability and morphology control of active layer materials will result in widely applicable OPV technologies for electricity generation. Key economic indicators suggest that OPVs will become competitive with traditional energy sources as a result of a low LCOE and outstanding EPBT due to their lightweight and high-throughput, roll-to-roll solution processing, and the rapid progress of this field instills continued confidence in this technology.

Chapter 2: Oligoselenophene Derivatives Functionalized with a Diketopyrrolopyrrole Core for Molecular Bulk-Heterojunction Solar Cells

2.1 Introduction

Conjugated polymer-based bulk heterojunction (BHJ) solar cells have received considerable attention as promising renewable energy resources.[16,64,65] Significant efforts are being put forth to improve the power conversion efficiencies (PCEs) in order to meet the demands for high performance photovoltaic applications.[61,66,67] PCEs as high as 9.2%[28] have been achieved using a low band gap polymer as the donor and a soluble fullerene derivative, (6,6)-phenyl C_{71}-butyric acid methyl ester ($PC_{71}BM$), as the acceptor; however, this efficiency is still lower than that required for commercial applications.[68] The motivation for attaining reproducible and high PCEs drives various research efforts in the area of BHJ solar cells.[69–75] Recently, much attention has been focused on solution processable small molecule semiconductors as alternatives to conjugated polymers in BHJ solar cells due to several intrinsic advantages.[76,77] In general, small molecule organic semiconductors exhibit higher hole and electron mobility than their polymeric counterparts because they are more likely to exhibit long-range order. In addition, small molecule semiconductors do not suffer from batch to batch variations, broad molecular weight distributions, or end group contamination during synthesis.[78]

These benefits have resulted in a number of research groups investigating the application of small molecule based organic solar cells. To date, small molecule-based

BHJ solar cell devices exhibit PCEs exceeding 8% using $PC_{71}BM$ as an acceptor.[79] The majority of small molecule donor materials have been focused on thiophene-based oligomers because of their high charge carrier mobility; however, thiophene-based oligomers often do not absorb strongly in the longer wavelengths of the solar spectrum and tend to exhibit low solubility in common organic solvents. This may result in lower efficiencies relative to either polymer-based solar cells or thermally deposited small molecule bilayer solar cells.

The incorporation of selenophenes may help compensate for some of the disadvantages of thiophene containing compounds. In general, selenophene containing compounds have the advantages of lower oxidation and reduction potentials, strong light absorptivity, ease of polarizability, and improved interchain charge transfer, while maintaining structural similarities to thiophenes.[80] Selenophene-based oligomers and polymers have attracted some interest as organic thin film transistor (OTFT) materials,[81,82] as several selenophene-containing compounds have been shown to exhibit excellent hole mobility. Despite these advantages, selenophene-based compounds have attracted little attention in the area of organic photovoltaics.[83,84] To the best of our knowledge, no oligoselenophene-based photovoltaic materials had been reported when this research was first publicly disseminated.[85]

Additionally, diketopyrrolopyrrole (DPP)-based materials have attracted tremendous attention recently because of their promising performance in solar cells as well as in field-effect transistors.[86–91] The DPP core contains a planar bicyclic structure that promotes strong π−π stacking providing high hole mobility materials.[92] It also contains electron-withdrawing carbonyl groups that make the DPP core suitable for use

as the acceptor unit in low band gap donor−acceptor materials. These two properties make DPP-based materials attractive for use in photovoltaic devices.

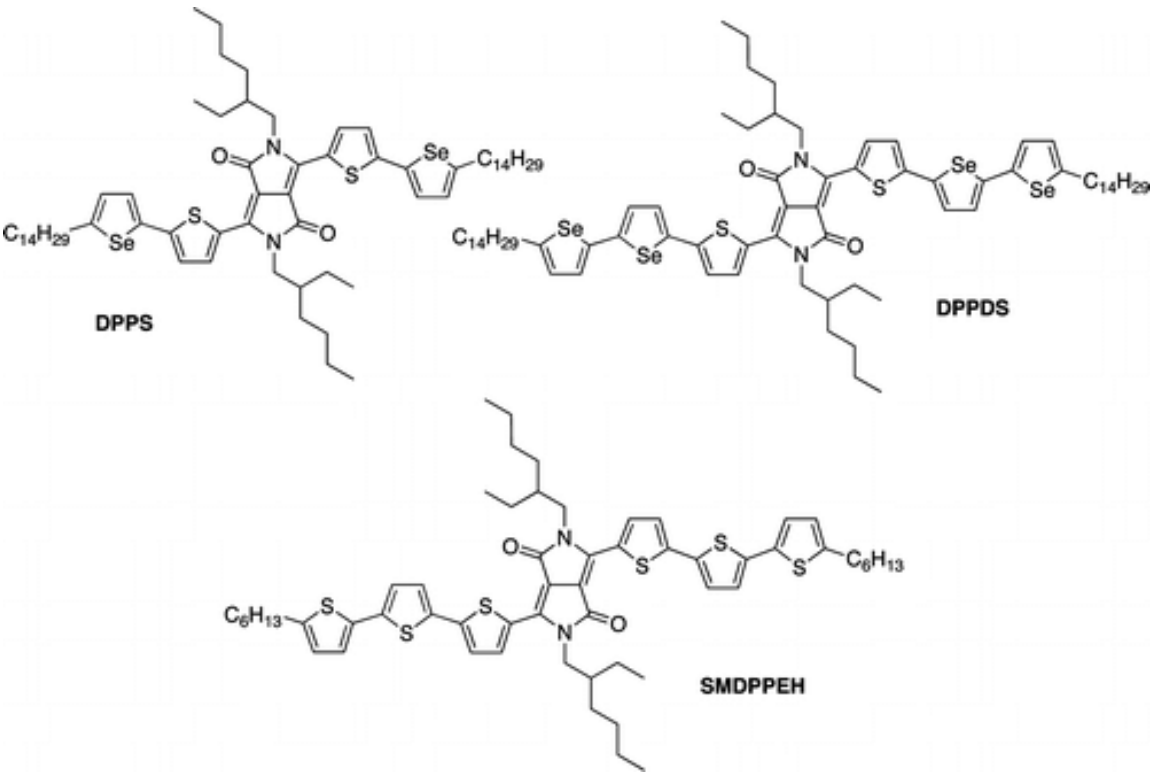

Figure 9: Structures of the synthesized oligoselenophenes, DPPS and DPPDS, and the previously synthesized SMDPPEH.

The goal of this work was to utilize selenophene derivatives in small molecule BHJ solar cells that were modeled after a previously reported thiophene-based material containing a DPP core (SMDPPEH) that achieved a PCE of 3.0% using $PC_{71}BM$ as the acceptor.[93] In this chapter, we examine the use of the oligoselenophene derivatives DPPS and DPPDS as shown in Figure 17, containing a DPP core for solution processable small molecule-based BHJ solar cells. It was necessary to increase the solubilizing chain from a C6 alkyl chain to a C14 alkyl chain because of the limited solubility observed in the selenophene derivatives. The aim in designing these systems

was to take advantage of the hole transporting and electron donating characteristics of these oligoselenophenes. It was intended that the internal electron transfer between the selenophene and the DPP core would induce a stronger light absorption in longer wavelengths relative to the previously reported thiophene derivatives, and that the higher molecular ordering of oligoselenophenes and DPP-based materials in the solid state would potentially enhance the charge carrier mobilities in these systems. To the best of our knowledge, this work represents the first reported example of oligoselenophenes to be used in molecular bulk heterojunction devices, and this work can be used as a basis for improving upon future oligoselenophene-based systems.

2.2 Experimental

2.2.1 Device Fabrication

ITO coated glass substrates (15 Ωm^{-2}) were cleaned with Meri Suds detergent, DI water, acetone, and IPA in an ultrasonic bath for 10 min each. They were then dried under N_2 and air plasma cleaned for 15 min. A 40 nm layer of poly(3,4-ethylenedioxythiophene) poly(styrenesulfonate) (PEDOT:PSS; clevios PVP Al 4083) was spin coated as the hole selective layer and annealed at 120 °C for 10 min. Active layers consisting of DPPS or DPPDS and phenyl-C_{61}-butyric acid methyl ester (American Dye Source, Inc. ADS61BFB) with various weight ratios (1:3, 1:2.5, 1:2, 1:1.5, 1:1, 1:0.8, 1:0.6) in chloroform (20 mg mL^{-1}) were spin coated on top of the PEDOT:PSS at 1500 rpm for 60 s. All active layer solutions were allowed to stir in a glovebox for at least 4 hours at room temperature before being filtered with a 0.2 μm PTFE filter. Top contacts for photovoltaic and EQE measurements consisted 0.9 nm LiF

and 100 nm Al layers that were thermally deposited at a base pressure of 2×10^{-6} Torr. Photovoltaic devices were annealed for 2, 5, 10, and 15 min. at 40, 50, 60, 80, and 100 °C in order to determine the optimal device performance conditions.

For OTFT measurements, devices were fabricated with a top contact geometry on heavily doped p-type Si/SiO_2 wafers (300 nm thermal oxide, Montco Silicon Technologies, Inc.). Substrates were cleaned by sonicating in acetone, methanol, and IPA for 15 min each. The wafers were then dried under nitrogen and air plasma etched for 10 min. Solutions of DPPS and DPPDS were made with chloroform ($CHCl_3$), *ortho*-dichlorobenzene (*o*DCB), and chlorobenzene (CB) at concentrations of 5 mg/mL. $CHCl_3$ solutions were spin coated at 800 rpm, while *o*DCB and CB solutions were spin coated at 1200 rpm, all for 60 s. Au source and drain electrodes (W = 9000 μm, L = 900 μm) were thermally evaporated through a shadow mask to 50 nm thick at a base pressure of 7×10^{-7} Torr.

2.2.2 Device Characterization

Photovoltaic device performance was characterized in air under simulated 100 mW cm^{-2} AM1.5G irradiation using an Oriel Xe arc lamp coupled with a Keithley 2400 source measurement unit. The solar simulator light intensity was calibrated with an NREL certified Si photodiode with a KG5 optical filter. The EQE was measured using the same source for photovoltaic measurements along with and Oriel Cornerstone 130 1/8m monochromator and referenced to an unfiltered, NREL certified Si photodiode. OTFT measurements were conducted in the dark in inert atmosphere. The absorption spectra were measured on a Perkin-Elmer Lambda-9 spectrophotometer. Atomic force microscope (AFM) images were taken in tapping mode on a Veeco multi-mode AFM

using a nanoscope III controller. All AFM images were taken from actual devices used to measure the photovoltaic properties.

2.3 Results and Discussion

2.3.1 Optical Properties

The thin film and solution absorption spectra were obtained for each compound, the results of which are summarized in Table 1. Figure 18 shows the solution absorption spectra of both compounds in chloroform, where it can be seen that they both exhibit similar features. Two main absorption peaks appear in both the ultraviolet and visible parts of the spectrum from 300-450 nm and from 550-750 nm, respectively. The latter absorption band is attributed to the charge transfer band from the selenophene units to the DPP core. It should be noted that both compounds exhibit a broad band in the long wavelength regions. This is due to the intermolecular aggregation state caused by the strong polarity of the amide groups in the DPP units[94,95] as well as to the increased vibronic coupling associated with the molecular rigidity imposed by molecular connectivity in solution measurements.[94]

Table 1: Optical data for DPPS and DPPDS.

	UV-Vis absorption data			
	Solution	Film		
	λ_{max}(nm)	λ_{max}(nm)	λ_{onset}(nm)	E_g[a](eV)
DPPS	628	695	720	1.73
DPPDS	628	655, 722	815	1.52

Absorption maxima (λ_{max}) were observed at 628 nm in solution for both DPPS and DPPDS and the molar absorption coefficients in solution (ε_s) were calculated to be 61300 M^{-1} cm^{-1} for DPPS and 76100 M^{-1} cm^{-1} for DPPDS. Thin film absorption maxima were found at 695 nm for DPPS and 655 nm for DPPDS with calculated thin film molar absorption coefficients (ε_{tf}) of 32000 M^{-1} cm^{-1} and 35400 M^{-1} cm^{-1} for DPPS and DPPDS, respectively. With DPPDS, the additional selenophene rings results in a red-shift of the absorption spectrum in both thin film and solution due to its increased π-conjugation length, relative to DPPS, as can be seen in Figure 18 a and b. Specifically, the absorption maximum (λ_{max}) of the charge-transfer band is extended into the red by 27 nm for DPPDS in solution. The thin film absorption of DPPS and DPPDS on glass substrates exhibit an even larger red-shift compared to the solution spectra, suggesting an effective interchain π-π stacking phenomena. The absorption bands edges extend up to 745 nm and 830 nm for DPPS and DPPDS, respectively. Based on the onset of absorption, the optical band gap was calculated to be 1.73 eV and 1.52 eV respectively for DPPS and DPPDS.

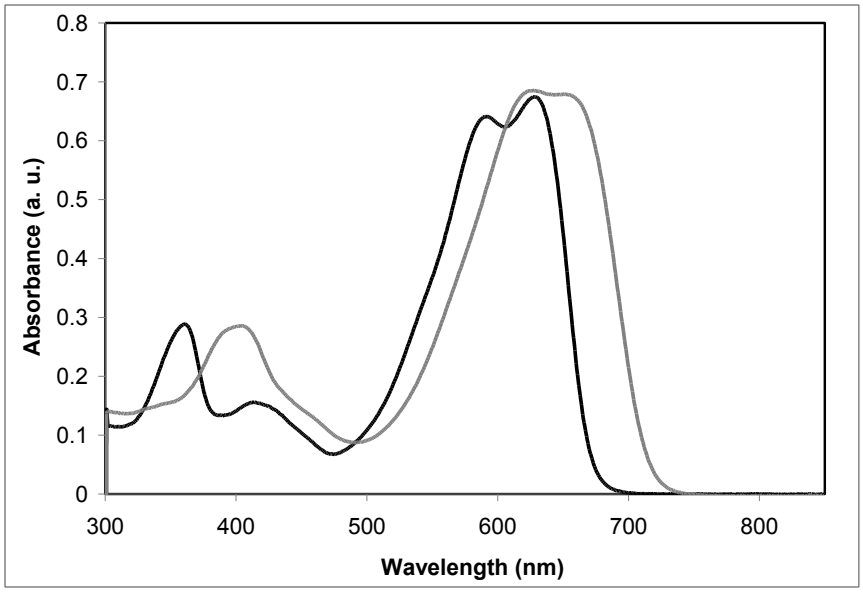

a)

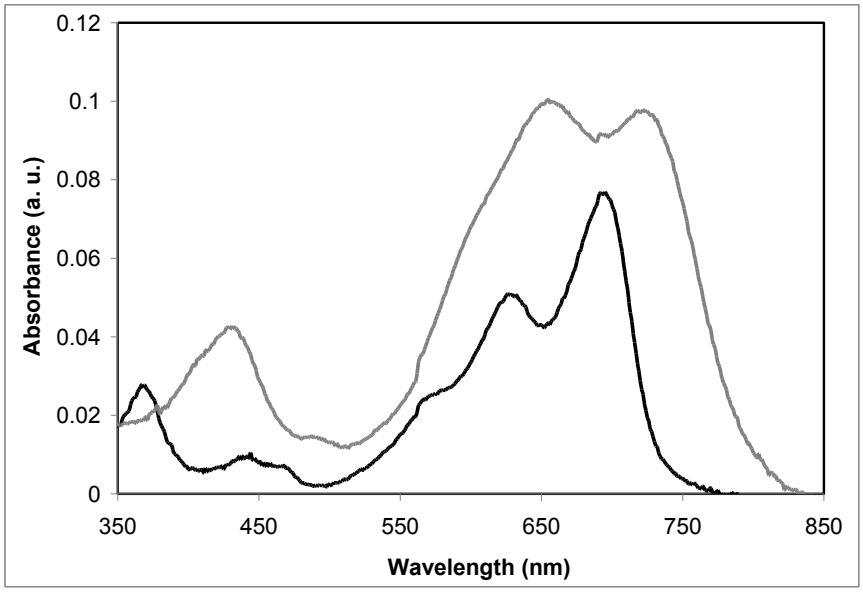

b)

Figure 10: UV-Vis absorption spectra of DPPS (black line) and DPPDS (grey line) in (a) $CHCl_3$ (0.0125 mg mL^{-1}) and (b) thin film on glass substrates.

2.3.2 Photovoltaic Properties and Thin Film Morphology of DPPS and DPPDS

In order to demonstrate the potential of DPPS and DPPDS as electron donating chromophores, BHJ solar cells were fabricated. Figure 19 shows current density versus voltage (J-V) curves for DPPS and DPPDS devices fabricated under optimized conditions and characterized under simulated AM 1.5G solar radiation at an incident

power intensity of 100 mW/cm^2. Table 1.2 provides a summary of the photovoltaic properties for an average of 16 devices for DPPS and DPPDS fabricated under the optimized conditions. Each active layer blend was subjected to a series of device optimizations as described in the Experimental Section. Conditions examined included solvents, donor:acceptor weight ratios, and annealing times and temperatures. For both DPPS and DPPDS, the optimal device conditions were found to be 1:1 weight ratios of DPPS:$PC_{61}BM$ and DPPDS:$PC_{61}BM$ in chloroform, respectively, without annealing for DPPS and with annealing at 80 °C for 5 min for DPPDS. Devices made in $CHCl_3$ showed over 50% improvement in device performance compared to those devices made in *o*DCB. In the PCBM concentration studies, the observed increase in PCEs with 1:1 weight ratios can be attributed to increased J_{SC} at this ratio, with decreasing J_{SC} at higher and lower weight ratios. With DPPS, annealing lowered the overall J_{SC} and resulting PCE, even at low temperatures. With DPPDS, annealing tended to result in slight decreases in J_{SC}, but a concomitant increase in FF resulted in greater overall performance. These fabrication conditions resulted in average PCEs of 1.53±0.04% for DPPS and 0.84±0.04% for DPPDS. In our hands, when $PC_{71}BM$ was used as an acceptor, no improvement in PCE was observed, which is probably due to increased phase separation with the decreased solubility of $PC_{71}BM$

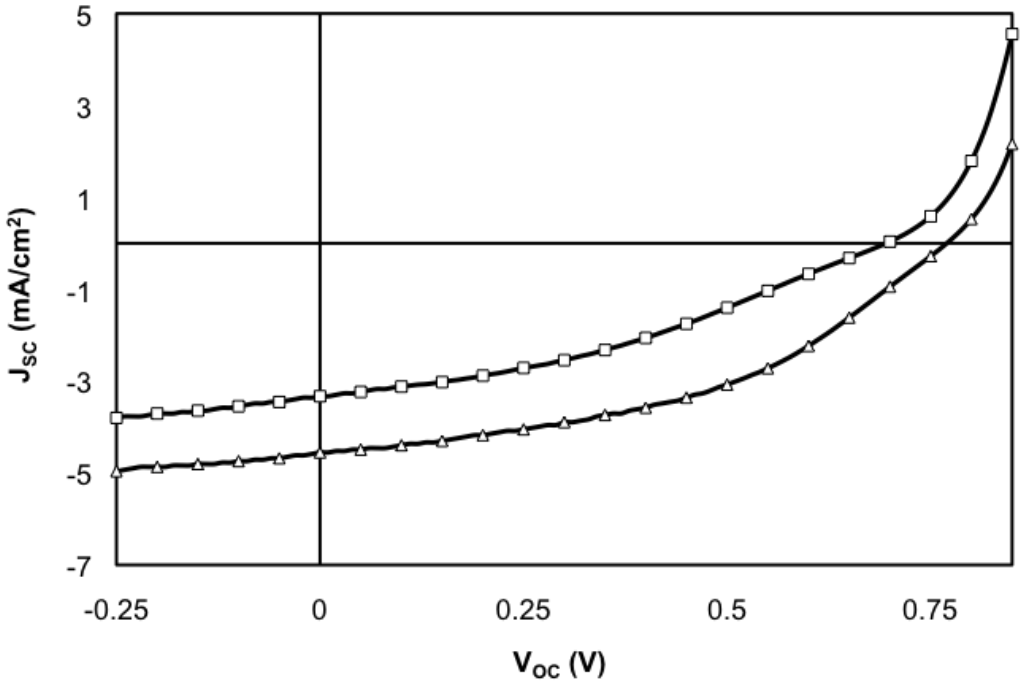

Figure 11: J-V characteristics for solar cells prepared with an active layer of $PC_{61}BM$ and DPPS (triangle) or DPPDS (square) under simulated AM 1.5G irradiation (100 mW/cm^2).

Table 2: Photovoltaic characteristics of best devices made from blends of DPPS or DPPDS and $PC_{61}BM$.

	V_{OC} (mV)	J_{SC} (mA/cm^2)	FF	PCE (%)
DPPS	766±13	4.9±0.3	0.41±0.02	1.53±0.04
DPPDS	696±16	3.4±0.2	0.36±0.01	0.84±0.04

The photovoltaic properties for DPPS are consistently higher than those of DPPDS, even though the greater π-conjugation length of DPPDS results in a broader absorption band that extends to the edge of the visible wavelengths and increases the molar absorptivity. The decrease in V_{OC} with increasing selenophene content of the

highest efficiency devices is consistent with the increasing HOMO levels of these molecules from -4.95 eV for DPPS to -4.85 eV for DPPDS. The short circuit current density (J_{SC}) varies consistently with both the external quantum efficiency (EQE) and the mobility (μ) for each material, as discussed below.

Figure 20 presents the EQE curves for devices fabricated with DPPS and DPPDS under optimized device performance conditions, with LiF/Al top contacts. Peak EQEs of approximately 25% at both 630 and 690 nm were found for DPPS. The EQE for DPPDS is significantly reduced to 19% at 650 nm. Hole only mobilities of both materials were examined through organic thin film transistors (OTFTs) in the top contact geometry. DPPS had a hole mobility of 4×10^{-5} cm^2/Vs and DPPDS showed a hole mobility of 2×10^{-5} cm^2/Vs. We attribute the lower PCE and EQE of the DPPDS devices, despite the extended absorption wavelength and greater absorption coefficient, to the lower hole mobility observed in these thin films. Our DFT calculations (details in Appendix X) show that DPPDS has the most planar structure, followed by DPPS, and finally SMDPPEH. Based on molecular packing, we would expect DPPDS to show the greatest hole mobility, but the opposite trend is observed. We attribute the decreased mobility to the film morphology rather than the molecular packing, where the formation of large crystallites leads to decreased uniformity and increased surface roughness in the thin film.[96] Increased grain boundaries may also play a role in the poor OTFT performances.[96]

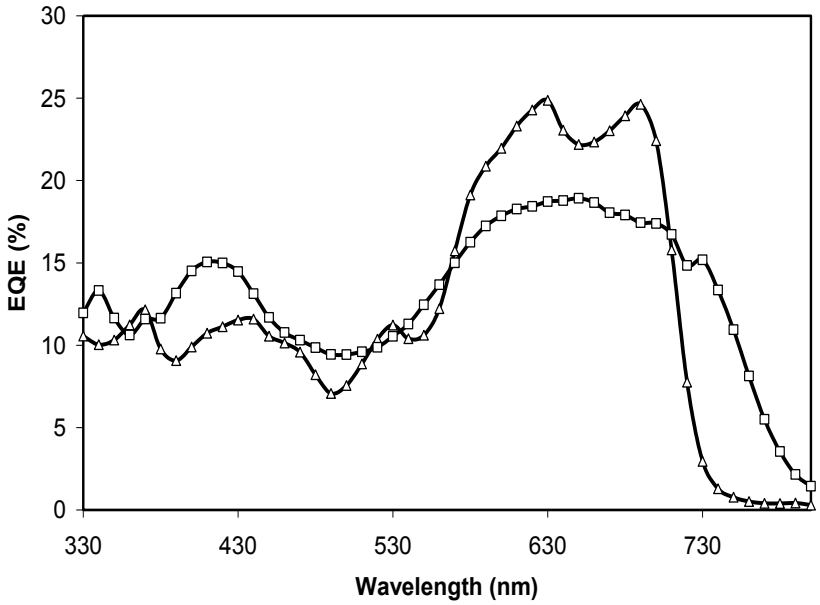

Figure 20: External quantum efficiency (EQE) curves for blends of DPPS:$PC_{61}BM$ (triangle) and DPPDS:$PC_{61}BM$ (square).

The thin film morphology of the OPV active layer was also examined for discussion of the lower PCE of DPPDS, as it is known to affect the overall device performance in BHJ solar cells. As can be seen in Figure 21, both active layers have similar morphologies with domains around 100 nm in diameter, and both are characterized by high rms roughness values of 10 nm for DPPS and 9 nm for DPPDS. The large domains and high rms roughness values may limit the overall device performance of our selenophene derivatives as compared to the SMDPPEH analog of Nguyen, et al.,[93] as the domains are larger than the optimal separation required for efficient exciton diffusion. Additional investigation of device performance when depositing active layers with solvent mixtures may help improve the morphology of the active layers.

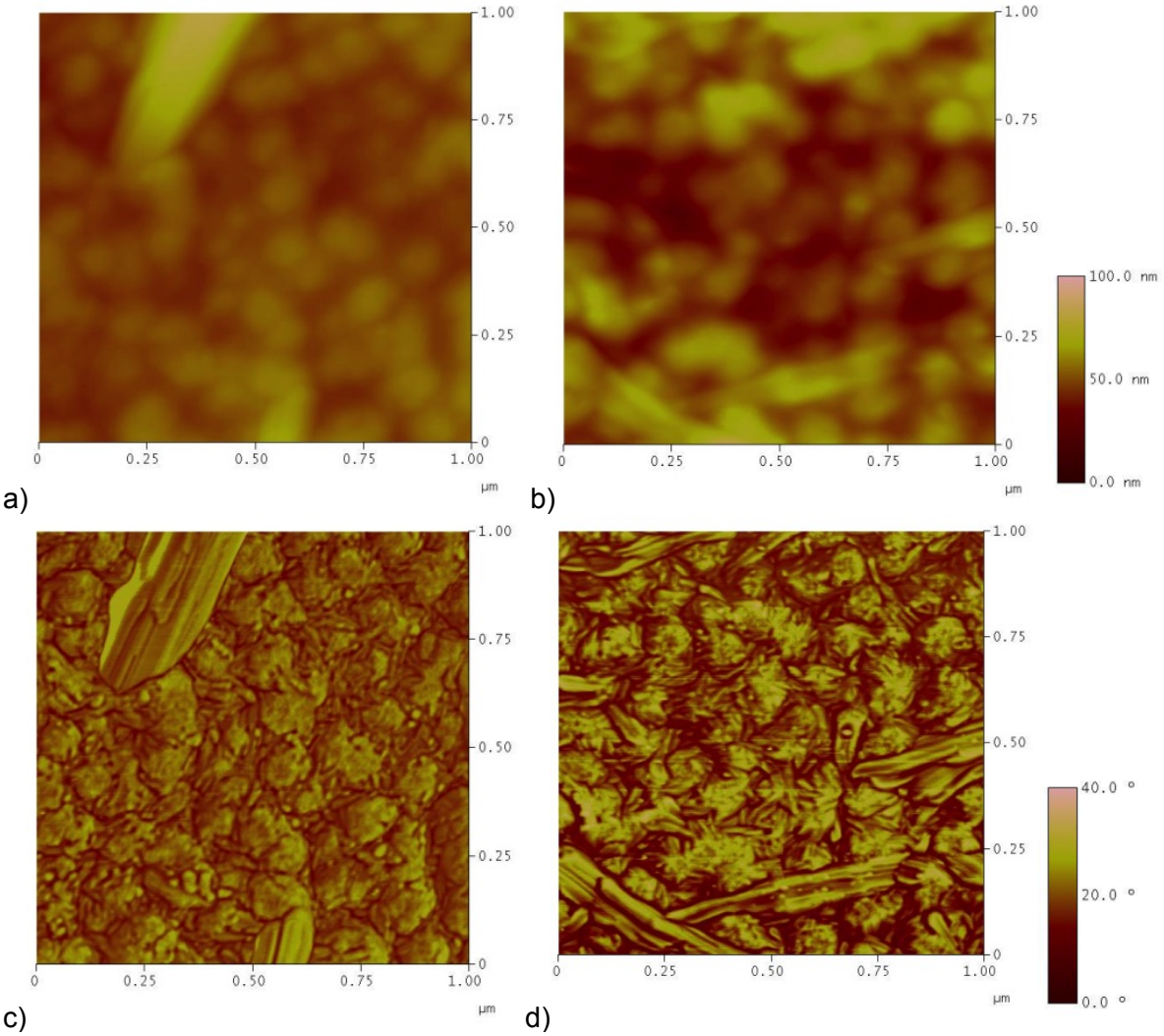

Figure 21: AFM height images of (a) DPPS:PCBM active layer between electrodes and (b) DPPDS:PCBM active layer between electrodes. AFM phase images of (c) DPPS:PCBM and (d) DPPDS:PCBM active layers.

2.4 Conclusions

The characterization of novel low band gap oligoselenophenes functionalized with a diketopyrrolopyrrole core was presented, which were the first reported oligoselenophenes used in molecular bulk heterojunction solar cells. These chromophores exhibit a broad optical absorption that is induced by the internal electron transfer between the selenophenes and the DPP core. Solar cells fabricated with DPPS and DPPDS show peak EQEs of 25% and 19%, and OTFT hole mobilities of 4×10^{-5}

cm^2/Vs and 2×10^{-5} cm^2/Vs, respectively. Under optimized fabrication conditions, solar cells consisting of an active layer of DPPS:$PC_{61}BM$ and DPPDS:$PC_{61}BM$ resulted in average PCEs of 1.53±0.04% and 0.84±0.04%. Further improvements to the overall device efficiencies may be realized through the optimization of film morphology to improve hole mobilities as well as charge dissociation.

Chapter 3: Conjugated P-Type Brush Copolymers Comprising a Donor-Acceptor Backbone and Poly(3-hexylthiophene) Sidechains Synthesized Via a "Graft Through" Approach

3.1 Motivation/Introduction

Although the efficiencies of organic photovoltaics (OPVs) are increasing, one drawback of conjugated polymers is that they tend to have narrow absorption bandwidths, leading to losses from some combination of excitonic thermalization or sub-bandgap transmission.[97] The former occurs when an electron is excited beyond the LUMO of the donor and relaxes toward the LUMO during exciton diffusion by releasing energy in the form of photons or phonons. The latter results when photons with energies smaller than the bandgap of the donor are transmitted through the device; this is a direct consequence of the requirements for energy level alignment between the donor, acceptor and electrodes to achieve efficient charge transfer between materials, which places a finite limit on the size of the donor band gap.

One strategy to address these problems simultaneously is to utilize a tandem solar cell, which is composed of two (or more) photovoltaic cells, typically connected in series.[98] These two cells possess donor/acceptor materials that exhibit complimentary absorption spectra to cover the majority of the visible spectrum; generally, poly-3-hexylthiophene (P3HT) is used in conjunction with smaller band gap donors. Any higher energy photons are absorbed by P3HT, thereby limiting thermalization losses;

conversely, any lower energy photons are absorbed by the low band gap material, thus alleviating sub-band gap transmission. However, introducing an interconnecting layer between the two cells introduces its own loss mechanisms and resistances. In addition, since the cells are connected in series, the J_{sc} is limited by the smallest J_{sc} of the two cells. As a result, tandem OPVs have been limited to achieving similar champion efficiencies (10.6%)[99] to single-junction OPVs (~10%).[100]

Another strategy to address transmission and thermalization losses without the complicated fabrication inherent to tandem OPVs is the use of ternary blends of materials in a single-junction bulk heterojunction (BHJ).[101] This method involves adding both a small band gap donor and a wide band gap donor to an n-type acceptor, which is intended to extend the absorption window of the BHJ and thereby improve photon harvesting and the overall J_{sc} of the device. In addition, having a cascade of energy levels in the three BHJ materials has been shown to enhance exciton dissocation efficiencies, which is another major hindrance to achieving high PCE values in OPVs.[102] Such devices have exhibited impressive performances compared to control cells composed of the basis donor materials.[103]

However, conjugated polymers suffer from inherently low dielectric constants compared to inorganic materials. Thus, polymers generate excitons (coulombically-bound electron-hole pairs) upon light absorption, whereas inorganic materials yield free charge carriers.[104] To form free charge carriers, excitons must diffuse through the polymer phase to reach a donor-acceptor interface, where the energetic offset of the lowest occupied molecular orbital (LUMO) levels of the two materials can facilitate exciton dissociation. Unfortunately, the diffusion length of an exciton is small (ca. 10

nm), which means that recombination is a major loss pathway in OPVs. So far, nanostructured active layers with domain sizes on the order of the diffusion length are the best method to mitigate this loss; the BHJ architecture has remained the most practical way to maximize exciton dissociation efficiency.[105] There have been attempts to covalently bond p- and n-type materials through conjugated and aliphatic chains to achieve better exciton separation efficiencies.[106,107] Ternary blend BHJ OPVs have also exhibited improved exciton dissociation efficiencies over their component OPVs.[100,108] Like ternary blends, creating a covalent, conjugated linkage between two electronically-active materials with sufficiently offset energy levels could enhance exciton dissociation via stepwise charge separation, but without having to rely on random exciton diffusion processes to promote exciton dissociation. Moreover, if these two materials had complimentary absorption profiles, thermalization and sub-band gap transmission issues could simultaneously be mitigated. To our knowledge, there have been no reports of direct conjugation between two covalently-linked p-type polymers with complimentary absorption.

The following studies were predicated on the idea that it is possible to functionalize a low-band gap p-type donor-acceptor (D-A) polymer with P3HT chains to yield a fully-conjugated brush copolymer that has broadband absorbance across the visible spectrum and can exhibit enhanced stepwise exciton dissociation. Also of interest was the largely unexplored synthetic chemistry involved with generating such a polymer, as well as the eventual effects on the optoelectronic characteristics of the final polymer and whether it would adopt the characteristics of the donor-acceptor polymer, P3HT, or would conflate properties of the individual polymers.

In this chapter, the electronic properties of a fully conjugated brush copolymer comprised of a carbazole (Cbz)/diketopyrrolopyrrole (DPP) backbone and P3HT sidechains are discussed (Figure 22). The polymer was synthesized via a "graft through" approach, wherein a series of boronic ester-functionalized Cbz-P3HT macromonomers with different degrees of P3HT polymerization were synthesized and subsequently polymerized with a DPP comonomer by a Suzuki coupling reaction. The physical, optical, and OFET performances of the brush copolymers are reported.

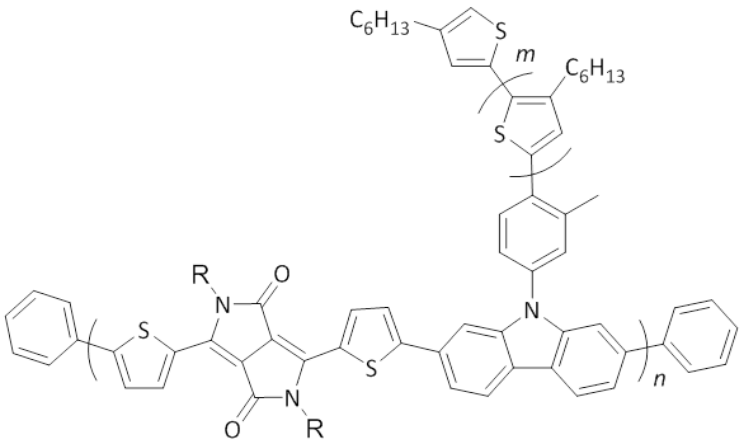

Figure 22. Target conjugated comb copolymer structure.

3.2 Experimental

3.2.1 Polymer synthesis

All polymers were used as received without further purification, as synthesized by David Zeigler. All chemicals were purchased from Aldrich and used without further purification. Solvents for synthesis were purified by distillation. All chemical reactions were carried out in a nitrogen atmosphere. Briefly, dibromocarbazole was functionalized

at the N position with a chlorotoluene P3HT initiator. The carbazole was then functionalized with boronic esters in place of Br prior to catalyst insertion on the chlorotoluene substituent. Grignardized 2-bromo-3-hexyl-5-iodothiophene monomer was then added to produce externally initiated P3HT. The resulting polymers were referred to as the carbazole-P3HT (CP) macromonomers, and series of four were fabricated with degrees of polymerization (DP) of DP 10, 20, 40, and 75. Each of these

Scheme 1: *i*) CuI, 1-chloro-4-iodo-2-methylbenzene, 1,10-phenanthroline, K_2CO_3, DMF, 125 °C, 16 h, 38%; *ii*) a) *n*-BuLi, THF, -78 °C, 1 h, b) 2-isopropoxy-4,4,5,5-tetramethyl-1,3,2-dioxaborolane, r.t., overnight, 76%; *iii*) a) $Ni(COD)_2$, PPh_3, toluene, 50 °C, 3 d, b) 1,3-bis(diphenylphosphino)propane, r.t., 3 h, c) 2-bromo-5-magnesium chloride-3-hexylthiophene; *iv*) a) 3,6-bis(5-bromothiophen-2-yl)-2,5-bis(2-octyldodecyl)pyrrolo[3,4-c]pyrrole-1,4(2H,5H)-dione, 18-crown-6, Aliquat 336, $Pd(PPh_3)_4$, toluene, 2M K_2CO_3, 110 °C, 3 d, b) phenylboronic acid, 110 °C, 12 h, c) bromobenzene, 110 °C, 12 h. *v*) a) 3,6-bis(5-bromothiophen-2-yl)-2,5-bis(2-octyldodecyl)pyrrolo[3,4-c]pyrrole-1,4(2H,5H)-dione, 18-crown-6, Aliquat 336, $Pd(PPh_3)_4$, toluene, 2M K_2CO_3, 110 °C, 3 d, b) phenylboronic acid, 110 °C, 12 h, c) bromobenzene, 110 °C, 12 h.

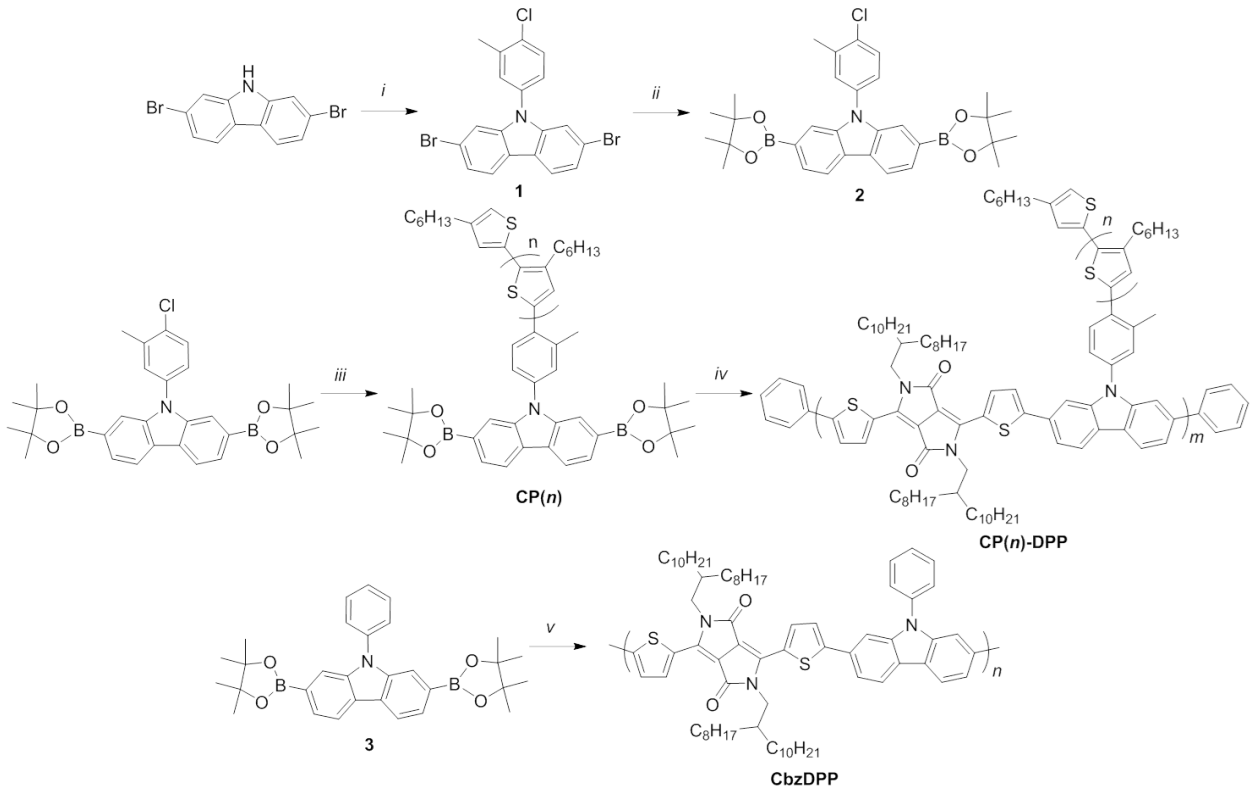

CPs were then copolymerized with a diketopyrrolopyrrole (DPP) monomer, resulting in a series of CP(n)-DPP brush copolymers, where n corresponds to the DP of the P3HT chain. A schematic of these reactions can be found in Scheme 2.

3.2.2 Characterization

UV-Vis spectra were tested using a Perkin-Elmer Lambda-9 spectrophotometer. All AFM images were recorded in tapping mode on a Nanoscope II Scanning Probe Microscope (Digital Instruments). All DSC thermograms were recorded on a TA Instruments Q20 DSC.

3.2.3 OFET device characterization

Organic field-effect transistors were fabricated in a top-contact bottom-gate device geometry on heavily doped p-type silicon <100> wafers with a 300 nm thermal oxide layer, purchased from Montco Silicon Technologies. Substrates were cleaned by sequential ultrasonication twice with fresh acetone, followed by isopropyl alcohol for 15 min each. They were then dried under a stream of nitrogen and treated by air plasma for 15 minutes before passivating the oxide layer with a thin divinyltetramethyldisiloxane-bis(benzocyclobutene) (BCB, Dow Chemicals, Inc.) buffer layer. A precursor solution of 1 wt% BCB in toluene was spin coated in air at 4000 rpm for 60 sec on the oxide layer. The substrates were subsequently annealed at 250 °C over night in a glove box. Solutions of each polymer were prepared in chloroform ($CHCl_3$) and chlorobenzene (CB) at concentrations of 5 mg/mL and allowed to stir in a glovebox over night before filtering with a 0.2 um PTFE filter. Filtered solutions were

then spin coated on BCB passivated substrates at 2000, 3000, or 4000 rpm for 60 sec. The best device performances were found for OFETs made in $CHCl_3$ and spin coated at 2000 rpm. These thin films were annealed at 65, 95, 125, and 155 °C for 10 min under nitrogen prior to electrode deposition in order to determine their optimal device performance conditions. Gold source and drain electrodes were thermally evaporated through a shadow mask at a base pressure of 7 x 10^{-7} Torr at a rate of 1 Å/s to a thickness of 50 nm. The output and transfer characteristics of all transistors were measured in a nitrogen atmosphere using an Agilent 4155B semiconductor parameter analyzer. The field-effect mobility (μ) was determined from a linear fit of $(I_{ds})^{1/2}$ vs V_{gs} in the saturation regime. The threshold voltage (V_t) was estimated from the x-intercept of the linear region of $(I_{ds})^{1/2}$ vs V_{gs}. All devices had a channel length of 100 μm and a width of 1000 μm.

3.3 Results and Discussion

3.3.1 UV-Vis Absorbance

The absorbance characteristics of the comb copolymers were characterized by UV-visible spectroscopy, the results of which can be found in Figure 23 a) in solution and b) thin film, with the solution spectrum of the CbzDPP copolymer for reference in each case and all copolymer response normalized to the P3HT contribution maximum absorption. Generally, each comb copolymer possesses a P3HT π-π* transition around 400-450 nm and a CbzDPP donor-acceptor intramolecular charge transfer (ICT) peak from 550 nm to greater than 800 nm. The ICT peak of the linear CbzDPP polymer has two main peaks (ca. 650 and 710 nm), which are also reflected in the bimodal ICT peaks of the comb copolymers, except CP(75)-DPP, which shows a small ill-defined

ICT peak. Thus, as hypothesized, the carbazole produces a sufficient break in conjugation to realize the optical properties of both components.

There is a clear trend in the intensity, shape and onset of the ICT peak in the comb copolymers as the P3HT length is varied. As the P3HT side chain was shortened, the ratio of the P3HT π-π* transition intensity to the donor-acceptor ICT peak decreased; conversely, the longer P3HT chains resulted in a more intense P3HT π-π* transition. There could be several explanations for this. First and foremost, the CP(40)-DPP and CP(75)-DPP polymers contain additional neat P3HT due to how they were worked up (the long polymer chains did not allow for purification by silica gel chromatography and were subjected to purification by soxhlet extraction instead, leaving behind neat P3HT), which accounts for some of their absorption around 450 nm. This P3HT also results in non-equimolar monomers, which limits the polymerization length and the resultant ICT intensity. It is also possible that the relative amount of

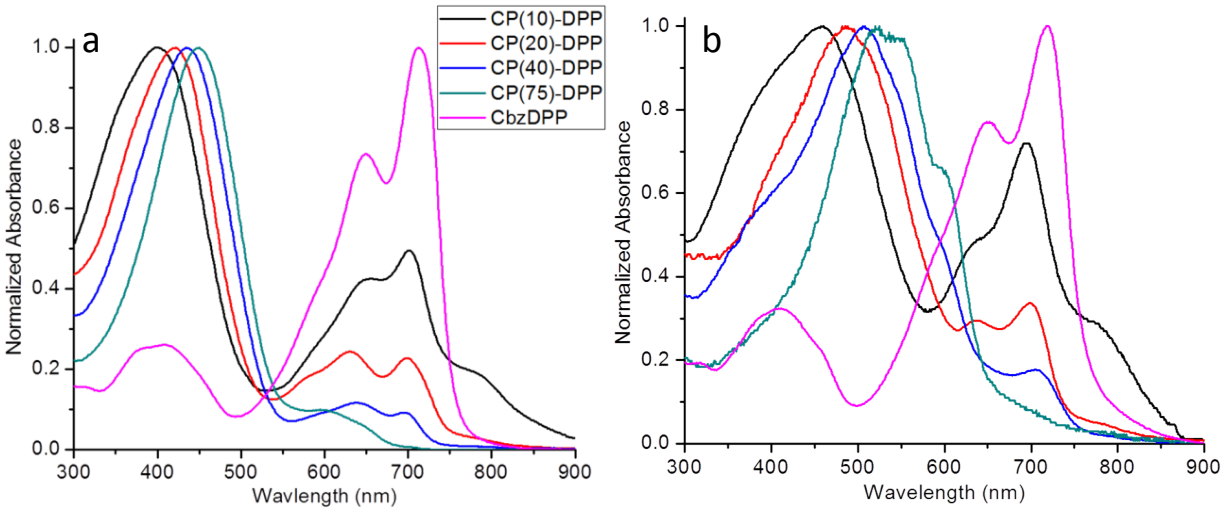

Figure 23: a) UV-visible $CHCl_3$ solution spectra for CP-DPP comb copolymers, with CbzDPP donor-acceptor absorbance for reference, b) Thin film absorption spectra for comb copolymers and CbzDPP. Films were dropcast from $CHCl_3$ solutions

P3HT and donor-acceptor polymer dictates the absorption profile – i.e., as the P3HT chain becomes shorter and the π-π* transition becomes weaker, the donor-acceptor peak becomes more prominent and *vice versa*. The longer CP macromonomers undoubtedly produce more steric congestion during the Suzuki polymerization and limit the length of the donor-acceptor polymer.

Regardless, there is clearly an inverse relationship between the length of the CP macromonomers and the onset and relative intensity of the ICT peak in the comb copolymers. This trend is supported by results from recent studies on D-A copolymers incorporating thienylated benzodithiophene donors, which have shown that adding two or three pendant thiophene rings to the donor generates an increasingly strong electronic transition around 400 nm.[109] Also of interest is that the ICT peaks of CP(10)-DPP and CP(20)-DPP both exhibit a shoulder at longer wavelengths. The thin film absorbance showed similar trends compared to the solution measurements, along with a slight broadening of the peaks and bathochromic shifts of both the P3HT π-π* transition and ICT peaks, as we would expect with a higher degree of order in the solid state.

3.3.2 Differential Scanning Calorimetry

The thermal behaviors of the polymers were characterized by differential scanning calorimetry (DSC). Figure 24 shows typical thermograms of each material. CbzDPP shows a melting point (T_m) of 231 °C. The CP(n)-DPP polymers show increasing melting temperatures of 217, 211, 180, and 174 °C with increasing P3HT length. It is known that longer P3HT chains exhibit stronger intermolecular interactions than shorter P3HT chains, which would explain the increasing T_m values with increasing

molecular weight.[110] This stronger intermolecular interaction is also reflected in the thin film absorption spectra. As the P3HT chains increase in length, there appears a more defined low-energy vibronic shoulder on the main P3HT π-π* transition, which results from ordered packing in the solid state. Also of note is that CP(10)-DPP possesses a second T_m at 215 °C, which is likely due to the higher proportion of CbzDPP in the final graft polymer.

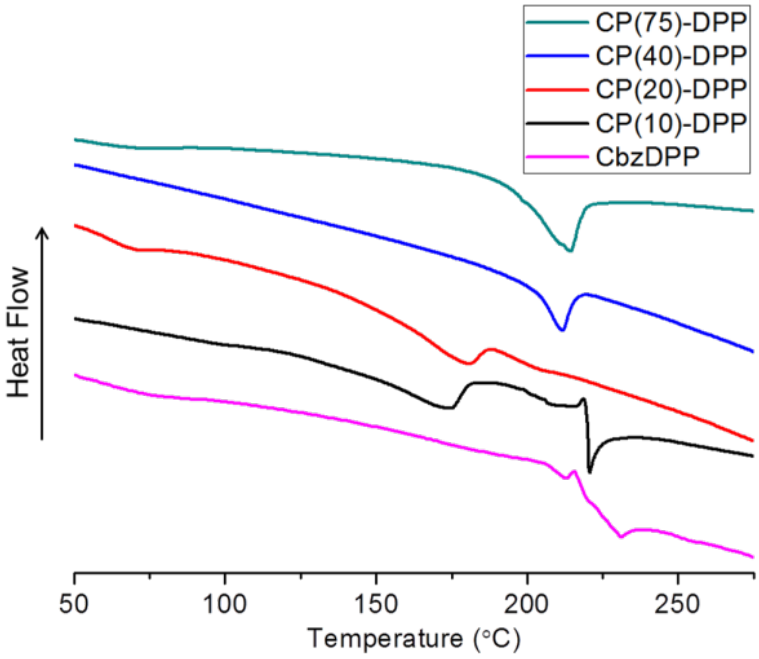

Figure 24: Differential scanning calorimetry of CP-DPP comb copolymers and CbzDPP.

3.3.3 OFET Characteristics

Finally, the free-charge carrier mobilities of each polymer were determined from organic field effect transistors (OFETs), and the microstructures of the optimized OFETs were characterized by AFM. To fabricate optimized OFET devices, the spincoating solvent, spincoating speed, and annealing temperature were varied. Chloroform and chlorobenzene were examined as solvents, and both yielded smooth and continuous films, but chloroform tended to lead to films with higher mobilities. Spincoating speeds

of 4000, 3000 and 2000 rpm were tested; the 2000 rpm spin speed yielded the thickest films and slightly higher mobilties than the thinner films formed with a spin speed of 3000 rpm. Finally, the films were annealed at 65, 95, 125, and 155 °C. The CbzDPP polymer exhibits a high T_g, and responded best to the 155 °C treatment, whereas films of the comb copolymers had the highest mobilities upon annealing at 65 °C. Optimized devices were therefore processed from chloroform, spun at 2000 rpm, and annealed for 10 minutes, with the CbzDPP and comb copolymers being annealed at 65 °C and 155 °C, respectively. The OFET transfer and output curves are shown in Figure 25 a-j.

The optimized OFET mobilities seem to reflect the polymer composition. The device properties of the comb polymers with P3HT suffered relative to those of the neat CbzDPP polymer. Both CP(10)-DPP and CbzDPP exhibit similar ambipolar properties, with the addition of the small amount of P3HT only slightly reducing the hole mobility from $7\times10^{-3} \pm 2\times10^{-3}$ $cm^2V^{-1}s^{-1}$ for CbzDPP to $5\times10^{-3} \pm 3\times10^{-3}$ $cm^2V^{-1}s^{-1}$ for CP(10)-DPP. They both have similar electron mobilities of $7\times10^{-4} \pm 2\times10^{-4}$ $cm^2V^{-1}s^{-1}$ for CbzDPP and $7\times10^{-4} \pm 3\times10^{-4}$ $cm^2V^{-1}s^{-1}$ for CP(10)-DPP. The surface morphology of these materials shows reduced domain sizes for CP(10)-DPP relative to CbzDPP, as expected due to an increase in disorder in the P3HT containing system, as could also be predicted by the significant decrease in T_m relative to CbzDPP as evidenced by DSC in Figure 24, as well as the unstructured nature of the P3HT contribution to the UV-Vis spectrum in Figure 23. Further increasing the concentration of P3HT to CP(20)-DPP and CP(40)-DPP results in devices that do not work well for transistor applications, with CP(20)-DPP not turning on and CP(40)-DPP resulting in devices with barely measurable output curves. Further increasing the P3HT concentration to CP(80)-DPP

results in p-type transistors with mobilities of $6\times10^{-4} \pm 1\times10^{-4}$ $cm^2V^{-1}s^{-1}$. This likely arises due to favorable π-π interactions between the longer P3HT chains, as can be expected from the well defined shoulder at ~610 nm in the thin film UV-Vis spectrum. Overall, it

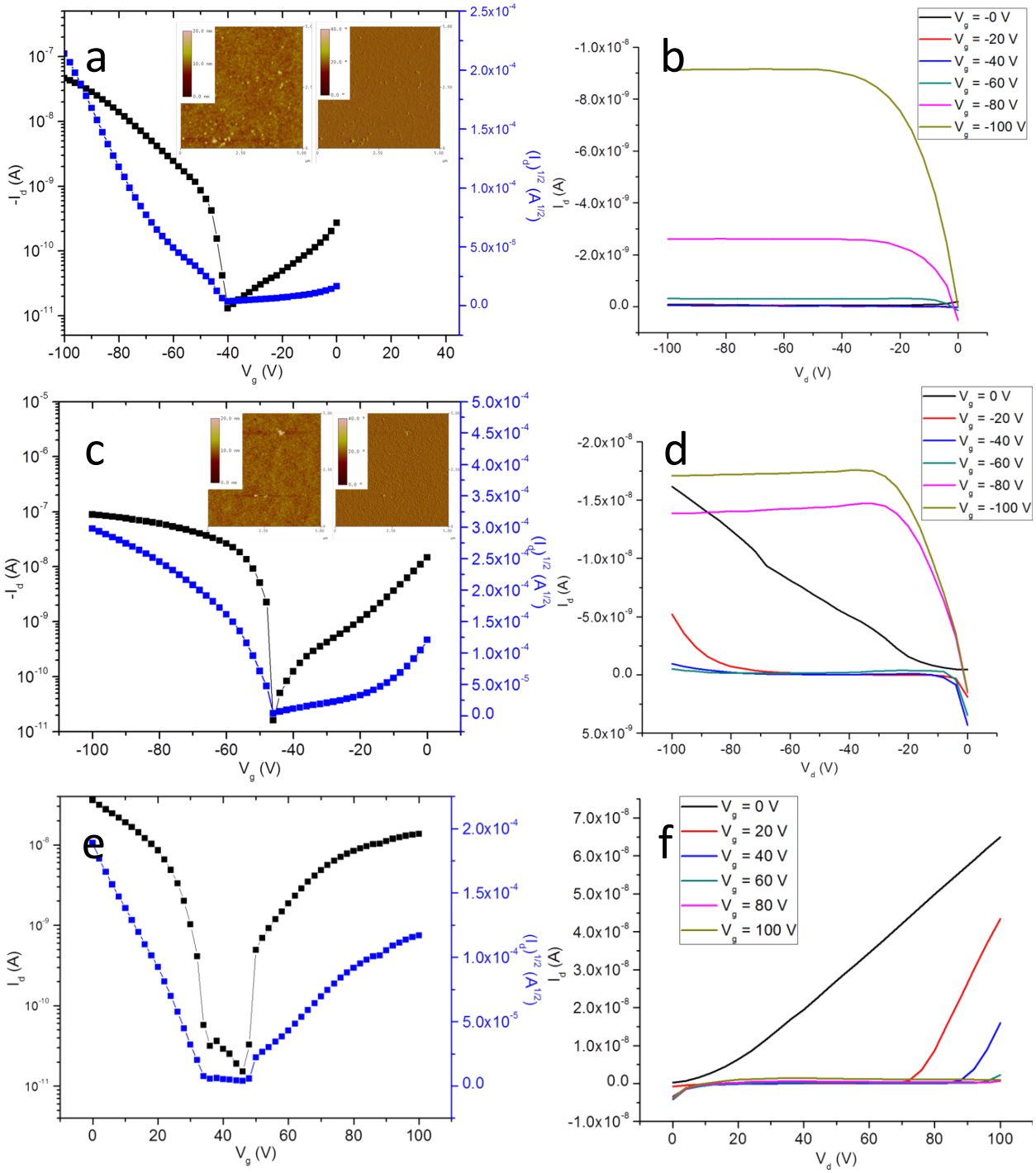

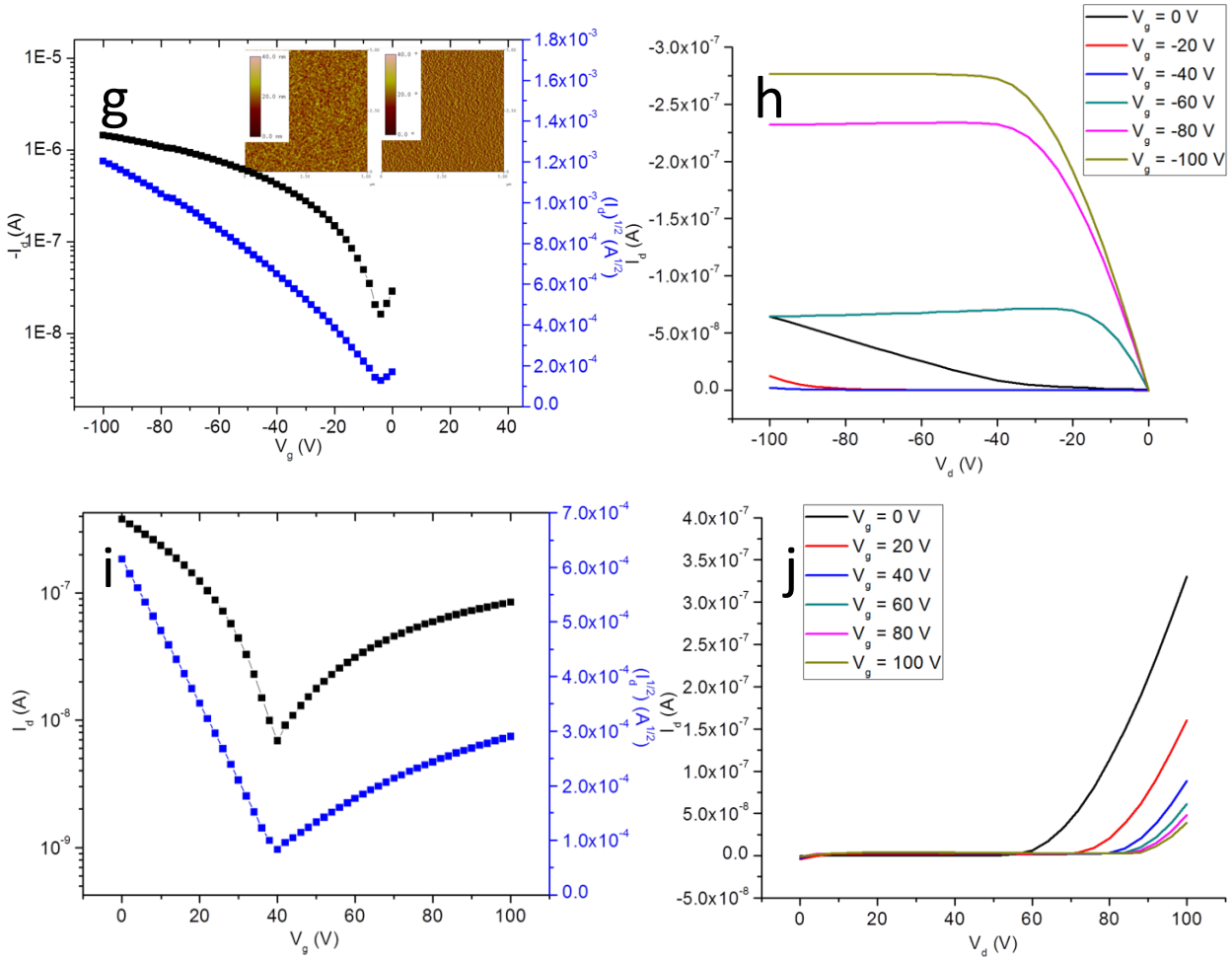

Figure 25: Transfer (left column), AFM surface topologies (inset) and output (right column) curves for a,b) CP(75)-DPP, c,d) CP(10)-DPP in the p-type regime, e,f) CP(10)-DPP in the n-type regime, g,h) CbzDPP in the p-type regime, and i,j) CbxDPP in the n-type regime.

appears that there is a general trend of transport properties being derived from the CbzDPP backbone with low P3HT chain lengths, followed by a disruption in the electronic structure with higher concentrations of P3HT, before the transport properties become dominated by P3HT interactions.

3.4 Conclusion

In this study, a series of four carbazole-P3HT-diketopyrrolopyrrole, or CP(n)-DPP, brush copolymers with different degrees of P3HT polymerization were synthesized via a “graft through” approach. These polymers were designed to be fully conjugated brush copolymers that have broadband absorbances across the visible spectrum and that can exhibit enhanced stepwise exciton dissociation. The physical, optical, and OFET performances of these materials were then characterized to determine how the copolymerization affected the polymer performance. From the UV-Vis, it was found that the intensity of the intermolecular charge transfer peaks that can be attributed to the low band gap backbone polymer diminishes with increasing P3HT chain length. However, the structural similarity of the ICT peaks for each of the polymers indicates that there is a sufficient break in conjugation to realize the optical properties of each component. An increase in the P3HT chain length on the copolymer resulted in the signal from the P3HT π-π* transition becoming red shifted and developing a more pronounced vibronic structure, as is expected with increased order in the solid state. This was also reflected in the increasing melting temperature with increasing P3HT length, as determined by DSC. The brush copolymer with the shortest P3HT chain, CP(10)-DPP, showed two melting temperatures, which was attributed to the higher proportion of the Cbz-DPP backbone. Transistors made from these materials showed the general trend of the charge transport properties of the brush copolymers primarily being derived from contributions from the Cbz-DPP backbone with low DP of P3HT, followed by disruption of the molecular order with increasing P3HT chain length, before becoming dominated by the P3HT charge transport characteristics.

Chapter 4: Surface-Initiated Synthesis of poly(3-methylthiophene) from Indium Tin Oxide and its Electrochemical Properties

4.1 Introduction

Conjugated polymers (CPs), especially poly(3-alkylthiophene)s (P3ATs), are a widely researched class of materials due to their desirable electronic and physical properties, with applications including solar cells, light emitting diodes, and sensors.[54,111–120] In each of these applications, compositional and energetic control at the organic−inorganic interface can facilitate both charge injection and charge transport.[121,122] In particular, organized layers of P3ATs tethered to metal or metal oxide electrical contacts are of interest for the optimization of charge injection and charge harvesting processes in organic electronics. Surface immobilization of conjugated polymers directly on OPV electrodes, such as ITO, may potentially improve transport properties by providing clear pathways for charge transport in the direction normal to the substrate, in addition to aiding in the formation of optimized bulk heterojunction architectures when infiltrated with a second component, and improving charge injection rates due to the nature of the covalent attachment.[122–127]

Surface grafted polymer films and polymer brushes are typically prepared utilizing either “grafting to” or “grafting from” approaches. The “grafting to” approach proceeds through the attachment of preformed polymer chains to the substrate. This method suffers from low grafting density and poor control over film thickness due to increased hindrance for surface attachment.[128] The requirement for polymer chains to

diffuse through an existing attached polymer layer to reach the reactive site severely limits the grafting density and results in thin polymer films of typically less than 10 nm.[129] The "grafting from" approach has thus become the preferred method and has been used to prepare thick surface-immobilized polymer films.[130] This method utilizes a surface bound initiator for *in situ* chain growth polymerization. Techniques for preparing "grafted from" polymers via surface initiated polymerization such as RAFT,[131–134] ROMP,[135–137] ATRP,[138–142] Suzuki and Yamamoto polycondensation,[143,144] and more recently the KCTP method[145–152] have been documented. Yokozawa[153,154] and McCullough[155] first pioneered the Kumada catalyst transfer polymerization and the Grignard metathesis (GRIM) techniques, respectively, using the 1,3-bis(diphenylphosphino)propane nickel(II) chloride [Ni- (dppp)Cl_2] catalyst with Grignard-type monomers, which yield highly regioregular polymers with controlled molecular weights, narrow dispersities, and uniform end groups. Our group, among others, has reported the synthesis of externally initiated polymers in solution.[156–159]

Previously, we had investigated the versatility of aryl halide initiators functionalized with a phosphonate moiety and observed a good percentage of headgroup incorporation, controlled molecular weight, and dispersity for poly(3-hexylthiophene) synthesized from a phenyl-based initiator with an ortho substituent,[160] and we speculated that a high level of polymerization control would carry through during the surface modified KCTP technique. The key aspect of KCTP is that it proceeds via a chain growth mechanism where the unique propensity of the Ni catalyst to undergo intramolecular ring walking leads to the addition of only one monomer unit at a time. This method is in sharp contrast with more common step-growth polymerization

techniques, which fail to produce conductive polymer brushes of reasonable thickness, which is primarily due to the random coupling of monomer units which leads to polymer precipitation in the reaction solution, thus hindering surface growth. Kiriy and co-workers applied the KCTP approach to grow 40−70 nm thick semiconducting poly(3-hexylthiophene) brushes from surface immobilized Ni(II) poly-4-bromostyrene (PS(Br)) macroinitiators.[145] It was observed that a maximum reachable thickness of the P3HT deposits is directly proportional to the thickness of the supporting PS(Br) layers and suggested that grafting occurs inside the PS(Br) films in addition to the topmost layer.[147] Locklin and co-workers have reported the polymerization of several Grignard monomers prepared from the corresponding 1,4-dihalobenzenes from a thienyl bromide monolayer resulting in surface bound films with thicknesses up to 30 nm,[151] as well as fabrication of poly(phenylene) and poly(thiophene) films with thicknesses up to 50 nm.[150] Recently, the same group has fabricated several (aryl)Ni(II)-Br KCTP initiators on various planar substrates, investigated the initiator density, homogeneity, and stability, and synthesized 40−65 nm thick P3MT films from functionalized SiO_2 and ITO surfaces.[152] While these existing studies on the surface initiated polymerization of poly(3-alkylthiophenes) have certainly demonstrated the feasibility of the KCTP approach, in order to realize the potential applications of these surface-grafted films in organic electronics, additional polymerization control parameters must be actualized.

Herein, we report the synthesis of surface-grafted poly(3- methylthiophene) films from ITO substrates functionalized with a phosphonic acid (PA) based initiator monolayer. The film thickness is regulated via monomer solution concentration demonstrating control over polymer growth relative to previous reports.

4.2 Experimental

4.2.1 Synthesis

Materials. All reagents were purchased from Sigma-Aldrich, TCI and Strem Chemicals and used as received unless otherwise stated. THF and toluene solvents were dried using a solvent drying system from Innovative Technologies and degassed using the freeze/pump/thaw method. ITO coated (~100 nm, 15 Ω/square) glass microslides were purchased from Colorado Concepts Coatings, Inc.

4.2.2 Instrumentation

UV–vis spectra were collected on Perkin-Elmer Lambda 9 Spectrophotometer. AFM topography images were recorded in tapping mode with Nanoscope II Scanning Probe Microscope (Digital Instruments).

4.2.3 P3MT Synthesis

P3MT synthesis was performed by Dr. Natalia Doubina and characterization was performed on the thin films as received. A schematic of the P3MT synthesis can be found in Scheme 3. Briefly, our previous work showed that the phosphonate analogue of **1** yields externally initiated polymers with a high percentage of headgroup incorporation.[160] An externally initiated KCTP developed in our group was utilized to produce surface anchored P3MT.[161] An initiator monolayer was formed by immersing the ITO substrates in a phosphonic acid (**1**) solution overnight. The initiator modified substrates were then subsequently immersed in the $Ni(COD)_2/PPh_3$ solution followed by ligand exchange with dppp. The polymerization was initiated by the addition of Grignard functionalized 3-methylthiophene monomer. Multiple rinsing steps with THF and toluene

were performed between each reaction stage to ensure complete removal of physisorbed Ni catalyst. Upon mixing $Ni(COD)_2$ with PPh_3, the solution turns a deep red color to form $Ni(COD)(PPh_3)_2$ complex which undergoes oxidative addition to the Ar–X bond of the initiator.[150] The subsequent ligand exchange of dppp and PPh_3 occurs on a time scale of several hours. Varying concentrations of the 2-bromo-5-chloromagnesio-3-methylthiophene precursor solution were prepared in order to examine the effect of monomer concentration on film thickness and morphology. After polymerization, the transparent ITO substrates developed a reddish color, while control ITO slides that were (a) not previously modified with a phosphonic acid monolayer and (b) modified with an inert benzylphosphonic acid monolayer remained clear and free of polymer coating. Surface polymer films were stable through extensive rinsing with various solvents, sonication in $CHCl_3$ and Soxhlet extraction which is consistent with the film being covalently attached to the surface rather than simply physiosorbed.

Scheme 2: Surface Initiated Synthesis of Poly(3-methylthiophene) Films.

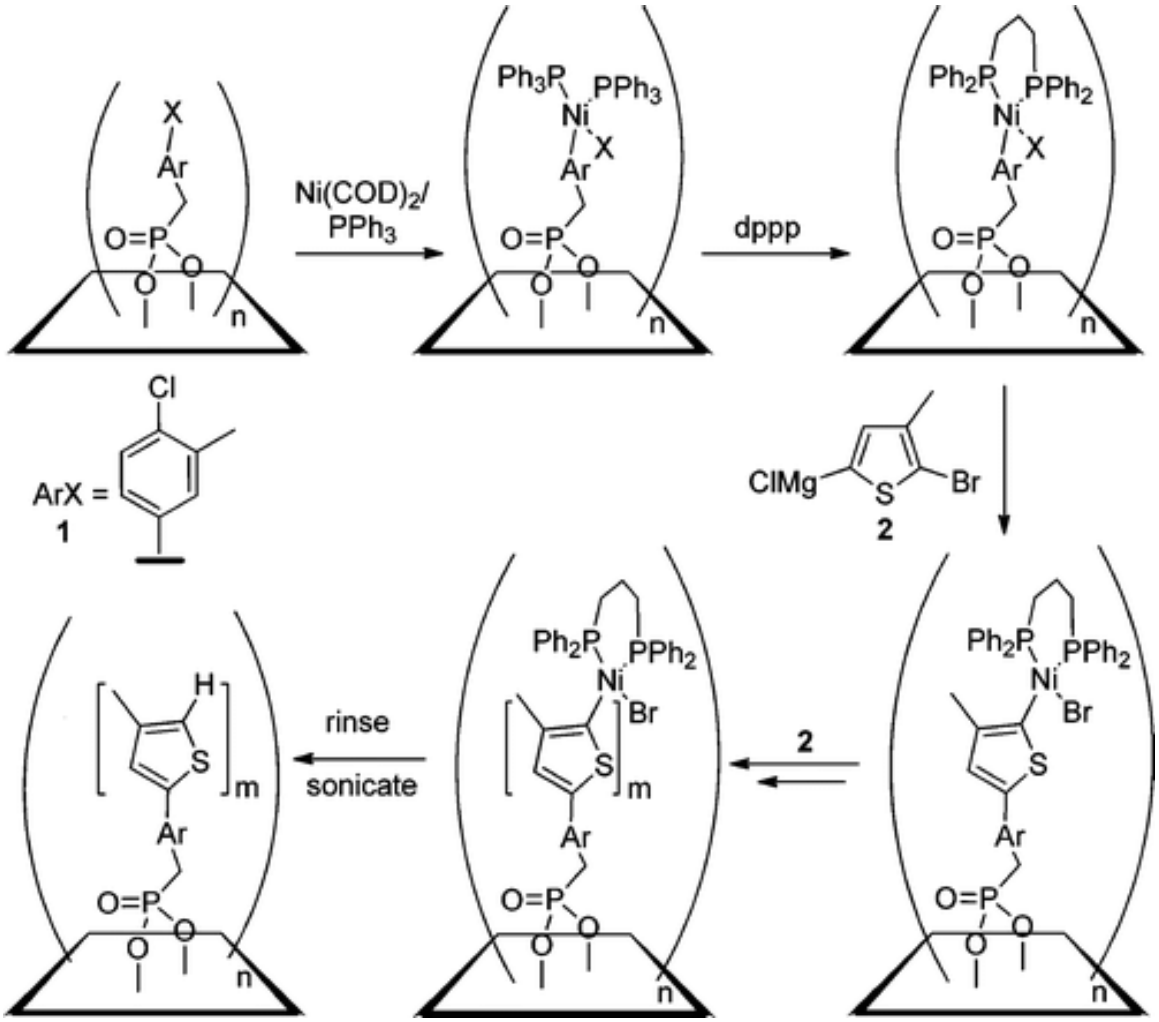

4.3 Results and Discussion

4.3.1 UV-Visible Spectroscopic Characterization

The UV-Vis absorption spectra of solid state P3MT grafts displayed in Figure 26 shows that the absorption intensity of thin films increases with increasing precursor concentration in solution, according to: 0.09 M > 0.05 M > 0.03 M.

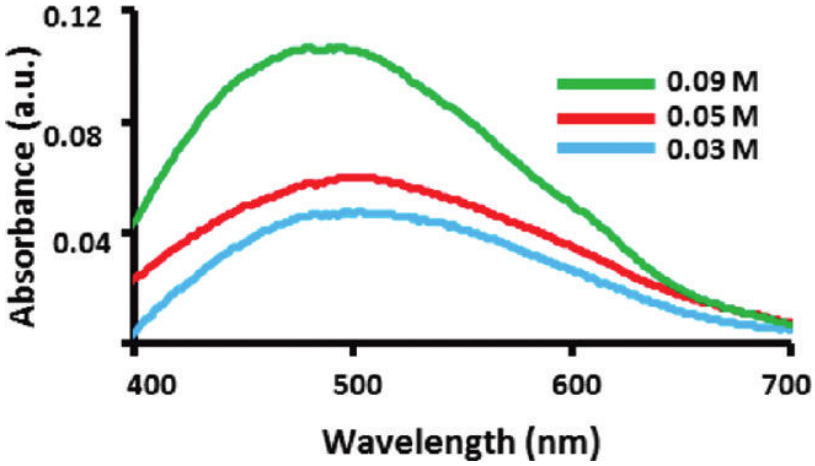

Figure 26: UV-Vis absorption spectra of P3MT films prepared with varying the 3-methylthiophene precursor concentration.

Previous reports have suggested that an increase in the degree of polymerization (DP) of poly(3-hexylthiophene) from 5 to 30 results in the pronounced red shift of the main absorption band from λ_{max} of 420 to 518 nm, which is attributed to differences in energy of π to π* transitions and is directly related to the extent of conjugation, however no significant changes in the maximum absorption peak position were observed for polymer chains with DPs exceeding 30, thus limiting the applicability of this method to accurately analyze chain length.[147] The λ_{max} values for the three different concentration samples were all quite similar (~500 nm), suggesting a scenario where the polymer layers grow to a certain point after which little difference is observed in the absorption spectra. The shoulder appearing around 620 nm in the UV−vis spectrum of the P3MT film prepared with 0.09 M precursor solution implies a certain degree of structural ordering in the film. Absorbance values in the UV−vis spectra are smaller than expected relative to closely packed spin-coated P3HT films of similar thickness due to a lower grafting density for the P3MT chains.

4.3.2 Concentration Effect on Thickness and Morphology

The morphology and thickness of synthesized films were studied via tapping mode atomic force microscopy (Figure 27).

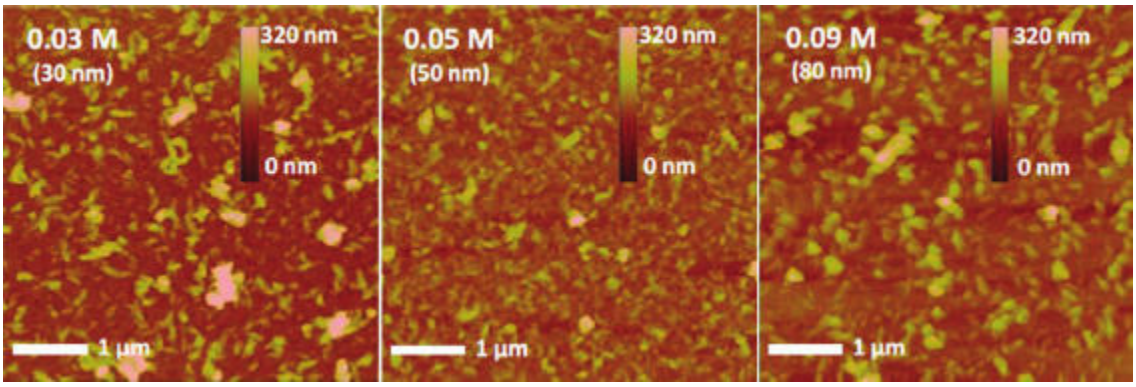

Figure 27: 5 × 5 µm tapping mode AFM images of P3MT films prepared with varying monomer concentration.

Polymer coverage of the substrates is observed in large area height images. The phase images (Figures 28 and 29) also suggest increasing P3MT coverage of the ITO with increasing solution monomer concentration. Phase imaging is a secondary imaging technique of tapping mode AFM that monitors variations in the surface properties of a sample, which may include the elasticity, adhesion, or friction of the surface. The root-mean-square (rms) roughness increased to 20−21 nm after grafting of the polymer films compared to the ∼4 nm roughness of both bare and monolayer modified ITO substrates, which is similar to rms values of grafted films obtained with other Ni(0) mediated condensation polymerization.[144] The high roughness values suggest that polymer chains adopt a collapsed “mushroom” configuration[162,163] likely caused by lower grafting density due to the nature of the bulky initiating species and amplified steric hindrance on the surface. While optical methods, such as ellipsometry, are frequently

used to determine film thickness on reflective substrates, in our case, the optically transparent nature of ITO as well as high surface roughness complicated the use of this technique.[142,164] Additionally, verification of polymer length using size exclusion

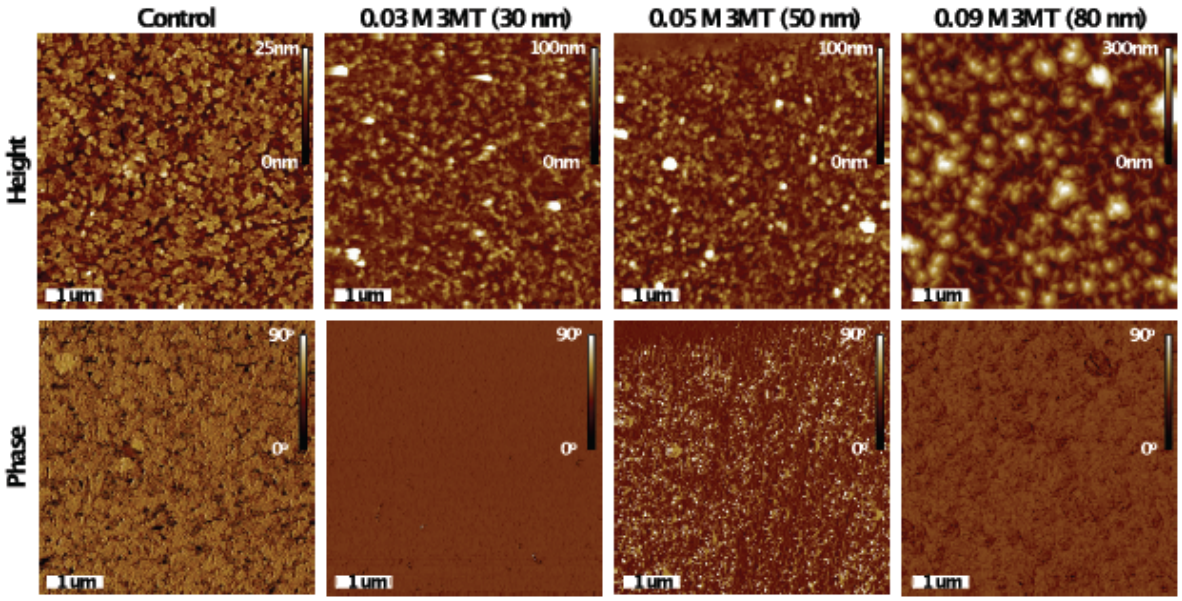

Figure 28: 5 × 5 µm height and phase contrast images for all solution monomer concentrations.

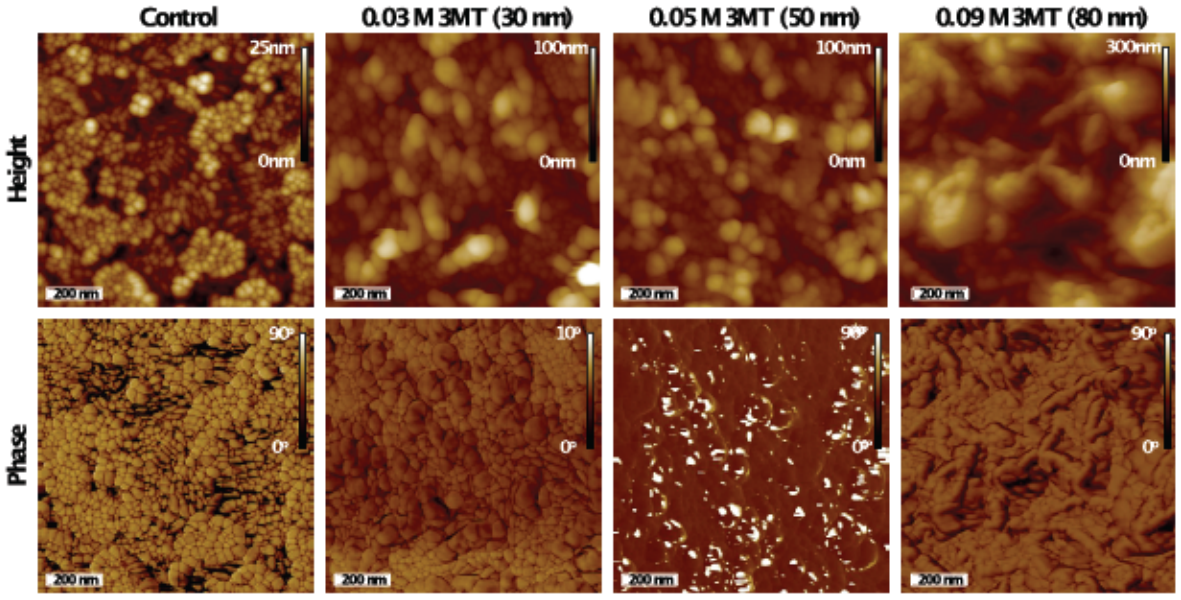

Figure 29: 1 × 1 µm height and phase images for all solution monomer concentrations.

chromatography (SEC) was not possible due to the insolubility of P3MT in common organic solvents. Thicknesses were calculated via AFM profilometry where the films were scratched with a clean sharp blade and multiple stepheight measurements were taken at different points on the substrate, as demonstrated in Figure 30. The average thicknesses increased from 30±1 nm at 0.03 M monomer concentration to 50±3 nm at 0.05 M monomer concentration to 80±3 nm at 0.09 M monomer concentration, where the errors reported are the standard deviations of the thickness measurements. These are thickness values previously reported to be optimal for interlayer films in both organic solar cell and organic light emitting diode platforms.[165]

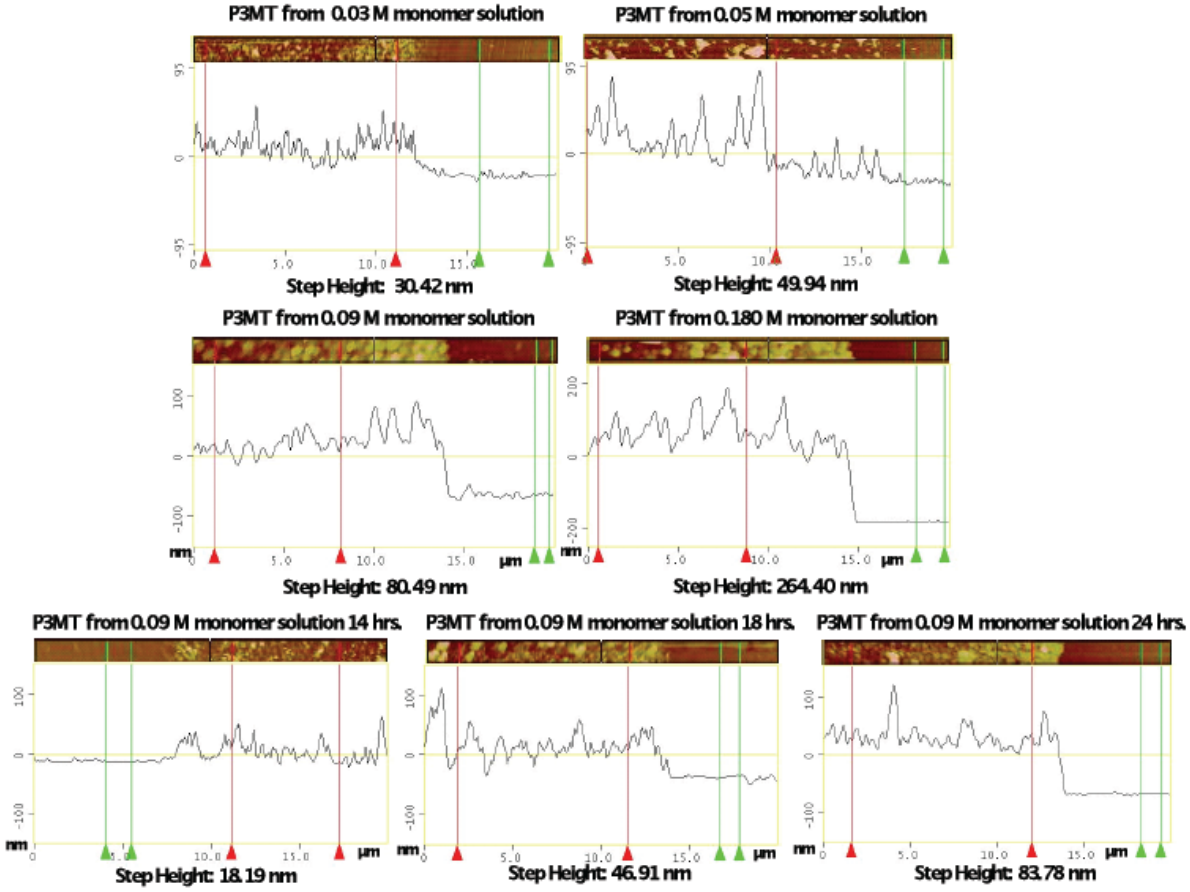

Figure 30: Selected step height line scans.

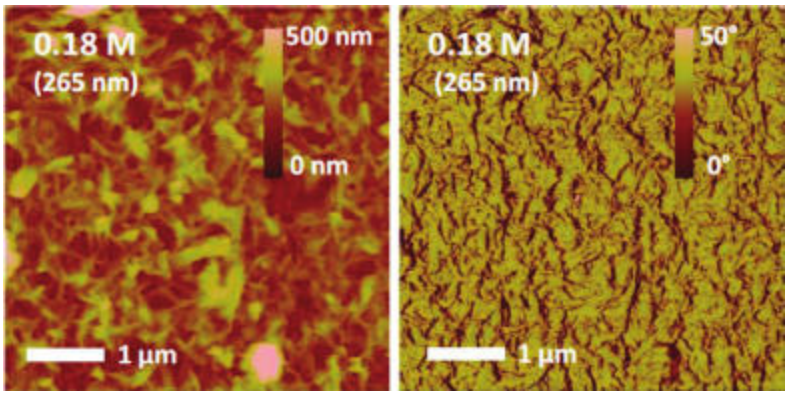

Figure 31: 5 × 5 µm tapping mode AFM height (left) and phase (right) contrast images of P3MT films fabricated with 0.18 M monomer concentration.

In order to investigate whether increasing the monomer solution concentration will further increase the thickness values, P3MT films were fabricated with 0.18 M monomer concentration (Figure 31). Larger globular polymer aggregates are observed in the topography images and the average measured film thickness was calculated to be 265±13 nm. However, the higher surface roughness values and nonuniform films indicate that the polymerization is no longer controlled at this monomer concentration. In contrast to previous synthesis attempts of surface-anchored P3ATs from monolayers on Au, SiO_2 and ITO, which resulted in maximum thicknesses of 5 nm via the "grafting to" method[129] and 65 nm via the "grafting from" method,[166] the P3MT films fabricated with our method appear to be the thickest polymer films synthesized from a single monolayer via KCTP method to date. The thickness values increase linearly with monomer concentration, allowing us to "tune" to a desired thickness.

The effect of monomer concentration on the resulting grafted film/brush thickness was previously observed with SI-ATRP[167,168] and SI-ROMP[169] methods, which are considered true "living" polymerizations. However, until now this has not been realized for the KCTP method. One of the possible reasons for the thickness dependence on the

monomer concentration could be attributed to the steric effect of initiated chains on the diffusion of reaction components. When the surface confined polymer chain length reaches a certain level, monomer diffusion to the reactive site is likely to be reduced, yet this phenomenon can be rendered less significant with higher monomer concentration. Additionally, an approximate first order dependence of the initial rate on both catalyst and monomer concentration has been previously demonstrated for Ni(dppp)Cl_2 polymerization.[170] Taking into account that the amount of surface-immobilized catalyst is constant across all experimental samples, the increase in the monomer concentration may lead to increased rates of polymerization.

4.3.3 Studies of Polymer Thickness versus Time

Polymerizations were performed with 0.09 M monomer concentration samples and analyzed at intervals of 2, 4, 8, 10, 14, 18, and 24 h. The onset of polymer film

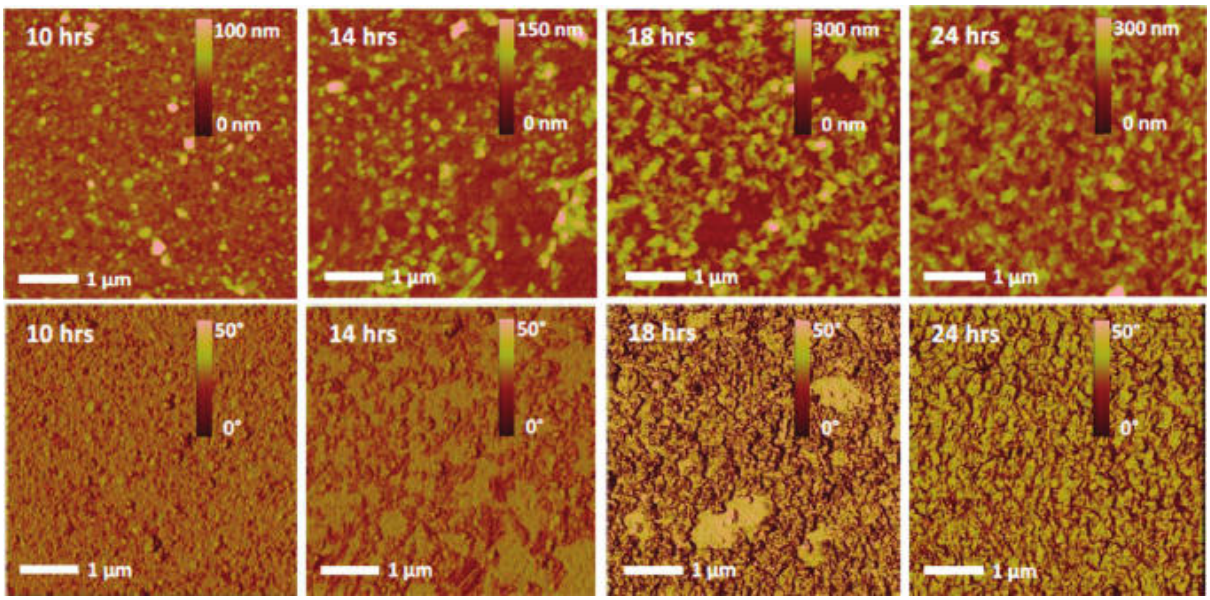

Figure 32: Effect of reaction time on grafted polymer film fabricated from 0.09 M monomer solution.

growth occurred at 10 h and continued on through the 24 h time frame. Both AFM height and phase contrast images (Figure 32) as well as optical observations (Figure 33) show increases in polymer film coverage with increasing time.

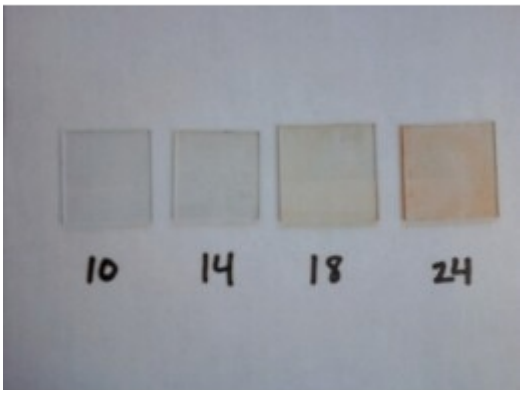

Figure 33: Optical photograph of the films fabricated with 0.09 M monomer concentration during the time studies (numbers below each substrate indicate the number of hours used in the synthesis).

Contrary to the solution KCTP reaction, which typically reaches complete monomer conversion within 2 h, surface initiation was observed to be a slow process. Isolated polymer islands were observed on the sample that was reacted for 10 h, however the average polymer coverage was too low for reproducible profilometry measurements. The average measured thickness values were calculated to be 14, 48, and 80 nm for the samples with polymerization reaction times of 14, 18, and 24 h, respectively. The film thickness increases close to linearly with time (after an induction period), which implies a certain level of polymerization control (Figure 34).

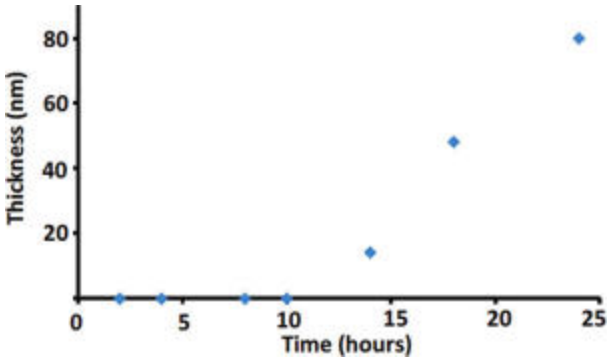

Figure 34: Kinetics of the surface polymer film growth.

As previously mentioned, polymerizations utilizing dppp as the binding ligand on the Ni catalyst involve a rate-determing transmetalation step. In the context of the surface-confined reaction, this translates to the coupling between the surface immobilized Ni(II)dppp-aryl initiator and the Grignard functionalized 3-methylthiophene monomer as being the slowest step. Additionally, the steric crowding near the Ni center has been shown to decelerate the transmetalation step,[171] which would result in the bulky dppp ligand, with two phenyl rings per phosphine, significantly retarding the chain initiation reaction as observed during the time study experiments. Reducing the steric bulk of the supporting ligand is expected to increase the polymerization rate and such studies are currently underway in our laboratory.

4.4 Conclusions

We have utilized SI-KCTP technique to fabricate grafted poly- (3-methylthiophene) films on the surface of indium tin oxide. To our knowledge, these films, ranging from 30 to 265 nm, are the thickest polymer layers grafted from a single monolayer to date. We demonstrated control over prepared film thickness over previous reports with the ability to manipulate the thickness values by varying the monomer

solution concentration. Time studies have shown that reaction kinetics of surface-initiated polymerization are drastically different from solution polymerization with this particular system. The initiation step was observed to proceed slowly, presumably due to the steric effects from the catalyst binding ligand magnified by the surface interface. This surface initiated polymer growth technique, which led to robust polymer-modified electrodes, may ultimately be used with other novel polymer systems of interest to provide control over the interfacial charger transfer processes in organic electronics.

Chapter 5: A One-Pot Controlled CdSe Quantum Dot Synthesis with in-situ π-conjugated Ligand Functionalization

5.1 Introduction

The design and synthesis of functional semiconducting nanocrystals (NCs) have been extensively studied due to the ability to control their photophysical properties and their potential for replacement of traditional materials in many applications including optoelectronics and biological labeling.[172–174] The properties of the nanocrystals, including their spectroscopic, reactivity, stability, and processability properties can be controlled by changing their size, shape, and surface chemistry.[45,175–179] Most synthetic routes for colloidal NCs utilize long chain aliphatic ligands with a coordinating head group that act as a diffusion barrier during growth and remain coordinated to the NCs as a surface monolayer when growth is complete.[180] Efforts to control the surface chemistry of NCs have primarily relied on ligand exchange processes that utilize functional ligands with stronger binding head groups that displace the native ligands,[181,182] but these ligand exchange processes often require a large excess of the desired capping ligands and can take several days to exchange at elevated temperatures for incomplete native ligand displacement.[183,184]

For optoelectronic applications, it is often desirable to utilize capping ligands that facilitate charge transfer across the NC surface while maintaining the miscibility and solution processability of the material. To this end, the direct attachment of molecules containing p-conjugated units is more attractive than using insulating aliphatic ligands. p-conjugated thiols have been shown to effectively quench CdSe

photoluminescence and exhibit shorter photoluminescence lifetimes than that of tri-*n*-octylphosphine oxide (TOPO), a common insulating capping ligand used during the synthesis of CdSe nanoparticles.[185] They have also been shown to act as acceptors for photogenerated holes through the aromatic region with good charge transport properties, and have been used to increase the short-circuit current density relative to TOPO in photovoltaic devices.[185] Some research has been done on the attachment of p-conjugated molecules to CdSe, but they have relied heavily on ligand exchange processes or by the growth or attachment of conjugated polymers on preexisting CdSe nanoparticles, often requiring two or three step processes,[186–194] and it is clear that there is a need for a simpler and more efficient route to CdSe surface functionalization.

In this chapter we report a new method for the attachment of π-conjugated ligands to colloidal CdSe quantum dots that does not rely on a ligand exchange process. This method has the advantages of being a fast and effective one-pot procedure that efficiently attaches ligands with aryl functionality while maintaining the size and shape control of the colloidal CdSe quantum dots. The process is different from typical ligand coordination in that it relies on using a precursor ligand to act as one of the reagents in the reaction. As shown in Scheme 1, in a typical CdSe synthesis, it is thought that the Cd coordinates to the Se on the trialkylphosphine selenide, and then the reaction is driven by the formation of the P=O bond, resulting in the cleavage of the P=Se bond and providing CdSe.[3] We anticipated that the replacement of some of the trialkylphosphine selenide in the reaction with arylthiophosphonates (ArSP) or arylselenophosphonates (ArSeP) would allow for a similar reaction, where the S or Se would coordinate to Cd, and then cleavage of the P-Se bond would result in the

formation of CdSeAr, where the aromatic group would directly attach to the QD surface in a one-pot reaction as outlined in Scheme 4.

Scheme 3: CdSe synthesis reaction (top),[3] and our proposed functionalization reaction (bottom).

Typical CdSe Synthesis

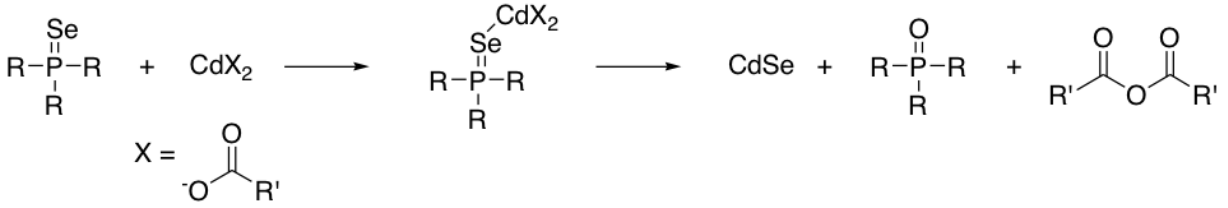

Proposed Reaction

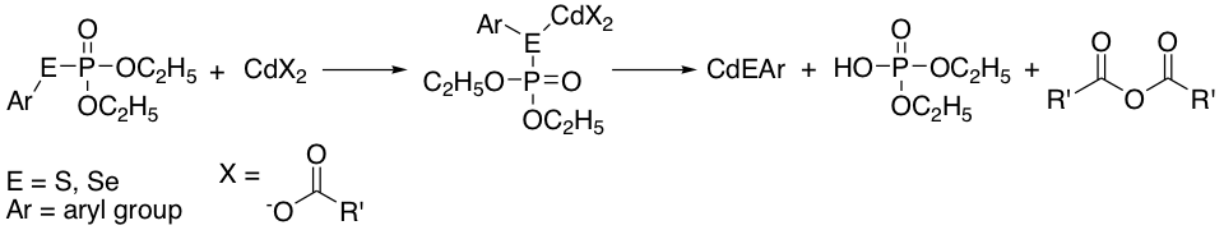

5.2 Experimental

5.2.1 Quantum Dot Synthesis

For all reactions, 1-octadecene (ODE, 90%), CdO, Oleic Acid (90%), Octadecylamine (ODA, 95%), and tri-*n*-octylphosphine oxide (90%, technical grade), and 1-octadecene (ODE, 95%, GC) were purchased from Sigma-Aldrich. Se (99.9%) was purchased from Fluka, and tri-*n*-butylphosphine (TBP) was purchased from Strem. All chemicals and reagents were used as received.

CdSe nanocrystals were synthesized by a modified version of the CdO/amine route synthesis of Yu and Peng.[195] In a typical reaction, 0.0385 g CdO was heated with 0.34 g Oleic Acid in 1g ODE in a N_2 purged three neck flask to 220 °C until the solution

turned clear, indicating the reaction of CdO with Oleic Acid to form Cd-Oleate. The solution would then be allowed to cool to room temperature, at which point the ligands could be added, followed by a N_2 purge. For the growth of CdSe quantum dots with in-situ aryl functionalization, 0.75 g ODA, and 0.406 g ArSP or 0.436 g ArSeP would be added to the reaction mixture. For standard CdSe quantum dots for ligand exchange processes, 0.75 g ODA and 0.25 g TOPO would be added to the reaction mixture at this step. The solutions were then put under vacuum for ~20 minutes at 110 °C until the solution was clear and no longer bubbling. The temperature would then be increased to 260-270 °C, and 1.5 g Se-TBP (from a stock solution of 1.4 g Se, 3.84 g TBP, and 12.33 g ODE that was previously prepared in a glovebox) would be swiftly injected to the reaction mixture and the dots would then be allowed to grow at 260 °C for 8 (for

Scheme 4: Ligand structures.

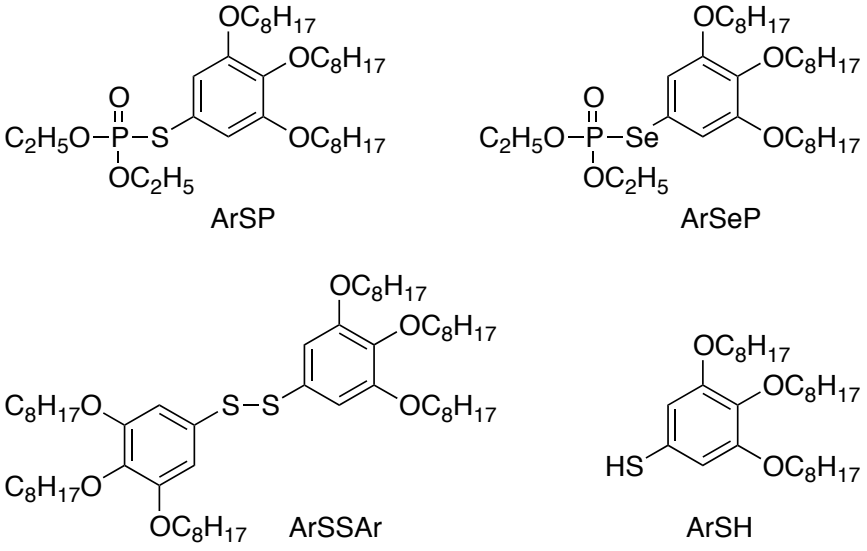

ArSP = O,O'-Diethyl S-[3,4,5-tris(octyloxy)phenyl]phosphorothioate
ArSeP = O,O'-Diethyl Se-[3,4,5-tris(octyloxy)phenyl]phosphoroselenoate
ArSSAr = bis[3,4,5-tris(octyloxy)phenyl]disulfide
ArSH = 3,4,5-trisoctyloxybenzenethiol

pyridine capped dots) or 18 minutes (all other dots), at which point the solution would then be removed from heat and allowed to air cool. All reactions were performed under N_2 on a schlenk line. After cooling to less than 60 °C, the quantum dots were extracted several times in methanol and hexanes. The final hexanes solution contained the desired quantum dots and was centrifuged, redisbursed in hexanes, and dried by rotary evaporation, with samples stored in the dark in air.

For the pyridine ligand exchange process, CdSe quantum dots were redisbursed in 3 mL of pyridine and sonicated for 1 hour in air. The dots were then precipitated and centrifuged in hexanes three times. A modified ligand exchange process with increased temperature was employed for ligand exchange processes[184] with either ArSSAr or ArSH, standard quantum dots were redispursed in chloroform and about 0.4 g of the desired capping ligand were added to the mixture. This mixture was then stirred at 60 °C for 3 days under N_2 atmosphere, with an additional 10 mL of chloroform added each day to compensate for solvent lost over night.

5.2.2 NMR

All NMR samples were taken in $CDCl_3$ on either a Bruker AV-300 or AV-500 spectrometer. All ^1H NMR were referenced to an internal chloroform standard, and all ^{31}P NMR samples were referenced to an external H_3PO_4 standard.

5.2.3 XPS

All XPS experiments were performed in a commercially available multi-chamber ultrahigh vacuum (UHV) system manufactured by SPECS Surface Nano Analysis GmbH (Berlin, Germany), at a base pressure of approximately 2 x 10^{-10} mbar. A homebuilt electrospray injection system is attached to one of the preparation chambers that allows the direct injection of macromolecular material from suspension into vacuum. For more detail on the system see Dam et al.[196]

For sample preparation, highly oriented pyrolytic graphite (HOPG) crystal substrates (Mikromasch, USA, "ZYA" quality) were cleaved to obtain a pristine surface. These crystals were attached to the substrate holder with conductive silver epoxy and a thin metal sheet was attached to the top of the HOPG crystal that was removed after loading the sample, creating a clean graphite surface. The materials to be analyzed were each dispersed in toluene at a concentration of 1 mg/mL and sprayed onto the intake orifice of the electrospray deposition system. After passing through the system, the molecular beam was captured on the substrate forming a thin film. The syringe tip had a 100 μm inner diameter and the spray rate was 4 mL/h. The syringe needle was kept at a potential of -2 kV relative to ground during depositions, and the tip-to-orifice distance was 3 mm. To reduce ambient contamination to negligible levels, during deposition the needle tip was kept in an enclosure that was filled with a slight overpressure of nitrogen gas relative to atmosphere during deposition.

Surface characterization of the substrates and prepared thin films was carried out using standard XPS (Mg *K*α, 1253.6 eV, 20 mA emission current). Analysis of the photoelectrons was performed with a SPECS PHOIBOS 100 hemispherical analyzer. The spectrometer was calibrated to yield the standard Cu $2p_{3/2}$ line at 932.66 eV and the Cu $3p_{3/2}$ line at 75.13 eV. Data evaluation of all photoemission spectra was carried out using Igor Pro software (WaveMetrics, Inc.). For the determination of the maximum core-level peak position a mixed Gaussian-Lorenzian line shape was used.

5.2.4 Photoluminescence

PL spectra for the data presented were measured on a homebuilt optical fiber photoluminescence measurement system with a Stellarnet BLUE Wave portable spectrometer, and Stellarnet LED illumination source, and a Stellarnet Y type '7-around-1' 600 micron fiber optic cable fluorescence probe tip. An excitation wavelength of 390 nm was used with an average of 3 scans and a 10 s detector integration time.

5.2.5 Transmission Electron Microscopy

All transmission electron microscopy (TEM) images were taken on an FEI Tecnai G2 F-20 TEM operating in bright field mode. TEM samples were prepared by dispersing a small amount of dry CdSe quantum dots in hexanes, and dropping onto ultrathin carbon film substrates with holey carbon support films on 400 mesh copper grids (Ted Pella, Inc.).

5.3 Results and Discussion

5.3.1 Ligand Exchange

Ligand exchange reactions were performed with unfunctionalized control CdSe QDs in order to justify the use of a new synthetic methodology for the replacement of native insulating ligands with the thiol (ArSH) and disulfide (ArSSAr) ligands shown in Scheme 5. For the ligand exchange process, we used protocols described in the literature,[184] where standard CdSe QDs were dispersed in $CHCl_3$ and the desired exchange ligand (ArSSAr or ArSH) was added. This mixture was stirred at 60 °C for 3 days under nitrogen and monitored each day by ^1H NMR to determine the progress of the ligand exchange, the results of which can be found in Figure 35. 10 mL $CHCl_3$ was added daily to compensate for the $CHCl_3$ lost overnight. With ArSSAr, no ligand attachment was observed, as has been reported for other disulfide ligands due to the weak affinity of the disulfide bond to the surface of CdSe.[197] For ArSH, the ligand

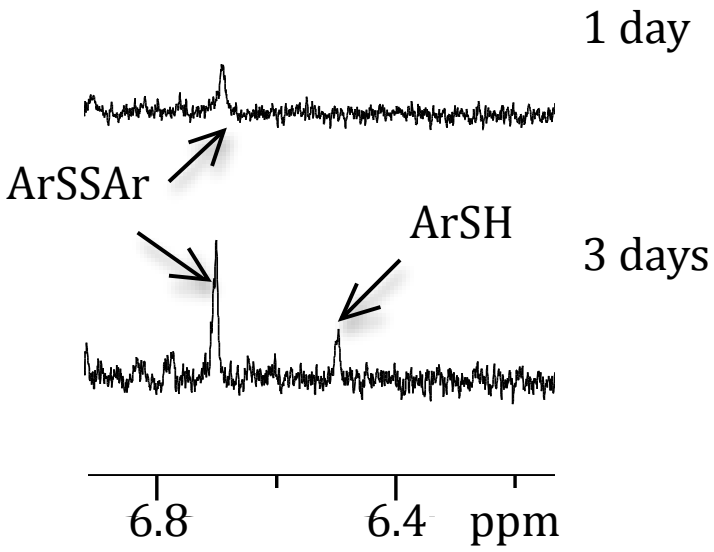

Figure 35: ^1H NMR spectra in the aryl region for ArSH ligand exchange after 1 and 3 days.

exchange process was very slow and generally resulted in the oxidation of ArSH to ArSSAr. After one day, only ArSSAr was observed and no ArSH could be found by NMR. After three days, some ArSH was observed, but three times as much ArSSAr was formed. The limited ligand exchange is consistent with the limited exchange of benzenethiol-type ligands experienced by other groups, and provides an example of the necessity of new ligand attachment methodologies.[185] We speculate that the ligand exchange was relatively unsuccessful where others have been more successful[184] when using benzenethiol derivatives due to the steric bulk of our ligands.

5.3.2 ^{1}H NMR

In order to determine if our ligands were attached to our dots, we first looked at ^{1}H NMR spectra in $CDCl_3$ for the neat ligands and the spectra of the quantum dots synthesized in the presence of these ligands. Figure 36 shows the ^{1}H NMR spectra of neat ArSP (bottom), neat ArSH (middle), and ArSP after attachment on CdSe nanocrystals. The spectrum of neat ArSP shows the protons from the aryl group at 6.75 ppm, the ethoxy protons of the phosphonate as a multiplet at 4.18 ppm, and the α-CH_2 alkoxy protons off the aryl group at 3.94 ppm. The aryl proton signal shifts to 6.49 ppm for the ArSH ligand, with the α-CH_2 aryl alkoxy protons remaining at 3.94 ppm. When CdSe quantum dots are grown in the presence of ArSP, several changes in the spectra are observed. The ethoxy protons disappear from the spectrum while the α-CH_2 aryl alkoxy protons remain at 3.94 ppm, indicating the cleavage of the phosphonate group from the precursor ligand. In addition, the aryl protons at 6.76 ppm disappear, and three new peaks are developed. These have been identified as corresponding to ArSH at

6.49 ppm, ArSSAr at 6.69, and ArS-C_2H_5 at 6.57 ppm (Figure 37). The ArSH is the primary and desired product. The formation of ArSSAr is attributed to the partial oxidation of ArSH due to the instability of the ArSH ligand, as similar benzenethiol containing compounds have been shown to actively photocatalytically oxidize on CdSe nanocrystal surfaces.[198] The ArS-C_2H_5 comes from the partial thermolysis of ArSP as temperatures increase to the Se precursor injection temperature.[199] A full ^{1}H NMR spectrum of ArS-CdSe can be found in Figure 38, showing evidence of residual oleic acid on the QDs, while evidence of other remaining ligands is obscured by the presence of ODE, oleic acid, and ArS- in the alkyl region of the NMR.

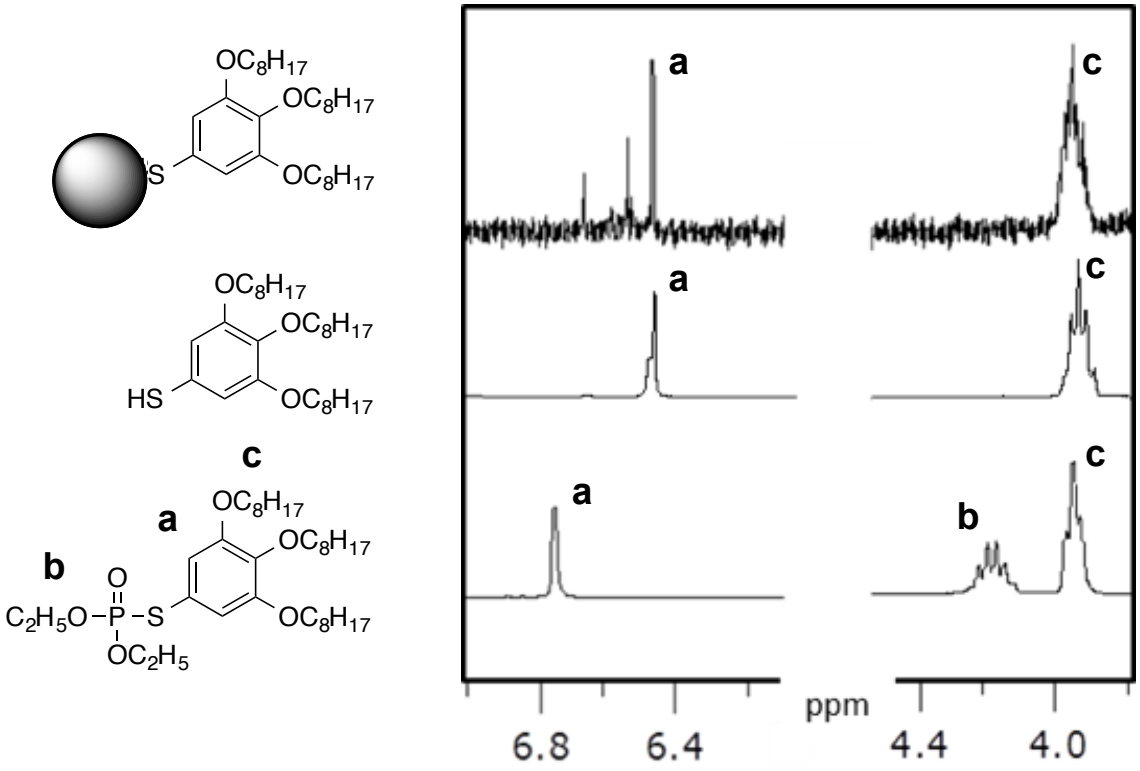

Figure 36: ^{1}H NMR of neat ArSP (bottom), neat ArSH (middle), and ArSP after attachment on CdSe nanocrystals (top).

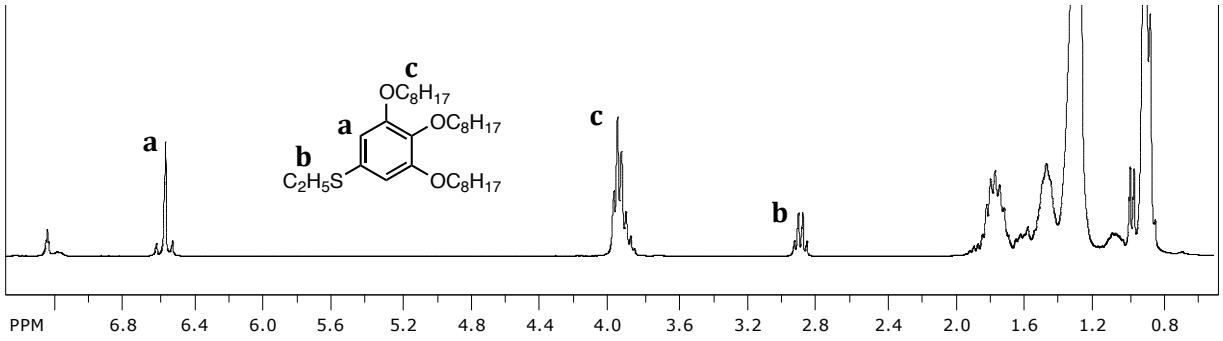

Figure 37: $ArSC_2H_5$ ^1H NMR spectrum.

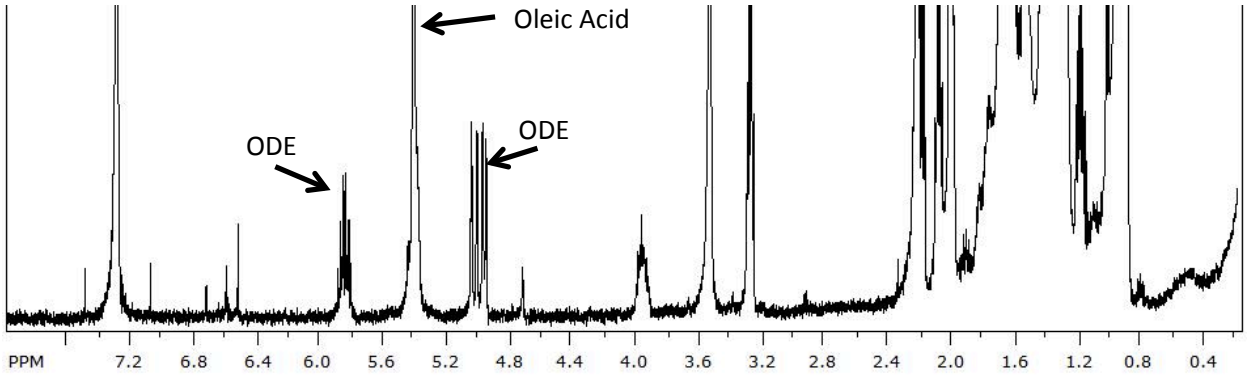

Figure 38: Full ^1H NMR spectrum of ArS-CdSe QDs showing the presence of oleic acid at 5.34 ppm and the presence of residual ODE at 5.81 and 4.86 ppm.

One other possibility for ligand attachment is via the decomposition of our precursor ligands followed by a traditional thiol ligand exchange at the reaction temperature. In order to investigate if this was the case, rather than our hypothesized reaction mechanism, we injected ArSH at the same time as the Se precursor under standard growth conditions. This resulted in the formation of standard quantum dots without any attached thiol, indicating that ligand attachment relies on the coordination of Cd to the ArSP, followed by the cleavage of the P-S bond. A representative ^1H NMR spectrum can be found in Figure 39.

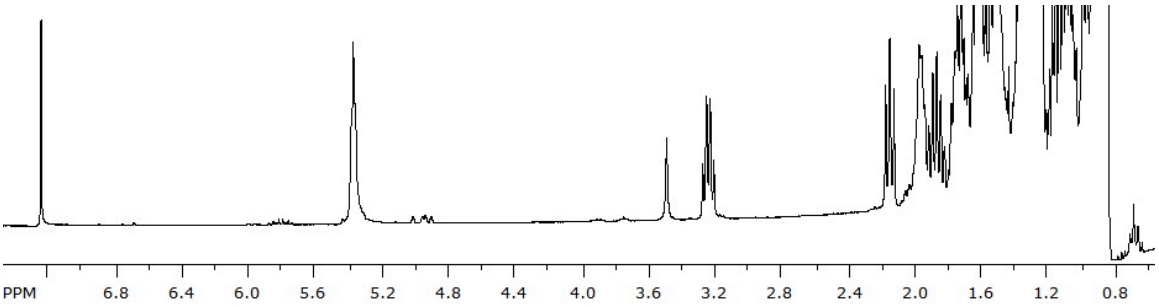

Figure 39: ^{1}H NMR spectrum of CdSe quantum dots grown for 18 min. at 260 C under standard conditions, but with ArSH injected immediately prior to SeTBP. This ^{1}H NMR spectrum shows that there is not a ligand exchange at under standard growth conditions, as there is no signal from the ArSH ligand.

5.3.3 ^{31}P NMR

Additional evidence for the cleavage of the phosphonate group from ArSP during nanocrystal synthesis comes from ^{31}P NMR, as can be seen in Figure 40. As expected, the ^{31}P NMR signal for neat ArSP does not appear in either the methanol or hexanes wash spectra, and because of this we can assume that all of the ArSP precursor ligand added at the beginning of synthesis reacted. The methanol wash contains two peaks that are assigned to unreacted Se precursor, SeTBP, and the sulfur analog, STBP, a reaction byproduct. Although we expect to see the formation of diethoxyphosphonic acid as a by-product of phosphonate cleavage, it is not observed. We expect that this is because diethoxyphosphonic acid has a boiling point (200 °C) below that of the reaction temperature and thus is not observed because it vaporizes during QD synthesis. The hexanes wash containing ArS functionalized quantum dots shows no ^{31}P NMR signal, which shows that the phosphonate did indeed cleave from ArSP, although there is a small chance that this is due to signal broadening due to an inhomogeneous magnetic field on the quantum dot surface.[184]

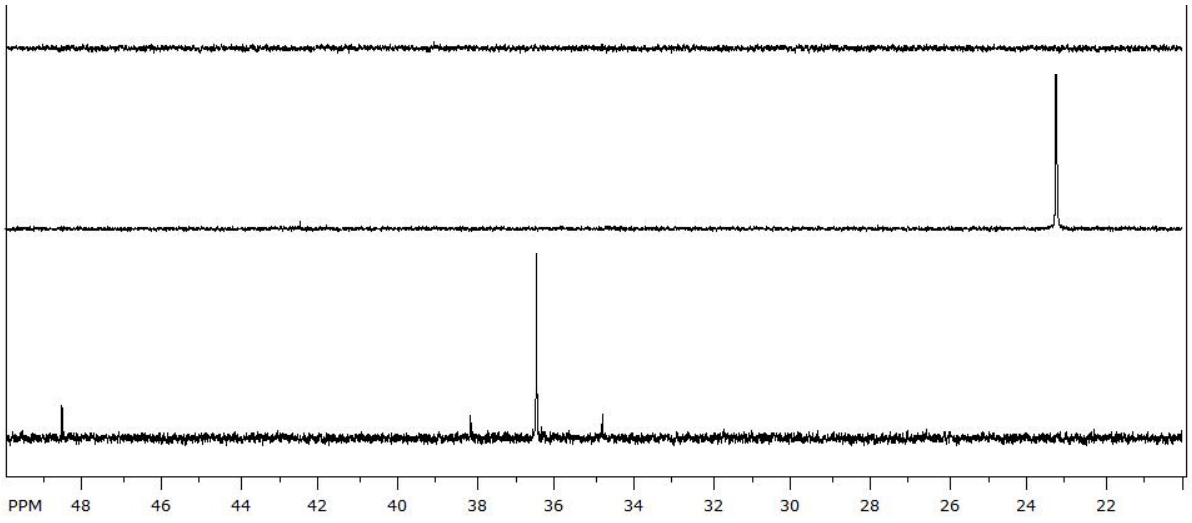

Figure 40: ^{31}P NMR spectra of ArS-CdSe hexanes wash (top, desired product), neat ArSP (middle), and ArS-CdSe methanol wash (bottom, reaction byproducts), with the peak at 36.8 ppm corresponding to residual Se precursor (TBPSe), and the peak at 48.7 corresponding to TBPS, a reaction byproduct.[3]

5.3.4 XPS

As further evidence of actual ligand attachment to CdSe as opposed to some form of decomposition, we looked at X-ray photoelectron spectroscopy (XPS). The bottom XPS spectrum in Figure 41 was measured on neat, unreacted ArSP, while the S2p core level spectrum (center) was measured on ArSH. Due to the low photo-ionization cross section of the S atoms[200] the signal-to-noise ratio is low, resulting in a high residuum peak fitting. Yet, it is apparent that the peak maxima differ only marginally by about 0.3 eV, which is expected considering the similar electronegativity of H and P. Upon formation of the ArS-capped CdSe quantum dots, the S2p spectrum shown at the top of Figure 41 indicates a shift of the core level by ~0.8 eV to higher binding energy relative to the ArSH ligand. Considering an overall resolution of ±0.1 eV for such measurements, this shift is significant and can be explained as the transfer of

electron density from the sulfur atoms to the Lewis acidic Cd metal ions, indicating the bonding of the ligand to the surface of the CdSe.[201,202]

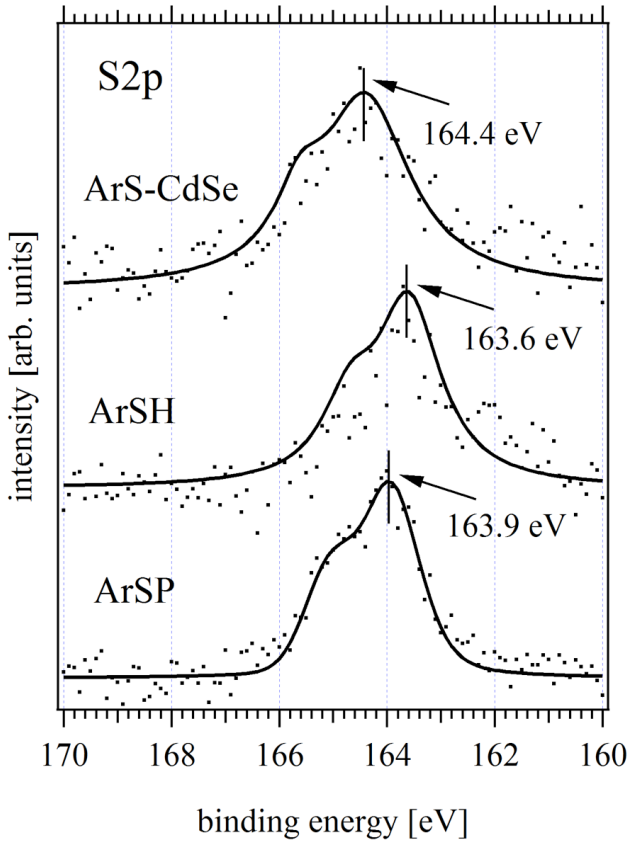

Figure 41: XPS data for S2p binding energies for ArS-CdSe (top), ArSH (center), and ArSP (bottom).

5.3.5 Photoluminescence

As additional support for ligand attachment, we looked at the photoluminescence (PL) spectra of our quantum dots. We observed PL quenching with ligand attachment relative to CdSe quantum dots synthesized without our ligands, as can be seen in Figure 42. Photoluminescence quenching is expected with the attachment of conjugated sulfur containing ligands to the surface of CdSe because the aromatic π-electrons can

act as efficient acceptors for photogenerated holes, thus hindering the radiative recombination process.[185]

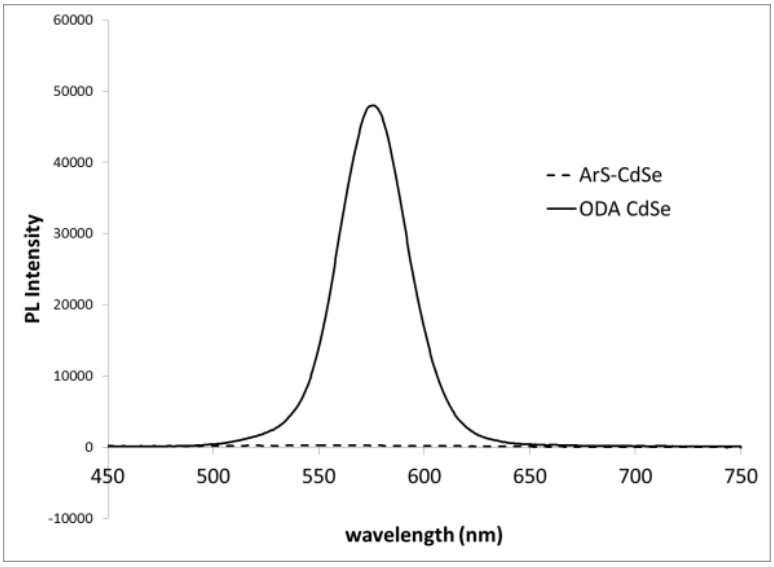

Figure 42: Photoluminescence of CdSe quantum dots with ODA functionalization (solid line) and quenched photoluminescence with aryl functionalization (dashed line).

5.3.6 Attachment of ArSeP

This in-situ ligand attachment process is not limited to ligands containing a sulfur-phosphonate bond. We found similar NMR and XPS results when S was replaced by Se and ArSeP ligands were attached to CdSe quantum dots in an analogous fashion, as can be seen in the comparative ^{1}H NMR spectra of Figure 43, and the XPS spectra of Figure 44. The ^{1}H NMR spectra show neat ArSeP on the bottom and the resulting spectrum after attachment of ArSeP to CdSe on the top. The disappearance of the α-CH_2 ethoxy protons of the phosphonate group at 4.18 ppm and the development of a series of reaction products as observed in the aryl region with attachment of ArSeP to CdSe indicate a similar response to the functionalization of CdSe with ArSP. The Se3d XPS spectra show that the Se energy levels in CdSe do not change with functionalization, but that there exists a change in Se binding energy from 55.9 eV for

ArSeP to a higher binding energy of 56.4 eV with attachment of this ligand to CdSe. Unfortunately, the selenol form, ArSeH, of the ArSeP precursor ligand is not stable, and therefore was unavailable for direct determination of the binding energy shift of these materials. The instability of ArSeH provides another justification for the necessity of our functionalization scheme, as selenol functionalization of CdSe would not be possible without this method.

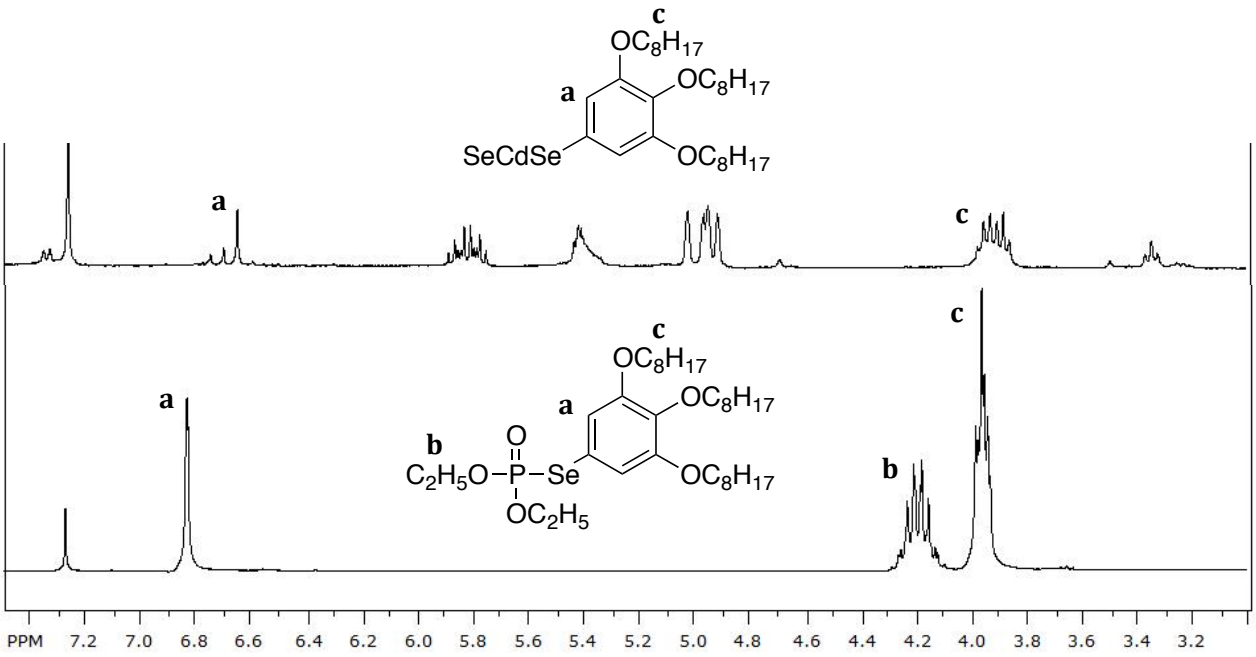

Figure 43: ^{1}H NMR of neat ArSeP (bottom), and ArSeP after attachment to CdSe quantum dots (top).

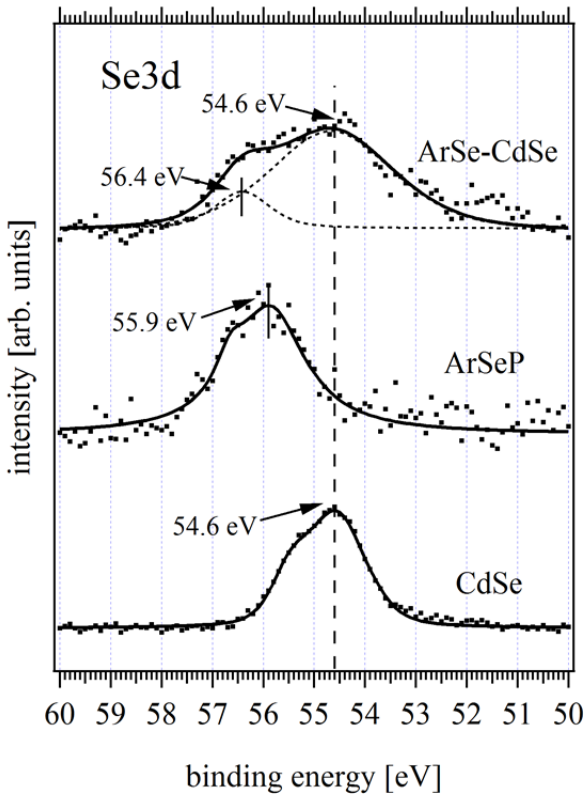

Figure 44: Se3d binding energies for ArSe-CdSe (top), neat ArSeP (middle), and bare CdSe (bottom).

5.3.7 Transmission Electron Microscopy

However, with the attachment of the ArSeP ligands, we found that we were not able to maintain size and shape control as we were previously able to do with attachment of the ArSP ligands under the same conditions, as can be seen in Figure 45. This loss of size and shape control is attributed to the greater reactivity of the Se-containing ligands, as others have previously shown a lack of control with highly reactive ligands.[203]

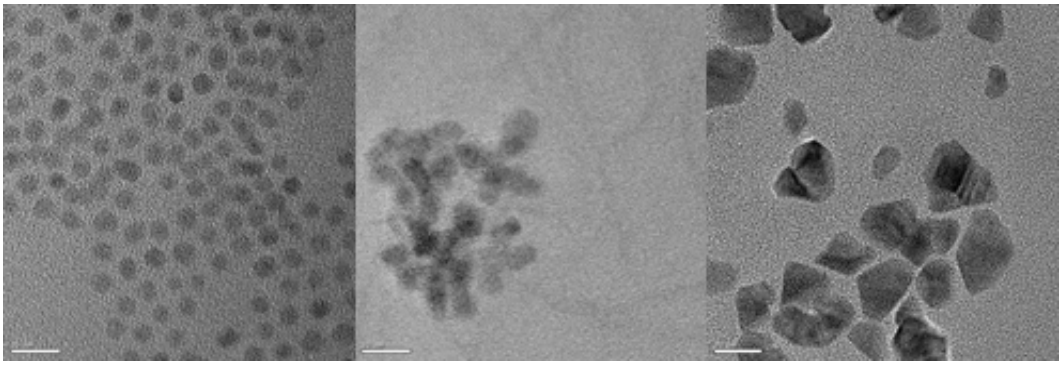

Figure 45: TEM images of ODA capped CdSe (left), ArS-CdSe (middle), and ArSe-CdSe (right). The scale bars on the left and middle images are 10 nm; the scale bar on the right image is 20 nm.

5.4 Conclusions

In Summary, we report here a novel procedure for the attachment of π-conjugated ligands that does not rely on a ligand exchange process. The process developed relies on the cleavage of a phosphonate moiety on the desired ligand for direct attachment onto the quantum dot. We showed that this method is applicable for both sulfur and selenium containing ligands where established ligand exchange processes with similar traditional ligands are difficult. The use of this method for the attachment of semiconducting polymers to CdSe QDs for use in photovoltaic cells is discussed in the following chapter.

Chapter 6: CdSe/P3HT Hybrid Material Synthesis and Photophysical Properties

6.1 Motivation/Introduction

Hybrid organic-inorganic materials are currently attracting much attention for use in light-weight and flexible optoelectronic devices and biological labeling because of the possibility of combining the desirable characteristics of each component. Devices consisting of hybrid materials have been proposed to compensate for the short lifetimes, low charge carrier mobilities, and short exciton diffusion lengths associated with the organic material while maintaining their solution processability. Hybrid devices with bulk heterojunction type architectures have been limited to power conversion efficiencies of 5.5%[204] due to poor interfacial and morphological control, and there is a clear need to increase the performance of hybrid devices for market competitiveness. We aim to enhance the efficiency of hybrid photovoltaics using polymer/nanocrystal hybrid materials fabricated according to the synthetic methodology discussed in chapter 5, and generate a deeper understanding of their exciton dissociation and charge transport processes that is a necessity for the rational design of future materials.

Some research has been done on the attachment of π-conjugated molecules to II-VI nanocrystals, such as CdSe, but they have relied heavily on ligand exchange processes or by the growth or attachment of conjugated polymers on preexisting nanoparticles, often requiring two or three step processes,[186,188–194,205] and it is clear that there is a need for a simpler and more efficient route to nanocrystal surface functionalization. Using our unique methodology we aim to facilitate charge transfer

between donor and acceptor materials, and reduce the complexity of processing for the functionalization of semiconducting quantum dots while simultaneously decreasing the amount of material required for functionalization and thereby cutting the overall production cost.

An understanding of the exciton dissociation dynamics in hybrid materials is essential for their use as electronic materials in photovoltaics. While much work has been done on examining the photoluminescence (PL) properties of CdSe quantum dots with semiconducting polymers to infer knowledge of charge transfer, static or dynamic PL quenching does not provide a full description of the quenching mechanism.[206,207] Transient absorption spectroscopy (TAS) is a technique that can be used to determine if the quenching of PL is a result of charge transfer or if it is instead a result of non-radiative decay processes. Additionally, if the ligands attached to a quantum dot participate in charge transfer, TAS is useful for quantifying the average number of ligands attached to the quantum dots.

Transient absorption spectroscopy (TAS) allows investigation of energy transfer processes on the fs time scale. In a TAS experiment, a pump pulse is absorbed by the sample of interest, promoting a small fraction of molecules to the excited state. A weak probe pulse with delay time τ relative to the pump pulse is then sent through the incident sample. The transmitted probe pulse is then sent through a diffraction grating where it is spread out, before being recorded on a diode array. A differential absorption spectrum can be calculated from the transmitted probe pulse relative to the ground state absorption spectrum. Performing this process over a variety of delay times between the pump and probe results in a collection of spectra containing information on the dynamic

excited state processes occurring in the system under investigation.

In this chapter, we discuss the synthesis of hybrid P3HT/CdSe materials and their photophysical properties, with particular emphasis on the TAS of these materials at ultrafast time scales.

6.2 Experimental

6.2.1 Polymer Ligand Synthesis

All reactions were carried out under nitrogen atmosphere using standard Schlenk techniques. All reagents were purchased from commercial sources and used without purification, unless otherwise indicated. The monomer 2-bromo-5-iodo-3-hexylthiophene and the catalyst 2-tolylNi(PPh_3)$_2$Br were synthesized according to literature procedures.[161] ^{1}H, ^{13}C, and ^{31}P NMR spectra were recorded on a Bruker AV-300 NMR spectrometer using TMS (for polymer ligand synthesis) or $CHCl_3$ (for quantum dot synthesis) as an internal standard. For ^{31}P NMR, 85% H_3PO_4 was used as an external standard. MALDI-TOF MS spectra were recorded on a Bruker Autoflex II spectrometer in reflectron mode, using terthiophene as the sample matrix. MALDI-TOF MS samples were prepared by dissolving 0.5 mg of sample in 100 µL of matrix solution in chloroform and approximately 2 µL of this solution was deposited on the plate.

Polymer precursor ligands were synthesized according to a modified procedure of the α2-tol/ωSH P3HT (P3HT-SH) synthesis previously reported by Okamoto and Luscombe,[208] with an additional step that resulted in the formation of α2-tol/ωS-PO(OEt)$_2$ P3HT (SP-P3HT), as outlined in Scheme 6. Briefly, externally initiated rr-

P3HT was synthesized according to previously reported procedures,[161] where 2-bromo-5-iodo-3-hexylthiophene (5 mmol, 1.87 g), dry LiCl (10 mmol, 0.42 g), and THF (40 mL) was added to a schlenk flask. 2 M *i*-PrMgCl was added dropwise at 0 °C for 10 min, followed by allowing the mixture to stir at room temperature for 30 min. 2-tolylNi(PPh_3)$_2$Br (0.25 mmol, 0.19 g) was exchanged with dppp (0.5 mmol, 0.21 g) in 10 mL THF for 1 h at room temperature to form the polymerization catalyst. This catalyst was then injected to the monomer mixture at once, and the resulting reaction mixture was allowed to stir at room temperature for 1 h. The polymerization was quenched by injecting it into a mixture of sulfur powder (S_8, 50 mmol, 1.6 g) and 1,8-diazabicyclo[5,4,0]undec-7-ene (DBU, 6 mmol, 0.9 mL), and allowing to stir under a nitrogen atmosphere at room temperature for 30 min, followed by the addition of 5 M HCl (~50 mL), and resulting in P3HT-SH. This polymer was extracted in brine and $CHCl_3$, then dried with Na_2SO_4, filtered, and dried under vacuum on a rotary evaporator. For synthesis of SP-P3HT, P3HT-SH was dissolved in $CHCl_3$ and a large excess of both I_2 and $HPO(OC_2H_5)_2$ were added at room temperature with stirring. Triethylamine (TEA) was then added fast dropwise to this mixture until there was no longer any visible vapor being emitted from the solution, at which point an additional 10-15 mL of TEA was then added until boiling; this reaction was allowed to stir in air for 30 min. The reaction was then quenched by the addition of an excess of aq. Na_2SO_3 with stirring, followed by extraction in brine and $CHCl_3$ and drying under vacuum on a rotary evaporator.

Scheme 5: Synthetic scheme for a P3HT containing polymer precursor ligand.

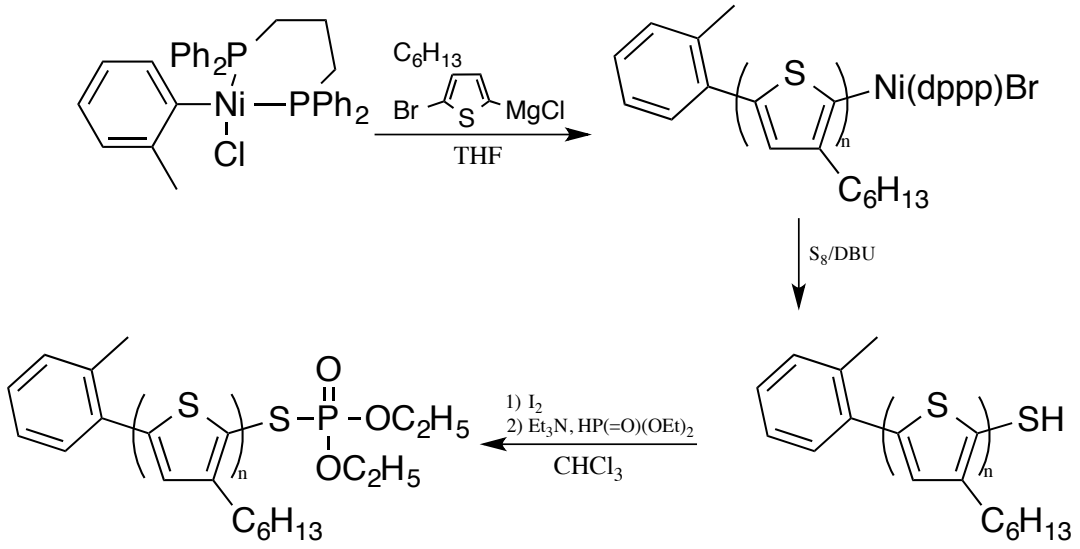

6.2.2 CdSe quantum dot and hybrid material synthesis

For all reactions, 1-octadecene (ODE, 90%), CdO, Oleic Acid (90%), Octadecylamine (ODA, 95%), and tri-n-octylphosphine oxide (TOPO, 90%, technical grade), and 1-octadecene (ODE, 95%, GC) were purchased from Sigma-Aldrich. Se (99.9%) was purchased from Fluka, and tri-n-butylphosphine (TBP) was purchased from Strem. All chemicals and reagents were used as received.

The details of the CdSe and hybrid materials synthesis, including a proposed reaction mechanism, were detailed for hybrid materials made with aryl containing small molecules in the previous chapter. Hybrid materials consisting of CdSe and P3HT were synthesized under similar conditions. Briefly, CdSe nanocrystals were synthesized according to a modified version of the CdO/amine route synthesis of Yu and Peng.[195] In a typical reaction, 0.0385 g CdO was heated with 0.34 g Oleic Acid in 1 g 95% ODE in a N_2 purged three neck flask to 220 °C until the solution turned clear, indicating the

formation of Cd-Oleate. The solution was then allowed to cool to room temperature and 0.75 g ODA was be added, followed by heating to 110 °C under vacuum for at least 30 minutes and until the solution was no longer bubbling. The temperature was then increased to 280 °C, and 1.5 g Se-TBP (from a stock solution of 1.4 g Se, 3.84 g TBP, and 12.33 g 90% ODE that was previously prepared in a glovebox) was swiftly injected into the reaction mixture and the quantum dots allowed to grow at 260 °C for two minutes before adding various concentrations of SP-P3HT (0.002, 0.004, 0.006, 0.008, 0.010, and 0.012 mmol). Growth was then allowed to continue at 260 °C for an additional 16 minutes (18 minute growth total) before removing from heat and allowing to cool to room temperature. The hybrid quantum dots were then extracted two to three times in methanol and hexanes. The final hexanes solution containing the desired hybrid materials was then dried by rotary evaporation. The dry hybrid materials were then washed twice with acetone to remove any remaining impurities, followed by drying again by rotary evaporation, with samples stored in the dark in a glovebox with N_2 atmosphere.

6.2.3 Spectroscopy

Ultraviolet-visible (UV-Vis) spectra were collected on an Agilent 8453 UV-Vis spectrophotometer. Steady state photoluminescence (PL) measurements were performed on a Shimadzu RF-5301 PC spectrofluorophotometer. Time-Correlated Single Photon Counting (TCSPC) measurements were carried out in a Horiba Fluorolog TCSPC coupled to a Horiba iHR320 grating monochromator (1200 g/mm). The excitation source was a 452 nm LED Horiba DD-450L Delta Diode picosecond laser. Spectra were collected on a Horiba Jobin Yvon TBX-04 photon detection system.

Quartz cuvettes were used for all of the liquid samples when testing the UV-Vis, PL, and TCSPC.

6.2.4 TA Spectroscopy

Transient absorption (TA) spectroscopy was performed with a 3-kHz train of 100 fs pulses (1.3 nJ/pulse, λ_0 = 800 nm) generated in a Ti:Sapphire amplifier system (Spectra-Physics, Spitfire-Pro) pumped by a 20-W DPSS Q-switched Nd:YLF laser (Spectra-Physics, empower) and seeded by a mode-locked oscillator (Spectra-Physics, Maitai). A portion of the amplifier output was used to pump a TOPAS optical parametric amplifier to enable tuning of the excitation pulses. Another portion of the amplifier output was used to generate a supercontinuum on a 3 mm thick CaF_2 plate that was moved on an automated translation stage to prevent damage. The probe beam was delayed relative to the excitation beam via a computer controlled Newport mechanical delay stage. The pump beam and the probe beam were focused to overlap nearly colinnearly in the sample, with the polarization set to the magic angle of 54.7° to avoid orientational dynamics. The fwhm diameters in the plane of the samples of the pump and probe beams were 400 and 250 μm, respectively. Any residual excitation beam remaining after having passed through the sample was blocked. The probe beam was directed through a home-built prism spectrograph and spectrally dispersed onto two 256 pixel photodiode arrays that are integrated in a camera from Entwicklungsbuero Stesing that is synchronized with the laser and read out shot-to-shot. The excitation beam was chopped at 1.5 kHz, such that every other probe pulse could be compared in order to obtain a differential transmission due to excitation. The differential transmission spectra were obtained via this method for each pixel, and the temporal dynamics were collected

by obtaining spectra over a range of variable probe delay times (typically ~150 points distributed from -10 to 2000 ps). Approximately 1000 laser shots were averaged for each data point and the entire time range was swept 5-10 times. There is a chirp of ~1.5 ps across the 500-800 nm probe spectrum that is a result of group velocity dispersion. This chirp is corrected for in data post processing by introducing a wavelength-dependent temporal offset. After making this correction and performing a negative-time background subtraction, the instrument limited time resolution was determined to be approximately 120 fs, as determined by the resulting signal rise time. For long time TA measurements on the ns timescale and greater, the 2nd or 3rd harmonic output of a Q-switched laser (532 nm) was used as the excitation source. This output was synchronized with the same broadband probe used for short time TA using a Stanford Research Systems DG535 electronic delay generator.

6.3 Results and Discussion

6.3.1 Polymer precursor synthesis

Synthesis of the polymer precursor ligand began with the synthesis of rr-P3HT according to literature procedures following KCTP, where Ni(dppp)Cl_2 catalyst was added to the thiophene monomer.[161,208] The polymerization was quenched with S_8/DBU at room temperature (with a small amount quenched with HCl at room temperature to verify the polymer end group) to provide thiol terminated P3HT. Figure 46 shows ^{1}H NMR spectra of proton terminated (HCl quenched) P3HT and thiol terminated (S_8/DBU quenched) P3HT. The presence of terminating protons in the acid quenched sample can be observed at 2.5 ppm. All signal from these terminating protons are observed to disappear for the polymer quenched with S_8/DBU. We do not observe the thiol

terminating proton for this polymer, which we hypothesize is a result of its upfield shift, resulting in this signal being hidden behind the α-CH_2 protons of the alkyl chain at 2.6 ppm. After verifying the formation of P3HT-SH, we performed a sulfur-phosphorous coupling reaction between P3HT-SH and diethyl phosphite[209] to form the final precursor polymer, SP-P3HT, the progress of which was also monitored by NMR, and the results of which can be found in Figure 46. We can see that the phosphonate group was successfully added to the thiol by the development of a new signal at 4.5 ppm corresponding to the α-CH_2 protons of the ethoxy groups on the phosphonate moiety.

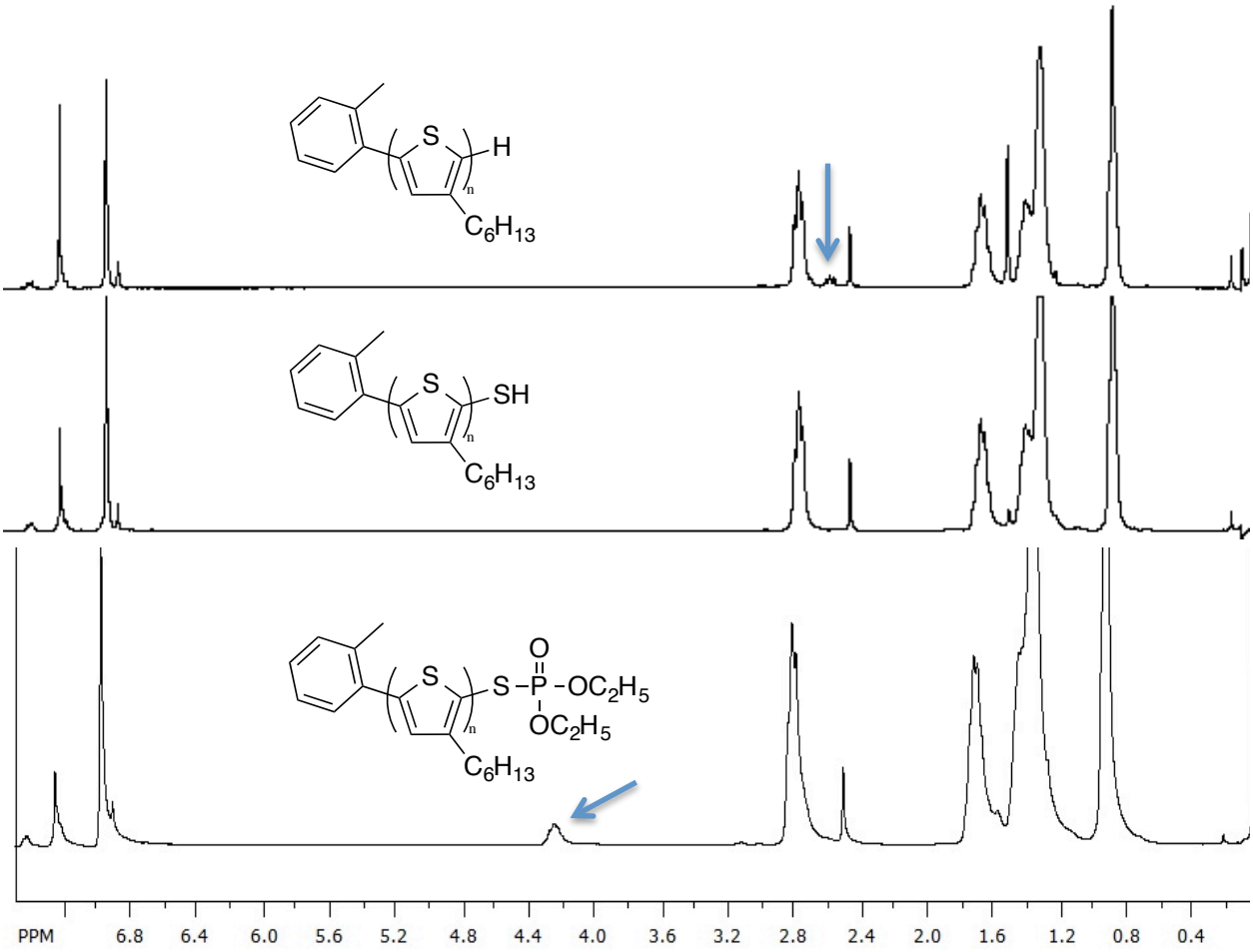

Figure 46: ^{1}H NMR of (top) proton terminated P3HT, (middle) P3HT-SH, and (bottom) SP-P3HT.

6.3.2 Hybrid material synthesis results

Synthesis of CdSe/P3HT hybrid materials followed the same reaction scheme outlined in the previous chapter. The reaction was similarly monitored by ^{1}H NMR, and an example of these results can be found in Figure 47. Here we can observe evidence of the cleavage of the phosphonate group from the polymer precursor material by the disappearance of the α-CH_2 protons on the ethoxy group at 4.2 ppm. There exists evidence of only a small amount of the thermolysis product, which we can determine by the ratio of the integrated tolyl peak at 2.4 ppm to the thermolysis multiplet at 3.2 ppm. We believe that the thiol proton is again hidden behind the signal from the α-CH_2 protons of the hexyl chain on the P3HT backbone around 2.8 ppm. Overall, we made a series of six hybrids with different concentrations of P3HT precursor ligand added during synthesis. These are denoted hybrid 002, 004, 006, 008, 010, and 012, in order of increasing P3HT concentration added during synthesis.

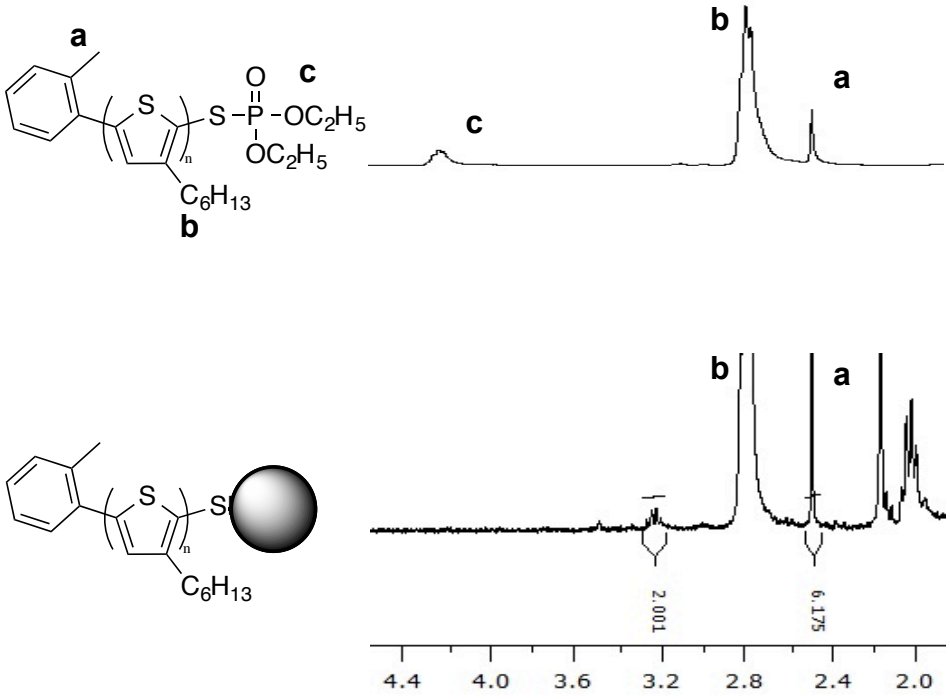

Figure 47: ^{1}H NMR of (top) SP-P3HT and (bottom) a CdSe-P3HT hybrid material.

6.3.3 UV-Vis Spectroscopy

Neat CdSe, neat P3HT-SH, a 10:1 blend of CdSe:P3HT-SH and the series of CdSe-P3HT hybrid materials were characterized by UV-Vis absorption spectroscopy at similar concentrations by weight (0.01 mg/mL), as shown in Figure 48. P3HT-SH has a broad absorbance with a maximum absorbance at 441 nm, which is typical for P3HT in solution,[210] indicating that the thiol termination does not appreciably effect the absorption properties of the polymer. The absorption of neat CdSe quantum dots shows a sharp onset at about 590 nm and a well defined exciton peak, as can be clearly seen in the inset of Figure 48, indicating a good size distribution of the quantum dots.[211] A 10:1 blend of CdSe:P3HT-SH shows a combination of the two individual spectra, where contributions from each component overlap, as we would expect with the two materials

not interacting in dilute solution. With the formation of hybrid materials, we can see some initial similarities with the blend spectrum, where contributions from both components can be identified, but there are also some differences in the hybrid UV-Vis absorption spectra. The most obvious change lies in the reduction of the P3HT contribution with decreasing precursor polymer added during synthesis. This trend roughly follows what we would predict for blend scenarios with decreasing P3HT concentration in the blend, and indeed, a 10:1 CdSe:P3HT-SH blend was chosen in order to compare a blend to hybrid 004 due to their similar absorbance spectra at the same concentration by weight. One thing that is unique in the absorbance spectra of the hybrids is that they show an obvious extension in the onset of absorbance into the red with hybridization, as can be clearly seen in the inset of Figure 48. Initial considerations would indicate that this implies a broad size distribution in the CdSe quantum dots, and that we are unable to control the growth kinetics of the CdSe with the addition of SP-P3HT as a reaction monomer, with another option being that there is something interesting electronically happening with hybridization.

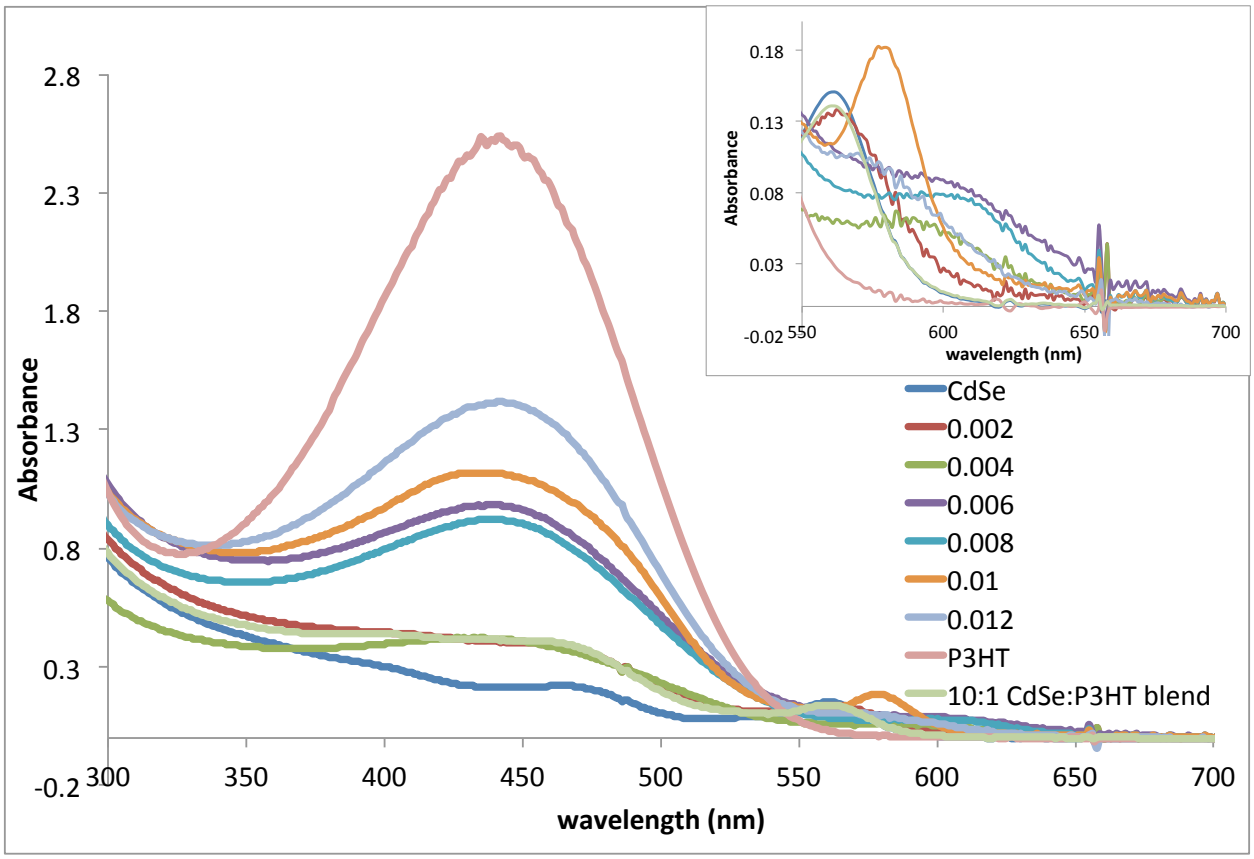

Figure 48: UV-Vis spectra of neat CdSe, neat P3HT-SH, a 10:1 CdSe:P3HT-SH blend, and hybrid materials made with 0.002, 0.004, 0.006, 0.008, 0.010, and 0.012 mmol SP-P3HT precursor ligand added during synthesis, hereon referred to as Hybrid 002, 004, 006, 008, 010, and 012, respectively.

6.3.4 Transmission Electron Microscopy

To establish if we actually had a larger size or broader size distributions, we determined the size of each hybrid material via TEM, as shown in Figure 49 a-f. The average size of each hybrid material was 3.4±0.3 nm, 3.9±0.2 nm, 4.1±0.4 nm, 4.2±0.3 nm, 3.51±0.08 nm, and 3.8±0.2 nm for hybrid 002, 004, 006, 008, 010, and 012, respectively. Due to the relatively small standard deviation in quantum dot size, it is clear that we are able to maintain more controlled growth kinetics with the addition of SP-P3HT as a reaction monomer than the extension of the absorption into the red would imply. We can compare the sizes determined by TEM and compare them to

empirical calculations used to determine the size of CdSe based on the absorption onset. In the Yu approximation,[212] a variety of CdSe nanocrystal sizes were determined by TEM and plotted vs their onset of absorption. These points were then fit with a fourth order polynomial to provide the empirical fitting function in Equation 11

$$D = (1.6122\times10^{-9})\lambda^4 - (2.6575\times10^{-6})\lambda^3 + (1.6242\times10^{-3})\lambda^2 - (0.4277)\lambda + 41.57 \quad (11)$$

where D is the calculated diameter based on the absorption onset, λ. We found that size estimations for our hybrid materials grossly overestimated the actual sizes of these materials as determined by TEM, the values of which are presented in Table 3. From this study we found that size characterization of our hybrid materials must be determined by visualization of the particles through a technique such as TEM, rather than size determination via UV-Vis, as is commonly used for standard quantum dots.[211]

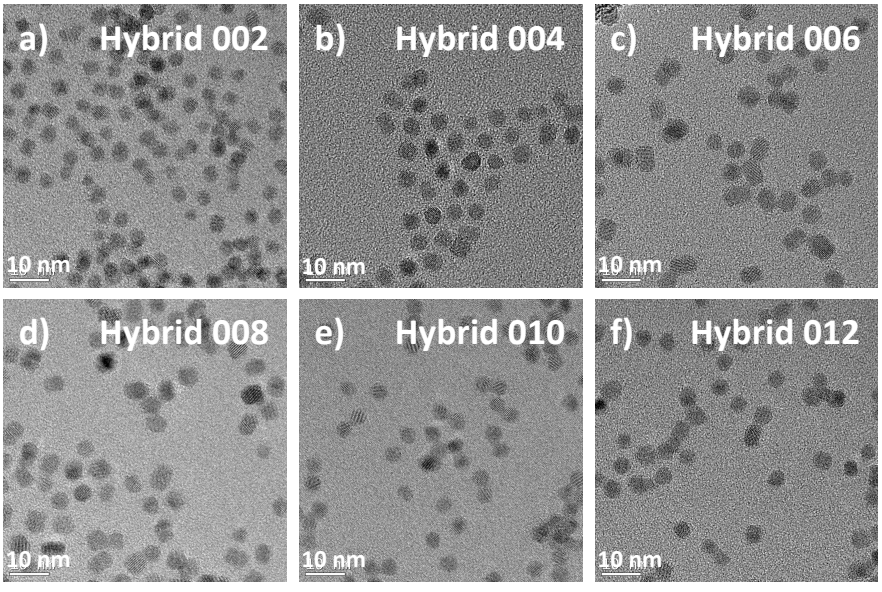

Figure 49: Representative TEM images for a) Hybrid 002, b) Hybrid 004, c) Hybrid 006, d) Hybrid 008, e) Hybrid 010, and f) Hybrid 012, with each having a 10 nm scale bar.

Table 3: UV-Vis absorption onsets, Yu approximation sizes, and size determined by TEM for all hybrid nanoparticle samples.

	hybrid 002	hybrid 004	hybrid 006	hybrid 008	hybrid 010	hybrid 012
Absorption onset (nm)	600	650	670	655	605	635
Yu approximation (nm)	4.6	7.8	9.7	8.2	4.8	6.6
Size by TEM (nm)	3.4	3.9	4.1	4.2	3.5	3.8

6.3.5 Photoluminscence

Continuing with steady state optical spectroscopy, we examined the photoluminescence (PL) properties of each material. Unfortunately, P3HT and CdSe show almost the exact same PL emission wavelength, as shown in Figure 50, with P3HT emitting at 568 nm and CdSe emitting at 570 nm. The hybrid materials all have PL emissions between 569-571 nm, and as a result, it is clear that we are unable to determine which species is responsible for the observed photoluminescence. However, while we were expecting to see drastic quenching of the P3HT photoluminescence with the hybrid materials, this phenomenon is not observed in the PL spectra when normalized to the absorbance at the excitation wavelength. We examined excitation at wavelengths of both 440 nm and 540 nm, as can be seen in Figure 50 a) and b), respectively, where the 440 nm excitation was attempting to primarily excite P3HT and the 540 nm excitation attempting to primarily exciting CdSe. Neither excitation wavelength shows quenching of the P3HT PL. Instead, we observe the trend of the PL increasing with increasing concentration of P3HT incorporated into the hybrid materials, and even surpassing the PL of neat P3HT with some of the hybrids that contain greater amounts of P3HT. Due to the spectral overlap between the CdSe and P3HT PL, it is unclear whether this is due to a combination of free CdSe and P3HT species in solution, a result of charge transfer from the CdSe to P3HT, or another phenomenon entirely,

and it is clear that further optical experiments detailing the time resolved evolution of the photoluminescent species needed to be performed.

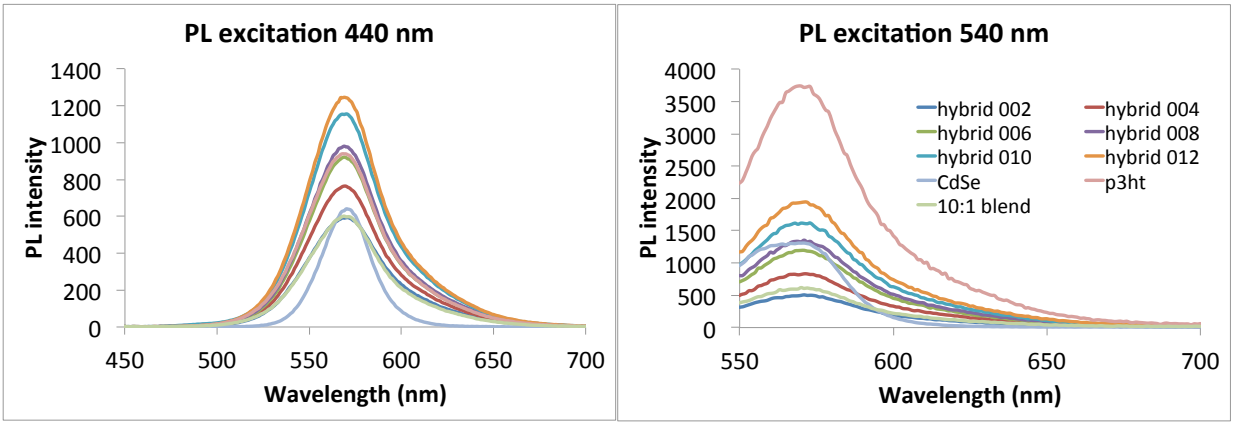

Figure 50: Photoluminescence spectra for neat CdSe, neat P3HT-SH, a 10:1 CdSe:P3HT-SH blend, and all hybrid materials with 440 nm excitation (left) and 540 nm excitation (right).

6.3.6 Time Correlated Single Photon Counting

We investigated the time-resolved photoluminescence spectra of each species with the time-correlated single photon counting (TCSPC) technique, the results of which are shown in Table 4 and Figure 51. TCSPC is a form of time resolved fluorescence spectroscopy that relies on the detection of single photons emitted from chromophores that are excited by a pulsed light source with known wavelength and repetition rate. The output is a waveform generated based on a series of randomly distributed photons that are emitted by these chromophores and is representative of its fluorescence decay in time. TCSPC is a form of ultrafast spectroscopy that allows fluorescence lifetime measurements on the picosecond time scale. From Figure 51, we can see that all of the hybrid materials appear to behave similarly to that of P3HT. CdSe shows a similar fast component response to P3HT initially, but has longer lived components that we hypothesize are due to surface trap states, or deep trap states within the dots. It is

interesting that the 10:1 blend of CdSe:P3HT-SH does not show any contributions from the long lived CdSe photoluminescence species, particularly at such high CdSe loading. As these are solution phase experiments, we would not expect the two materials to interact at such low concentrations. This implies that any free P3HT in solution will dominate the PL response. The PL lifetime can be calculated as the inverse of the slope in the linear region of the TCSPC plot. Table 4 shows that the PL lifetimes for each material have a fast component that has a lifetime of approximately 500 ps. The resolution of the TCSPC instrument is approximately 100 ps as determined via the scattering of incident light with a 30 wt% silica slurry in water. This means that any quenching of photoluminescence faster than 100 ps will be unresolvable, and it is quite possible that the hybrid materials exhibit a much faster PL quenching lifetime than that of either neat CdSe or P3HT, and are therefore unresolvable with TCSPC. This also means that the instrument response function dictates that no significant difference can be ascertained from the lifetimes of each material examined. In addition, neither static nor dynamic photoluminescence measurements can provide a full description of the quenching mechanism. Transient absorption spectroscopy is a power full tool that can be used to determine if any PL quenching is a result of charge transfer or if it is instead a result of non-radiative decay processes.

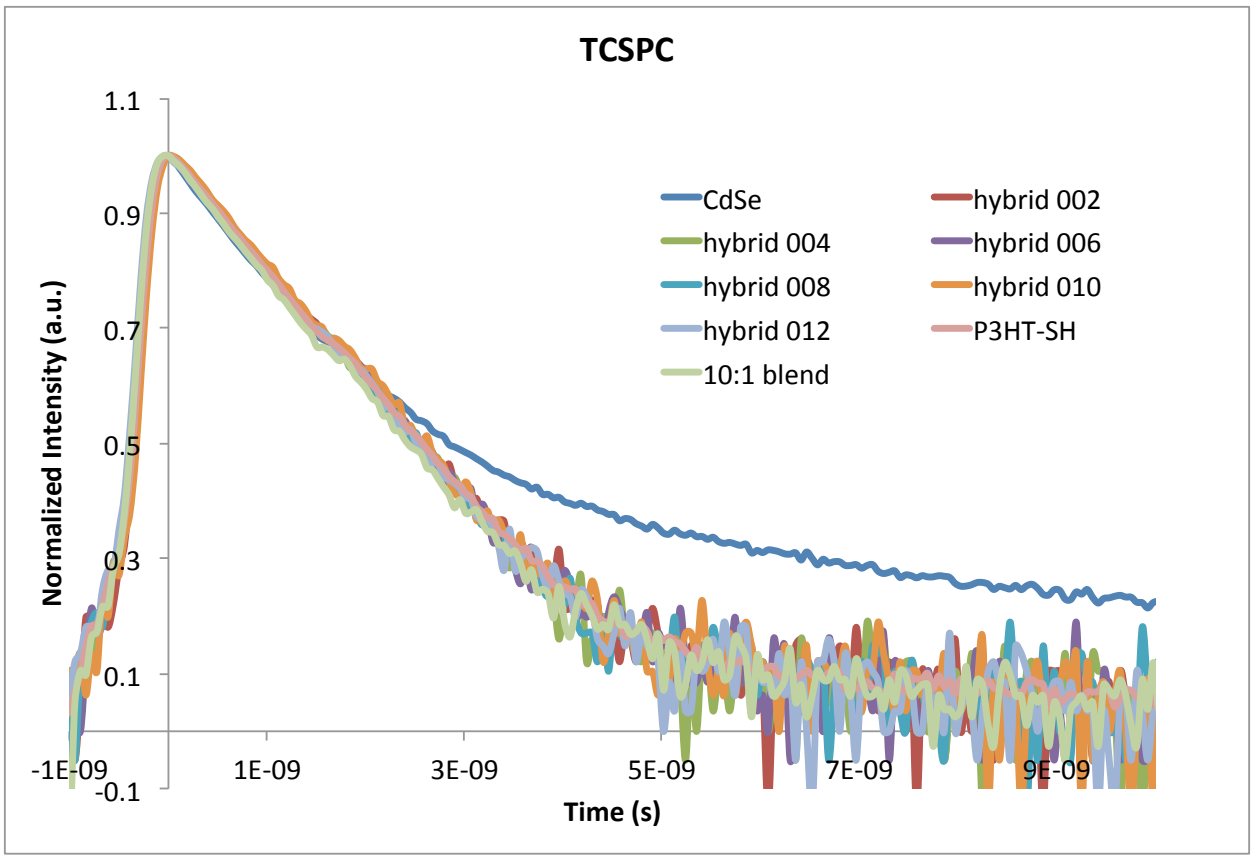

Figure 51: Normalized time-correlated single photon counting spectra for neat CdSe, neat P3HT, a 10:1 blend of CdSe:P3HT, and all hybrid materials.

Table 4: Photoluminesce lifetimes calculated for neat CdSe, neat P3HT, a 10:1 blend of CdSe:P3HT, and all hybrid materials.

P3HT (mmol)	1	0.012	0.01	0.008	0.006	0.004	0.002	0	blend
lifetime (ps)	531	523	521	510	510	506	518	481	503

6.3.7 Transient Absorption Spectroscopy

In order to further investigate the excited state species and their lifetimes that occur upon photoexcitation in these hybrid materials, we looked at femtosecond

transient absorption (TA) spectroscopy. For femtosecond TA, we looked at each sample with 440 nm and 570 nm excitations in an attempt to primarily excite the P3HT and CdSe species, respectively. In order to assign the spectral response of our hybrid materials, we first looked at the photoresponse of the individual CdSe and P3HT-SH components in order to remove these individual responses from the hybrid spectra. For data subtraction, we first normalized the CdSe absorption to 1 at 554 nm and normalized the P3HT absorption to 1 at 725 nm. The hybrid spectra were then normalized to 1 at 554 nm and the normalized CdSe absorption spectra were subtracted from the normalized hybrid absorption spectra. Similarly, the CdSe subtracted hybrid spectra were then normalized to 1 at 725 nm the normalized P3HT spectra were subtracted. The resulting subtracted hybrid data was then unnormalized by multiplying by the two normalization factors. Figure 52 shows an example of a 100 fs-200 fs spectral slice from Hybrid 004 taken with a 440 nm excitation both before and after the removal of any neat CdSe or P3HT contribution.

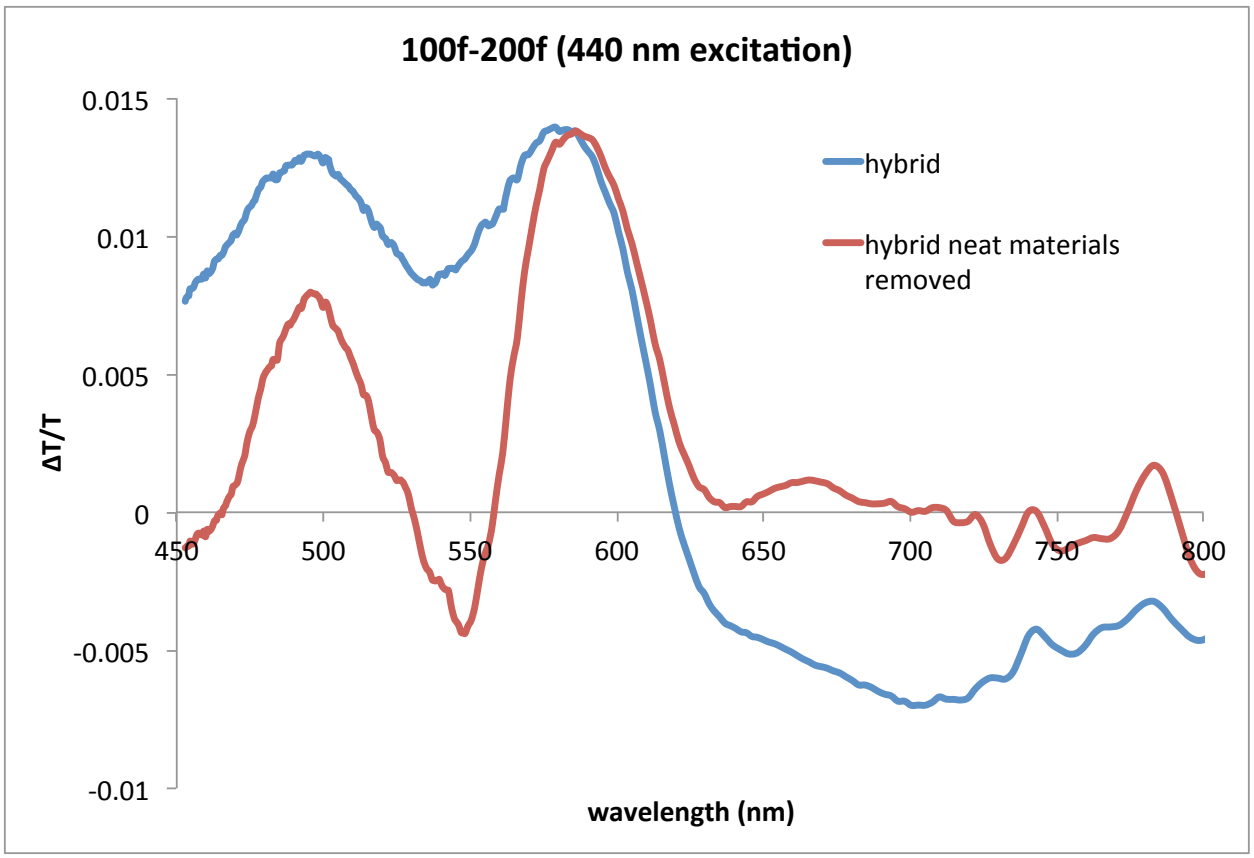

Figure 52: A representative 100-200 fs spectral slice for Hybrid 004 from a data set with a 440 nm before (blue) and after (red) background subtraction of neat CdSe and neat P3HT-SH.

This data subtraction process was performed for each hybrid material with 440 nm and 570 nm pump pulses at a variety of different spectral slices in time, including 100-200 fs, 1-2 ps, 10-20 ps, 100-200 ps, 1-2 ns, and 2.5-3 ns. Figure 53 shows the 570 nm excitation spectral slices for Hybrid 004 both before (thin lines) and after (thick lines) data subtraction for each time series. These subtracted data sets are useful because they can help elucidate the contribution from the hybrid materials to the entire TA absorption spectrum.

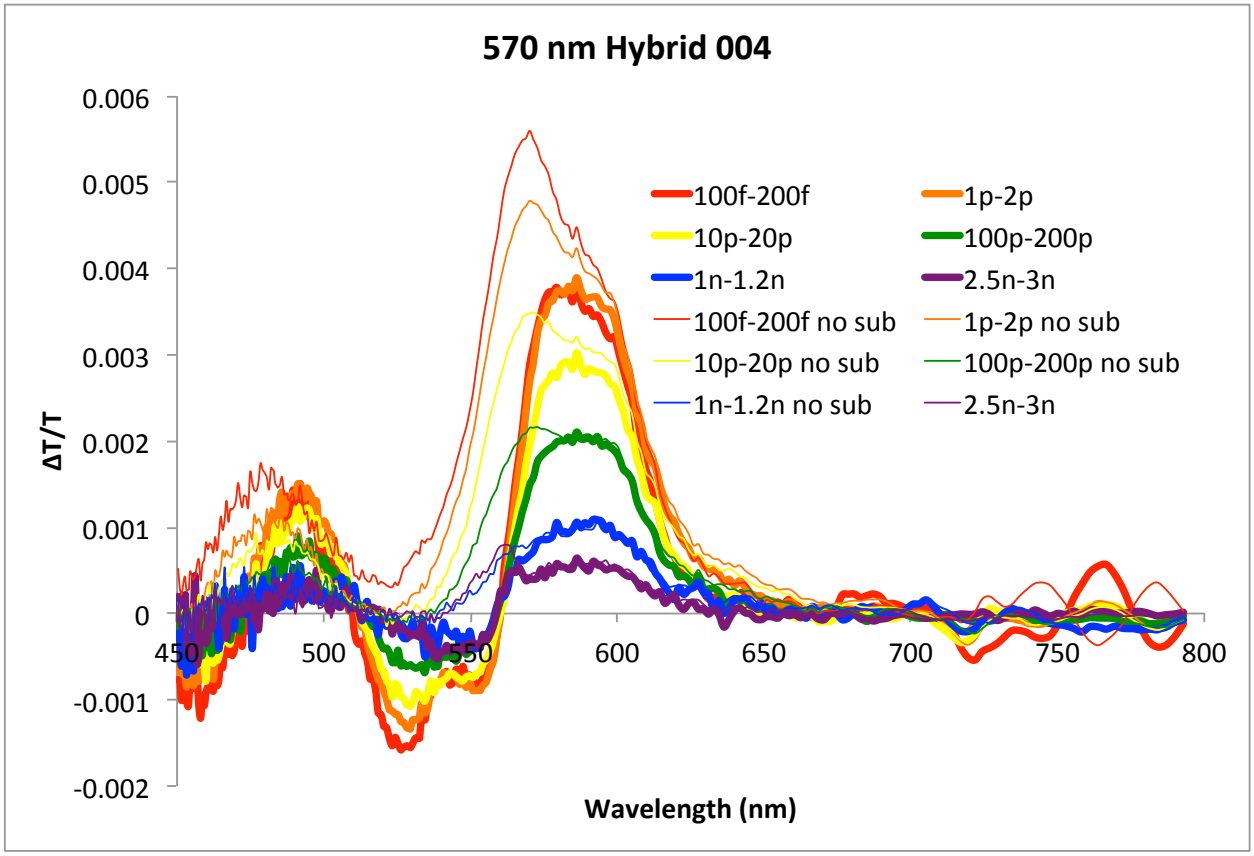

Figure 53: A set of spectral slices from a 570 nm probe data set for Hybrid 004 before (thin lines) and after (thick lines) data subtraction.

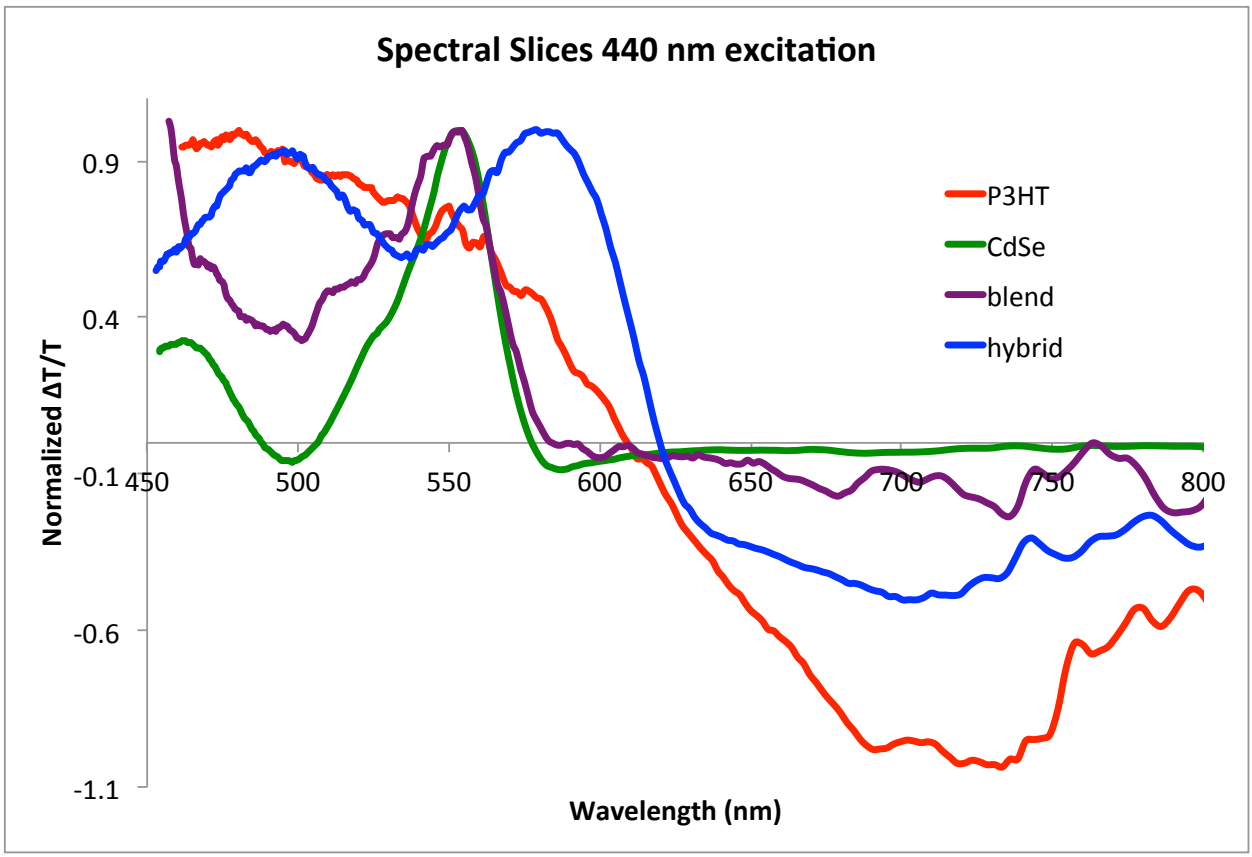

Figure 12: TA spectral slices in the 100-200 fs range with 440 nm excitation of (red) P3HT-SH, (green) CdSe, (purple) 10:1 CdSe:P3HT-SH blend, and (blue) hybrid 004.

A comparison of neat CdSe, a 10:1 blend of CdSe:P3HT-SH, Hybrid 004, and neat P3HT-SH can be used to illustrate several important points. Figure 54 shows the spectral response from each of these samples in the 100-200 fs range when excited by a 440 nm pump signal. 440 nm was chosen because it is near the P3HT maximum absorbance, but both CdSe and P3HT species should absorb this wavelength. With P3HT, we observe a broad bleach signal that extends to just over 600 nm, followed by a large photo-induced absorption (PIA) signal that extends well into the red. CdSe shows a bleach that resembles the first excitonic transition from the UV-Vis. With the hybrid, we observe a broad bleach signal from 450~625 nm, with a peak at approximately 580

nm and a large PIA feature past 650 nm. The bleach is consistent with contributions from both CdSe and P3HT because of its absorption range. It is tempting to attribute the hybrid spectral response to a photoinduced charge transfer process, which we would expect to produce both CdSe and P3HT-based signals. However, similar signals were observed in the blend with similar P3HT and CdSe concentrations, with the main difference being that the bleach from the hybrid sample extends much further into the red. Additionally, the P3HT and CdSe derived signals have different lifetimes, which is inconsistent with them being associated with the same (CT) state. The lifetimes of these materials are reported in Table 5, as determined by fitting the kinetic data obtained by TA to a series of exponential decay functions. Figure 55 provides some examples of kinetic traces at 555 nm and 700 nm. The PIA signal, as measured at 700 nm, resembles that of P3HT, and the kinetics show P3HT decay and lifetimes exclusively in this region. In addition, the kinetic traces show that the hybrid material has a longer lifetime than either free P3HT or CdSe. However, given that the spectrum is also red-shifted, the lifetime extension may be linked to the same electronic perturbation, possibly a CdSe surface modification in the hybrid.

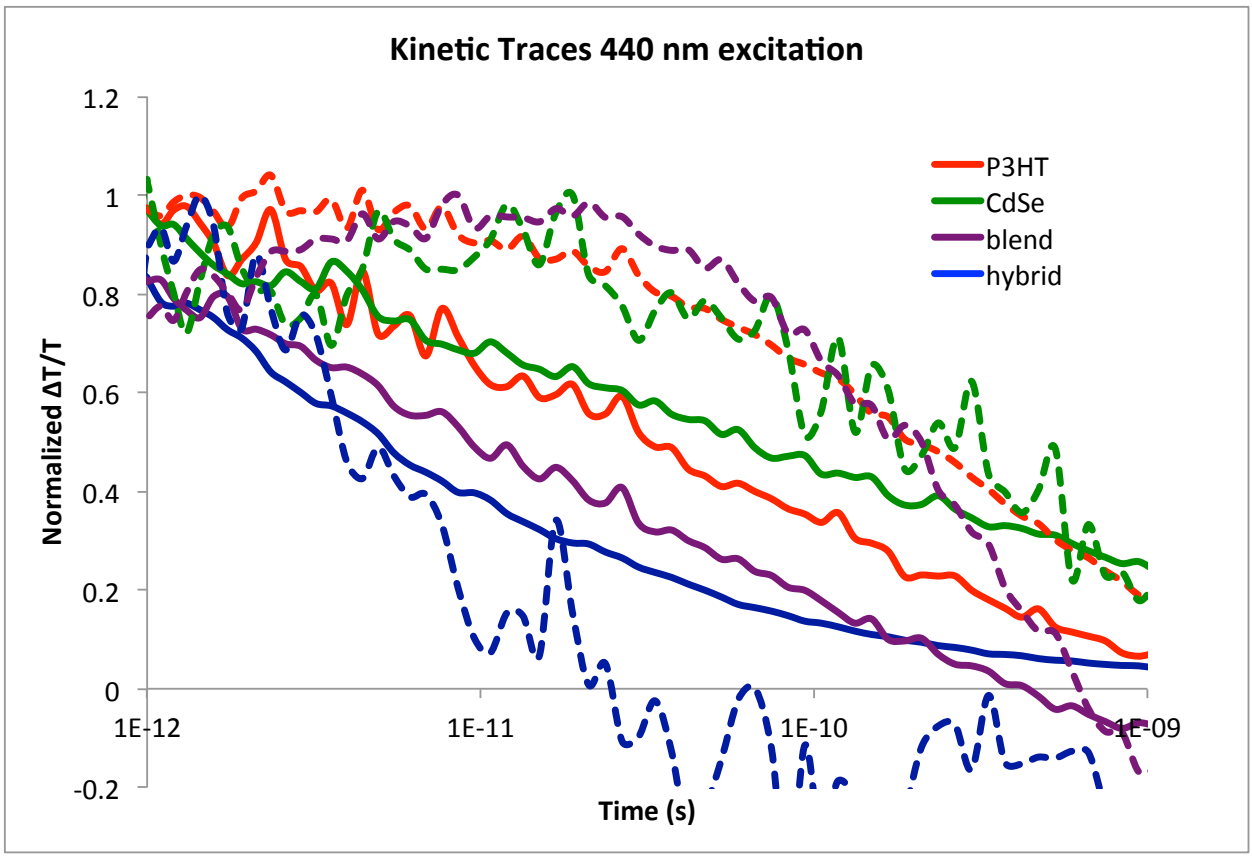

Figure 55: 440 nm excitation TA kinetic traces over (dashed lines) 700 nm and (solid lines) 555 nm for neat CdSe (green), neat P3HT-SH (red), a 10:1 CdSe:P3HT-SH blend (purpe), and hybrid 004 (blue).

Table 5: Kinetic lifetimes for P3HT, CdSe, and hybrid 004 with 440 nm excitation at 555 nm.

Species	τ_1	τ_2	τ_3	τ_4
555 nm P3HT	6.67E-13	1.00E-11	2.00E-10	5.00E+05
555 nm CdSe	3.33E-12	1.43E-10		
555 nm hybrid	1.00E-11	1.00E-10	1.67E-09	

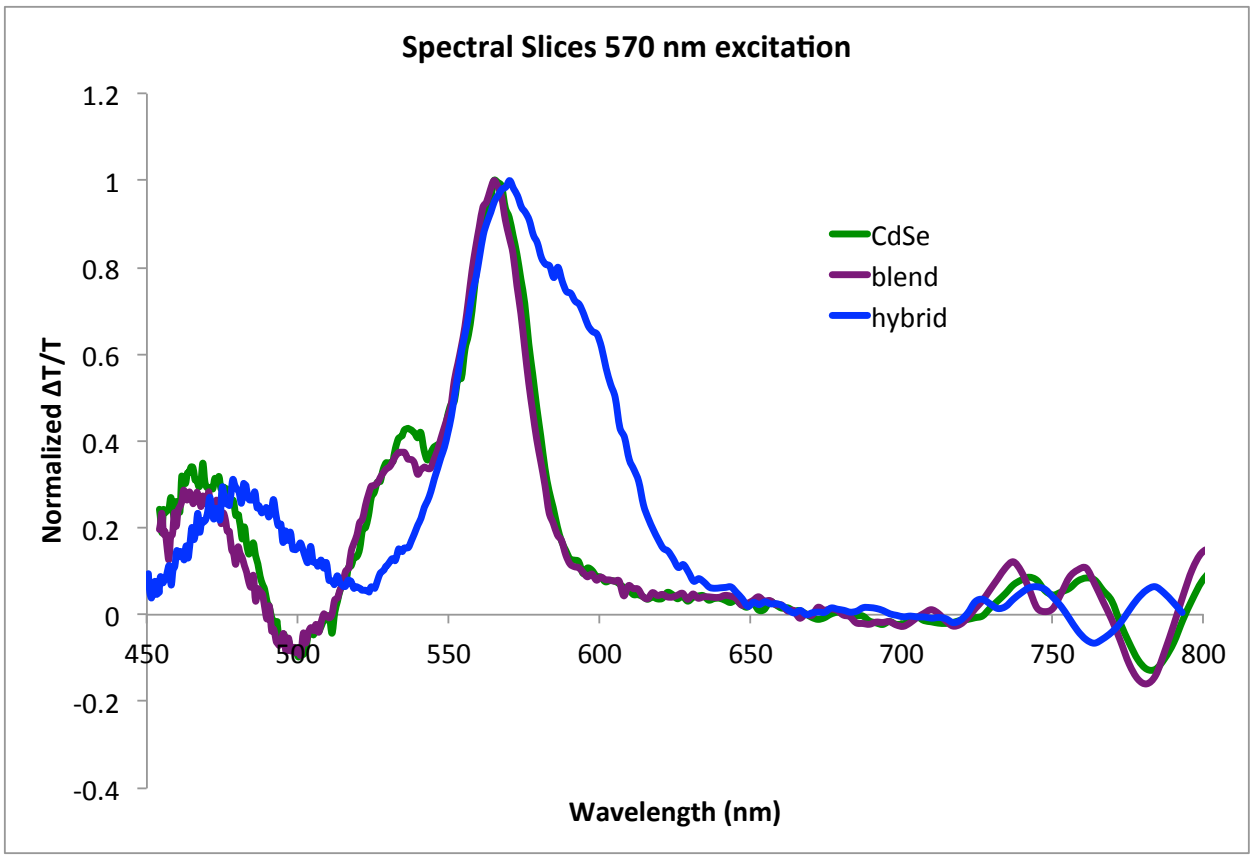

Figure 56: TA spectral slices in the 100-200 fs range with 570 nm excitation of (red) P3HT-SH, (green) CdSe, (purple) 10:1 CdSe:P3HT-SH blend, and (blue) hybrid 004.

In order to directly isolate the CdSe-based features, we then preferentially excited CdSe with a 570 nm pump pulse, and the results of each species from 100-200 fs range can be found in Figure 56. The CdSe spectral response is similar to that of the neat CdSe excited with a 440 nm pump pulse. P3HT does not absorb at 570 nm, so this excitation should not populate the P3HT GSB, and indeed, we do not see its contribution in the blend profile, which matches the neat CdSe spectrum very well. With the hybrid, we can see the population of the CdSe bleach along with a clear redshifted shoulder. The existence of this shoulder with 570 nm excitation confirms that it is exclusively associated with excitations on CdSe. There are no PIA features observed past 650 nm as there are when we excite P3HT, implying that we do not transfer photo

excited holes from CdSe to P3HT. This is an indication of non-optimal energy band alignment or surface states impeding charge transfer. The kinetic data for these materials is presented in Figure 57, and their calculated lifetimes are presented in Table 6. Following the kinetics at 570 nm, which is very close to the max absorbance for the first electronic transition of CdSe, we see that each of the kinetic traces resembles that of CdSe, and that the calculated lifetimes are similar for CdSe and the blend, but the hybrid has one longer lifetime, suggesting that the observed perturbation to CdSe results from the hybridization process. When we examine the kinetics at 605 nm, which is redshifted past the onset of absorption of CdSe, we see no kinetic response in CdSe or the blend, but the hybrid shows similar kinetics as observed at 570 nm, and again with a longer lifetime than that of CdSe.

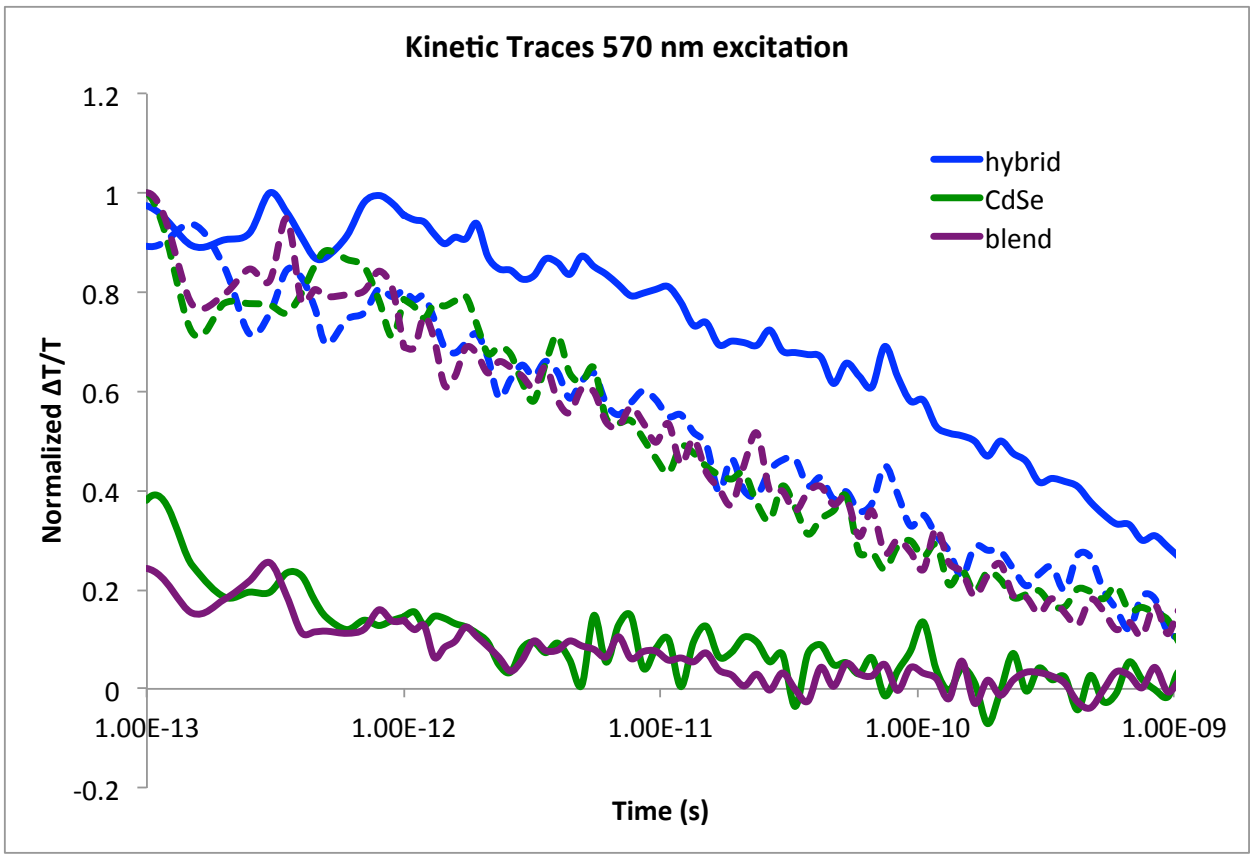

Figure 57: 570 nm excitation TA kinetic traces over (dashed lines) 570 nm and (solid lines) 605 nm for neat CdSe (green), a 10:1 CdSe:P3HT-SH blend (purple), and hybrid 004 (blue).

Table 6: Kinetic lifetimes for CdSe, a 10:1 CdSe:P3HT blend, and hybrid 004 with 570 nm excitation at 570 nm and 605 nm.

Species	τ_1	τ_2	τ_3
605nm hybrid	7.69E-12	1.85E-10	2.56E-09
570nm hybrid	4.55E-12	1.08E-10	1.61E-09
570nm CdSe	3.70E-12	6.25E-11	2.33E-09
570nm blend	9.09E-13	4.55E-11	1.61E-09

6.3.8 Förster Resonance Energy Transfer

These spectral features seem to indicate that we do not have electron transfer in this hybrid system, and instead have energy transfer through a Förster resonance

energy transfer (FRET) process when exciting the higher energy P3HT component. FRET is a mechanism of energy transfer between two chormophores that does not rely on charge transport, and instead, occurs through non-radiative dipole-dipole processes, a schematic of which is shown in Figure 58. There are three main factors that effect the FRET efficiency. These include 1) The distance between the donor and acceptor molecules, 2) the spectral overlap between the donor emission and the acceptor absorption, and 3) the relative orientation of the dipole-dipole interaction of the donor and acceptor molecules. In our case, our hybrid system should meet all three of the criteria that promote efficient FRET processes. We expect the donor/acceptor distance to be much less than the 1-10 nm typically cited as being reasonable for FRET to occur,[213] as the nature of our synthesis requires that they only be separated by the sulfur unit, and as such should have a separation distance on the order of angstroms.

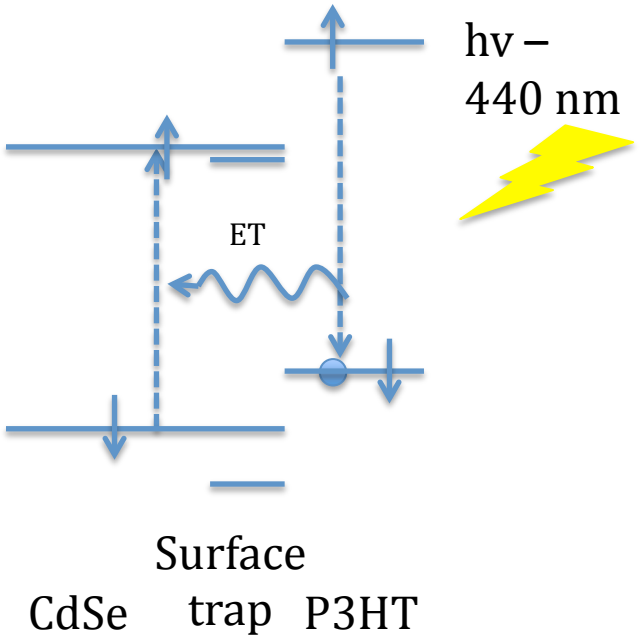

Figure 58: Schematic of FRET for our hybrid system.

Our system also shows good resonance between the CdSe and P3HT, owing to the large spectral overlap between the CdSe absorption and P3HT fluorescence emission, as shown in Figure 59. In addition, we would expect a favorable dipole interaction due to the electronegativity of the sulphur linking atom. Further evidence for a FRET process can be obtained by an estimate of the number of photons absorbed as a ratio of CdSe to P3HT between the blend in solution and the hybrid in solution. With more absorption into the P3HT component of the hybrid, we observe an increase in CdSe-based ground state bleach signal relative to a blend with similar concentration of the two absorbing species. We believe that all of these results point towards a FRET process occurring from the P3HT to CdSe. Finally, we believe that we do not see hole injection after FRET due to surface traps caused by the process of hybridization. We believe that we are effectively forming a CdS monolayer between the P3HT and CdSe and that this is enough to block the back transfer of holes to P3HT.

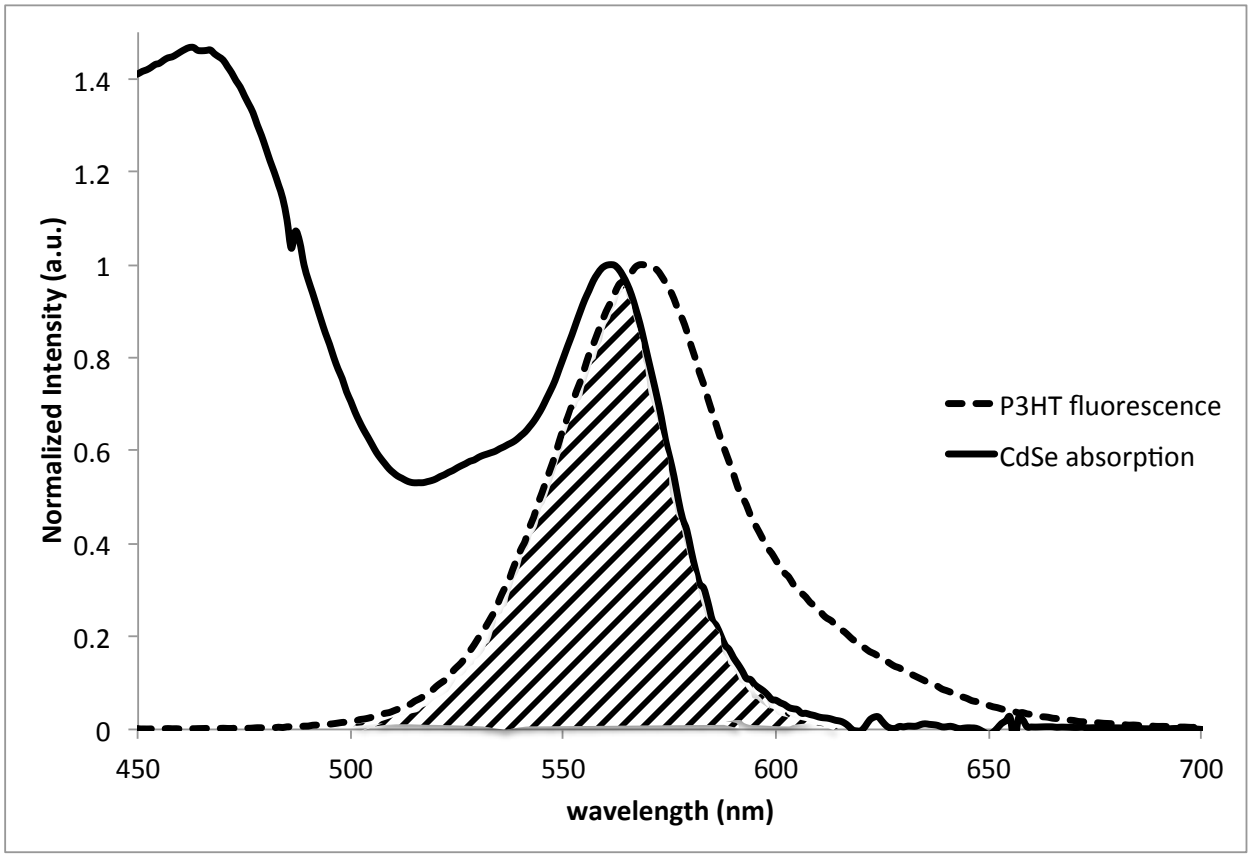

Figure 59: Overlay of (dashed) P3HT fluorescence and (solid) CdSe absorption, highlighting their good spectral overlap.

6.4 Conclusion

In this chapter we first applied the hybrid synthesis method developed in chapter 5 to make a series of P3HT/CdSe hybrid materials, the progress of which was followed by ^{1}H NMR. We then investigated the steady state and time resolved optical properties of the resulting hybrid materials in order to develop an understanding of the excited state processes that occur in these hybrid materials upon photoabsorption. The hybrids were characterized by UV-Vis, phololuminescence, time-resolved photoluminescence, and transient absorption spectroscopies in order to investigate their steady state and time resolved photophysical properties. We found that with hybridization there is a

strong red shift in absorption, which is reflected in both the UV-Vis and spectral slices in the transient absorption spectroscopy. The steady state and time-resolved photoluminescence spectroscopies indicated the existence of free P3HT in solution, and may also indicate that there exists photoluminescence quenching processes that are faster than the resolution of the time-correlated single photon counting system. Through kinetic analysis of the transient absorption spectroscopy of these materials, we found that the observed red shift in absorption with hybridization can be exclusively associated with the CdSe core, and that is most likely a result of a surface perturbation, which we believe is a result of the inclusion of S into the CdSe lattice on the surface. This S incorporation not only affects the optical properties, but it also prevents hole transfer from the CdSe to P3HT. Ultimately, we found that FRET processes are responsible for the observed photophysical properties due to the distance between the donor and acceptor species, their good resonance, and their excellent spectral overlap.

Chapter 7: Future Work and General Conclusions

7.1 Photophysical properties of hybrid materials

In order to wrap up the photophysical studies of our hybrid materials, we would like to perform a quick comparative study to determine if the FRET process is entirely due to surface trap states caused by inclusion of S into the CdSe lattice. Because we hypothesize that the barrier to charge transport in our CdSe/P3HT materials as a result of the incorporation of S into the CdSe lattice at the interface, we will replace the CdSe with CdS to see if this energy barrier remains with better energy matching to the bulk of the nanocrystal. We will again monitor the charge transport properties by TAS in collaboration with the Hodgkiss group at Victoria University of Wellington. In addition, we will examine the effect of hybridization relative to blends of the neat materials in photovoltaic devices. The relative contributions of exciton dissociation and charge transport properties to the performance of solar cells can be obtained by measuring the light intensity dependence of the current density.[214] In current organic solar cells, poor exciton dissociation and high charge carrier recombination generally lead to efficiency decreases with increasing light intensity.[215] The proposed hybrid materials offer many new opportunities for innovation in the design of photovoltaic devices, ranging from better light harvesting and charge transport to novel mechanisms of photovoltage generation.

7.2 General Conclusions

This work has explored interfacial phenomena in organic photovoltaics to investigate and control the charge transport properties of these devices. We first investigated low band gap donor-acceptor small molecules that have HOMO and LUMO energy levels approaching the theoretical optimal energies for efficient exciton dissociation. In addition to ideal energy levels, pi-conjugated small molecules offer several intrinsic benefits relative to their polymeric counterparts, including synthetic consistency and higher hole and electron mobilities due to their propensity to exhibit long-range order. Even with all of these benefits, we found that in our case we were only able to produce solar cells with modest efficiencies. This was attributed to the formation of large domains that were greater than the exciton diffusion length in addition to these large domains resulting in reduced donor-acceptor interfacial area, thus limiting exciton dissociation. This chapter highlights the importance of the active layer morphology for controlling donor-acceptor interfaces. Next, the optical, physical, and charge transport properties of series of fully conjugated brush copolymers were investigated. These polymers were designed to limit thermalization and sub-band gap transmission losses by utilizing polymers with complimentary absorption profiles in addition to promoting efficient exciton dissociation via as stepwise charge separation process, which is common in ternary blend solar cells. We examined a series of brush copolymers comprised of a low band gap donor-acceptor backbone functionalized with different length P3HT chains. A torsional rotation at the nitrogen atom that linked the pendant chains to the backbone provided a sufficient break in conjugation to realize the optical properties of each polymer independently. It was also found that the physical

and electronic properties could be dictated by either the low band gap polymer backbone or the pendant chains, depending on the length of the pendant chains, with short pendant chains resulting in properties being dictated by the backbone, followed by a disruption in the electronic properties with increasing pendant chain length, before the properties becoming dominated by the pendant chain with the longest lengths. This study was followed by investigation of poly(3-methylthiophene) that had been grown from the surface of ITO substrates functionalized with a phosphonic acid (PA) based initiator monolayer. Analysis of the growth process was followed with AFM and optically. In this study, it was found that control over the film thickness could be achieved by regulating the monomer solution concentration. This study was followed by the development of a new synthetic technique for the in-situ functionalization of CdSe nanocrystals with pi-conjugated materials during growth. The process developed relies on the cleavage of a phosphonate group on the desired capping ligand that allows a sulphur unit to then interact with the surface of the CdSe. This new method of functionalization is particularly important when traditional ligand exchange processes prove difficult. Finally, we used this synthetic method for the functionalization of CdSe with P3HT. The goal of this work was to facilitate charge transfer across the surface of the nanocrystal, as this has been shown to be a bottleneck in their use in devices. We investigated the photophysical properties of a series of these hybrid materials and found that they exhibit fluorescence resonance energy transfer between the two materials due to their extremely close contact, good resonance, and large spectral overlap. However, we found that we were unable to achieve the back transfer of holes from the excited

CdSe to P3HT due to surface perturbations caused by the use of a sulphur linking atom. We will investigate this process with CdS to see if we can alleviate this issue.

7.3 List of Publications

7. **Mazzio, K. A.**; Luscombe, C. K. “The Future of Organic Photovoltaics: A Tutorial Review” *Chem. Soc. Rev.,* **2014**, *accepted*

6. Rice, A. H.; **Mazzio, K. A.**; Durban, M. M.; Luscombe, C. K. “The Effect of Regioregularity on Charge Transport and Coherent Domain Size in P3HT Nanowires” *in preparation*

5. Zeigler, D. F.; **Mazzio K. A.**; Luscombe, C. K. “Fully Conjugated Copolymers Comprising a P-type Donor-Acceptor Backbone and Poly(3-hexyl)thiophene Sidechains Synthesized Via a “Graft Through” Approach” *Macromolecules*, **2014**, *47* (15), 5019-5028.

4. Li, Z.; **Mazzio, K. A.**; Okamoto, K.; Luscombe, C. K.; Schlaf, R. “Orbital Alignment at the Internal Interface of Arylthiol (ArSH) Functionalized CdSe Molecular Hybrid Materials” *under review*

3. **Mazzio, K. A.**; Okamoto, K.; Li, Z.; Gutmann, S.; Strein, E.; Ginger, D. S.; Schlaf, R.; Luscombe, C. K. “A one pot organic/CdSe nanoparticle hybrid material synthesis with in situ π-conjugated ligand functionalization” *Chem. Commun.*, **2013**, *49*, 1321-1323.

2. Doubina, N.; Jenkins, J. L.; Paniagua, S. A.; **Mazzio, K. A.**; MacDonald, G. A.; Jen, A. K-Y; Armstrong, N. R.; Marder, S. R.; Luscombe, C. K. “Surface-Initiated Synthesis of Poly(3-methylthiophene) from Indium Tin Oxide and its Electrochemical Properties” *Langmuir*, **2012**, *28* (3), 1900-1908.

1. **Mazzio, K. A.**; Yuan, M. J.; Okamoto, K.; Luscombe, C. K. “Oligoselenophene Derivatives Functionalized with a Diketopyrrolopyrrole Core for Molecular Bulk Heterojunction Solar Cells” *ACS Appl. Mater. Inter.*, **2011**, *3*, 271-278. Top 10 most read article for Q1 2011 for ACS Appl. Mater. Inter.

7.4 Acknowledgements

I would like to thank my advisor, Prof. Christine Luscombe, for the freedom that I have had throughout my graduate program to pursue my own ideas, in addition to her encouragement, advice, and support. I would also like to thank Prof. Lih Lin, Prof. Peter Pauzauskie, and Prof. Xiaohu Gao for agreeing to be on my reading and dissertation defense committees for both challenging me and providing helpful suggestions. I would like to acknowledge Prof. Kannan Krishnan for his time on my general exam committee. Thank you to all of the Luscombe group members past and present that I have interacted with – each of whom have had an effect on my graduate education. Specifically, I would like to acknowledge Dr. Ken Okamoto, Dr. Natalia Doubina, Dr. David Zeigler, and Dr. Mingjian Yuan for making many of the organic polymers and small molecules that I used throughout my Ph.D., Dr. Elisabeth Strein for her introduction to CdSe synthesis, Prof. Rudy Schlaf and Zhi Li at the University of Southern Florida for their XPS work, and Prof. Justin Hodgkiss and Shyamal Prasad at Victoria University of Wellington for all of their help with TCSPC and TAS. Finally, I would like to thank my partner Jeff for putting up with me and taking care of me as I prepared for my thesis defense, as well as my family for all of their love and support.

Some of this work was performed at the University of Washington Nanotech User Facility, a member of the NSF National Nanotechnology Infrastructure Network (NNIN). This work was supported financially by the UW GSFEI, UW GPSS, Frank and Jane Wagstaff, NSF (IGERT 0504573, OISE 1310819, DMR 1035196), and AFOSR FA9550-10-1-0430.

References:

(1) Hoppe, H.; Niggemann, M.; Winder, C.; Kraut, J.; Hiesgen, R.; Hinsch, A.; Meissner, D.; Sariciftci, N. S. *Adv. Funct. Mater.* **2004**, *14*, 1005.

(2) Lee, J. K.; Ma, W. L.; Brabec, C. J.; Yuen, J.; Moon, J. S.; Kim, J. Y.; Lee, K.; Bazan, G. C.; Heeger, A. J. *J. Am. Chem. Soc.* **2008**, *130*, 3619.

(3) Liu, H. T.; Owen, J. S.; Alivisatos, A. P. *J. Am. Chem. Soc.* **2007**, *129*, 305.

(4) International Energy Outlook 2013 - Energy Information Administration http://www.eia.gov/forecasts/ieo/ (accessed May 21, 2014).

(5) NREL Best Research-Cell Efficiencies http://www.nrel.gov/ncpv/images/efficiency_chart.jpg (accessed Jun 18, 2014).

(6) 2013 Technology Map of the European Strategic Energy Technology Plan, JRC Science and Policy Report http://setis.ec.europa.eu/system/files/2013TechnologyMap.pdf (accessed Jun 18, 2014).

(7) Espinosa, N.; Hösel, M.; Angmo, D.; Krebs, F. C. *Energy Environ. Sci.* **2012**, *5*, 5117.

(8) Knapp, K.; Jester, T. *Sol. Energy* **2001**, *71*, 165.

(9) Sariciftci, N. S.; Smilowitz, L.; Heeger, A. J.; Wudl, F. *Science* **1992**, *258*, 1474.

(10) ASTM G173-03 Reference Spectra http://rredc.nrel.gov/solar/spectra/am1.5/ (accessed Jun 28, 2014).

(11) Ong, B. S.; Wu, Y.; Liu, P.; Gardner, S. *J. Am. Chem. Soc.* **2004**, *126*, 3378.

(12) Karg, S.; Riess, W.; Dyakonov, V.; Schwoerer, M. *Synth. Met.* **1993**, *54*, 427.

(13) Tang, C. W. Organic solar cell. US 4164431 A, August 14, 1979.

(14) Tang, C. W. *Appl. Phys. Lett.* **1986**, *48*, 183.

(15) Halls, J. J. M.; Pichler, K.; Friend, R. H.; Moratti, S. C.; Holmes, A. B. *Appl. Phys. Lett.* **1996**, *68*, 3120.

(16) Yu, G.; Gao, J.; Hummelen, J. C.; Wudl, F.; Heeger, A. J. *Science (80-.).* **1995**, *270*, 1789.

(17) Park, S. H.; Roy, A.; Beaupré, S.; Cho, S.; Coates, N.; Moon, J. S.; Moses, D.; Leclerc, M.; Lee, K.; Heeger, A. J. *Nat. Photonics* **2009**, *3*, 297.

(18) De Jong, M. P.; van IJzendoorn, L. J.; de Voigt, M. J. A. *Appl. Phys. Lett.* **2000**, *77*, 2255.

(19) Heliatek consolidates its technology leadership by establishing a new world record for organic solar technology with a cell efficiency of 12% | Heliatek http://www.heliatek.com/newscenter/latest_news/neuer-weltrekord-fur-organische-solarzellen-heliatek-behauptet-sich-mit-12-zelleffizienz-als-technologiefuhrer/?lang=en (accessed Jun 6, 2014).

(20) Ellmer, K. *Nat. Photonics* **2012**, *6*, 809.

(21) Shaheen, S. E.; Brabec, C. J.; Sariciftci, N. S.; Padinger, F.; Fromherz, T.; Hummelen, J. C. *Appl. Phys. Lett.* **2001**, *78*, 841.

(22) Schilinsky, P.; Waldauf, C.; Brabec, C. J. *Appl. Phys. Lett.* **2002**, *81*, 3885.

(23) Padinger, F.; Rittberger, R. S.; Sariciftci, N. S. *Adv. Funct. Mater.* **2003**, *13*, 85.

(24) Kim, Y.; Cook, S.; Tuladhar, S. M.; Choulis, S. A.; Nelson, J.; Durrant, J. R.; Bradley, D. D. C.; Giles, M.; McCulloch, I.; Ha, C.-S.; Ree, M. *Nat. Mater.* **2006**, *5*, 197.

(25) Schilinsky, P.; Asawapirom, U.; Scherf, U.; Biele, M.; Brabec, C. J. *Chem. Mater.* **2005**, *17*, 2175.

(26) Wang, D. H.; Kim, J. K.; Seo, J. H.; Park, I.; Hong, B. H.; Park, J. H.; Heeger, A. J. *Angew. Chem. Int. Ed. Engl.* **2013**, *52*, 2874.

(27) Liang, Y.; Xu, Z.; Xia, J.; Tsai, S.-T.; Wu, Y.; Li, G.; Ray, C.; Yu, L. *Adv. Mater.* **2010**, *22*, E135.

(28) He, Z.; Zhong, C.; Su, S.; Xu, M.; Wu, H.; Cao, Y. *Nat. Photonics* **2012**, *6*, 593.

(29) Sun, Y.; Welch, G. C.; Leong, W. L.; Takacs, C. J.; Bazan, G. C.; Heeger, A. J. *Nat. Mater.* **2012**, *11*, 44.

(30) Mishra, A.; Bäuerle, P. *Angew. Chem. Int. Ed. Engl.* **2012**, *51*, 2020.

(31) Wienk, M. M.; Kroon, J. M.; Verhees, W. J. H.; Knol, J.; Hummelen, J. C.; van Hal, P. A.; Janssen, R. A. J. *Angew. Chem. Int. Ed. Engl.* **2003**, *42*, 3371.

(32) He, Y.; Chen, H.-Y.; Hou, J.; Li, Y. *J. Am. Chem. Soc.* **2010**, *132*, 1377.

(33) He, Y.; Li, Y. *Phys. Chem. Chem. Phys.* **2011**, *13*, 1970.

(34) Ren, S.; Chang, L.-Y.; Lim, S.-K.; Zhao, J.; Smith, M.; Zhao, N.; Bulović, V.; Bawendi, M.; Gradecak, S. *Nano Lett.* **2011**, *11*, 3998.

(35) Celik, D.; Krueger, M.; Veit, C.; Schleiermacher, H. F.; Zimmermann, B.; Allard, S.; Dumsch, I.; Scherf, U.; Rauscher, F.; Niyamakom, P. *Sol. Energy Mater. Sol. Cells* **2012**, *98*, 433.

(36) Zhou, Y.; Eck, M.; Veit, C.; Zimmermann, B.; Rauscher, F.; Niyamakom, P.; Yilmaz, S.; Dumsch, I.; Allard, S.; Scherf, U. *Sol. Energy Mater. Sol. Cells* **2011**, *95*, 1232.

(37) Kamat, P. V. *J. Phys. Chem. C* **2008**, *112*, 18737.

(38) Kongkanand, A.; Tvrdy, K.; Takechi, K.; Kuno, M.; Kamat, P. V. *J. Am. Chem. Soc.* **2008**, *130*, 4007.

(39) Kim, J.-P.; Christians, J. A.; Choi, H.; Krishnamurthy, S.; Kamat, P. V. *J. Phys. Chem. Lett.* **2014**, 140311155651009.

(40) Robel, I.; Kuno, M.; Kamat, P. V. *J. Am. Chem. Soc.* **2007**, *129*, 4136.

(41) Wright, M.; Uddin, A. *Sol. Energy Mater. Sol. Cells* **2012**, *107*, 87.

(42) Beek, W. J. E.; Wienk, M. M.; Janssen, R. A. J. *Adv. Mater.* **2004**, *16*, 1009.

(43) Morgenstern, F. S. F.; Rao, A.; Böhm, M. L.; Kist, R. J. P.; Vaynzof, Y.; Greenham, N. C. *ACS Nano* **2014**, *8*, 1647.

(44) Huang, J.; Huang, Z.; Yang, Y.; Zhu, H.; Lian, T. *J. Am. Chem. Soc.* **2010**, *132*, 4858.

(45) Manna, L.; Scher, E. C.; Alivisatos, A. P. *J. Am. Chem. Soc.* **2000**, *122*, 12700.

(46) Sun, B.; Marx, E.; Greenham, N. C. *Nano Lett.* **2003**, *3*, 961.

(47) Huynh, W. U.; Dittmer, J. J.; Libby, W. C.; Whiting, G. L.; Alivisatos, A. P. *Adv. Funct. Mater.* **2003**, *13*, 73.

(48) Markov, D. E.; Amsterdam, E.; Blom, P. W. M.; Sieval, A. B.; Hummelen, J. C. *J. Phys. Chem. A* **2005**, *109*, 5266.

(49) Sim, M.; Shin, J.; Shim, C.; Kim, M.; Jo, S. B.; Kim, J.-H.; Cho, K. *J. Phys. Chem. C* **2014**, *118*, 760.

(50) Chen, L.-M.; Hong, Z.; Li, G.; Yang, Y. *Adv. Mater.* **2009**, *21*, 1434.

(51) Vandewal, K.; Himmelberger, S.; Salleo, A. *Macromolecules* **2013**, *46*, 6379.

(52) Liu, F.; Gu, Y.; Jung, J. W.; Jo, W. H.; Russell, T. P. *J. Polym. Sci. Part B Polym. Phys.* **2012**, *50*, 1018.

(53) Li, G.; Yao, Y.; Yang, H.; Shrotriya, V.; Yang, G.; Yang, Y. *Adv. Funct. Mater.* **2007**, *17*, 1636.

(54) Ma, W.; Yang, C.; Gong, X.; Lee, K.; Heeger, A. J. *Adv. Funct. Mater.* **2005**, *15*, 1617.

(55) Mihailetchi, V. D.; Xie, H. X.; de Boer, B.; Koster, L. J. A.; Blom, P. W. M. *Adv. Funct. Mater.* **2006**, *16*, 699.

(56) Chen, D.; Nakahara, A.; Wei, D.; Nordlund, D.; Russell, T. P. *Nano Lett.* **2011**, *11*, 561.

(57) Campoy-Quiles, M.; Ferenczi, T.; Agostinelli, T.; Etchegoin, P. G.; Kim, Y.; Anthopoulos, T. D.; Stavrinou, P. N.; Bradley, D. D. C.; Nelson, J. *Nat. Mater.* **2008**, *7*, 158.

(58) Park, J. H.; Kim, J. S.; Lee, J. H.; Lee, W. H.; Cho, K. *J. Phys. Chem. C* **2009**, *113*, 17579.

(59) Jo, J.; Na, S.-I.; Kim, S.-S.; Lee, T.-W.; Chung, Y.; Kang, S.-J.; Vak, D.; Kim, D.-Y. *Adv. Funct. Mater.* **2009**, *19*, 2398.

(60) Chu, C.-W.; Yang, H.; Hou, W.-J.; Huang, J.; Li, G.; Yang, Y. *Appl. Phys. Lett.* **2008**, *92*, 103306.

(61) Peet, J.; Kim, J. Y.; Coates, N. E.; Ma, W. L.; Moses, D.; Heeger, A. J.; Bazan, G. C. *Nat. Mater.* **2007**, *6*, 497.

(62) Burke, T. M.; McGehee, M. D. *Adv. Mater.* **2013**, n/a.

(63) Watts, B.; Belcher, W. J.; Thomsen, L.; Ade, H.; Dastoor, P. C. *Macromolecules* **2009**, *42*, 8392.

(64) Krebs, F. C. *Sol. Energy Mater. Sol. Cells* **2009**, *93*, 393.

(65) Thompson, B. C.; Fréchet, J. M. J. *Angew. Chem. Int. Ed. Engl.* **2008**, *47*, 58.

(66) Liang, Y.; Wu, Y.; Feng, D.; Tsai, S.-T.; Son, H.-J.; Li, G.; Yu, L. *J. Am. Chem. Soc.* **2009**, *131*, 56.

(67) Piliego, C.; Holcombe, T. W.; Douglas, J. D.; Woo, C. H.; Beaujuge, P. M.; Fréchet, J. M. J. *J. Am. Chem. Soc.* **2010**, *132*, 7595.

(68) Scharber, M. C.; Mühlbacher, D.; Koppe, M.; Denk, P.; Waldauf, C.; Heeger, a. J.; Brabec, C. J. *Adv. Mater.* **2006**, *18*, 789.

(69) Chen, C.-P.; Chan, S.-H.; Chao, T.-C.; Ting, C.; Ko, B.-T. *J. Am. Chem. Soc.* **2008**, *130*, 12828.

(70) Wang, E.; Wang, L.; Lan, L.; Luo, C.; Zhuang, W.; Peng, J.; Cao, Y. *Appl. Phys. Lett.* **2008**, *92*, 033307.

(71) Wu, P.-T.; Bull, T.; Kim, F. S.; Luscombe, C. K.; Jenekhe, S. A. *Macromolecules* **2009**, *42*, 671.

(72) Xiao, S.; Zhou, H.; You, W. *Macromolecules* **2008**, *41*, 5688.

(73) Yang, P.; Zhou, X.; Cao, G.; Luscombe, C. K. *J. Mater. Chem.* **2010**, *20*, 2612.

(74) Zhang, Y.; Hau, S. K.; Yip, H.-L.; Sun, Y.; Acton, O.; Jen, A. K.-Y. *Chem. Mater.* **2010**, *22*, 2696.

(75) Zhou, E.; Yamakawa, S.; Zhang, Y.; Tajima, K.; Yang, C.; Hashimoto, K. *J. Mater. Chem.* **2009**, *19*, 7730.

(76) Schmidt-Mende, L.; Fechtenkötter, A.; Müllen, K.; Moons, E.; Friend, R. H.; MacKenzie, J. D. *Science* **2001**, *293*, 1119.

(77) Sun, M.; Wang, L.; Zhu, X.; Du, B.; Liu, R.; Yang, W.; Cao, Y. *Sol. Energy Mater. Sol. Cells* **2007**, *91*, 1681.

(78) Tamayo, A. B.; Walker, B.; Nguyen*, T.-Q. *J. Phys. Chem. C* **2008**, *112*, 11545.

(79) Zhou, J.; Zuo, Y.; Wan, X.; Long, G.; Zhang, Q.; Ni, W.; Liu, Y.; Li, Z.; He, G.; Li, C.; Kan, B.; Li, M.; Chen, Y. *J. Am. Chem. Soc.* **2013**, *135*, 8484.

(80) Patra, A.; Bendikov, M. *J. Mater. Chem.* **2010**, *20*, 422.

(81) Chen, Z.; Lemke, H.; Albert-Seifried, S.; Caironi, M.; Nielsen, M. M.; Heeney, M.; Zhang, W.; McCulloch, I.; Sirringhaus, H. *Adv. Mater.* **2010**, *22*, 2371.

(82) Cho, N. S.; Lee, S. K.; Seo, J. H.; Elbing, M.; Azoulay, J. D.; Park, J.; Cho, S.; Heeger, A. J.; Bazan, G. C. *J. Mater. Chem.* **2008**, *18*, 4909.

(83) Gao, F.; Cheng, Y.; Yu, Q.; Liu, S.; Shi, D.; Li, Y.; Wang, P. *Inorg. Chem.* **2009**, *48*, 2664.

(84) Kong, H.; Jung, Y. K.; Cho, N. S.; Kang, I.-N.; Park, J.-H.; Cho, S.; Shim, H.-K. *Chem. Mater.* **2009**, *21*, 2650.

(85) Mazzio, K. a; Yuan, M.; Okamoto, K.; Luscombe, C. K. *ACS Appl. Mater. Interfaces* **2011**, *3*, 271.

(86) Bijleveld, J. C.; Zoombelt, A. P.; Mathijssen, S. G. J.; Wienk, M. M.; Turbiez, M.; de Leeuw, D. M.; Janssen, R. A. J. *J. Am. Chem. Soc.* **2009**, *131*, 16616.

(87) Wienk, M. M.; Turbiez, M.; Gilot, J.; Janssen, R. A. J. *Adv. Mater.* **2008**, *20*, 2556.

(88) Zou, Y.; Gendron, D.; Badrou-Aïch, R.; Najari, A.; Tao, Y.; Leclerc, M. *Macromolecules* **2009**, *42*, 2891.

(89) Nelson, T. L.; Young, T. M.; Liu, J.; Mishra, S. P.; Belot, J. A.; Balliet, C. L.; Javier, A. E.; Kowalewski, T.; McCullough, R. D. *Adv. Mater.* **2010**, *22*, 4617.

(90) Bijleveld, J. C.; Gevaerts, V. S.; Di Nuzzo, D.; Turbiez, M.; Mathijssen, S. G. J.; de Leeuw, D. M.; Wienk, M. M.; Janssen, R. A. J. *Adv. Mater.* **2010**, *22*, E242.

(91) Woo, C. H.; Beaujuge, P. M.; Holcombe, T. W.; Lee, O. P.; Fréchet, J. M. J. *J. Am. Chem. Soc.* **2010**, *132*, 15547.

(92) Tamayo, A. B.; Tantiwiwat, M.; Walker, B.; Nguyen, T.-Q. *J. Phys. Chem. C* **2008**, *112*, 15543.

(93) Tamayo, A. B.; Dang, X.-D.; Walker, B.; Seo, J.; Kent, T.; Nguyen, T.-Q. *Appl. Phys. Lett.* **2009**, *94*, 103301.

(94) Huo, L.; Hou, J.; Chen, H.-Y.; Zhang, S.; Jiang, Y.; Chen, T. L.; Yang, Y. *Macromolecules* **2009**, *42*, 6564.

(95) Wallquist, O.; Lenz, R. *Macromol. Symp.* **2002**, *187*, 617.

(96) Smith, J.; Heeney, M.; McCulloch, I.; Malik, J. N.; Stingelin, N.; Bradley, D. D. C.; Anthopoulos, T. D. *Org. Electron.* **2011**, *12*, 143.

(97) Polman, A.; Atwater, H. A. *Nat. Mater.* **2012**, *11*, 174.

(98) Ameri, T.; Li, N.; Brabec, C. J. *Energy Environ. Sci.* **2013**, *6*, 2390.

(99) Riede, M.; Uhrich, C.; Widmer, J.; Timmreck, R.; Wynands, D.; Schwartz, G.; Gnehr, W.-M.; Hildebrandt, D.; Weiss, A.; Hwang, J.; Sundarraj, S.; Erk, P.; Pfeiffer, M.; Leo, K. *Adv. Funct. Mater.* **2011**, *21*, 3019.

(100) You, J.; Dou, L.; Yoshimura, K.; Kato, T.; Ohya, K.; Moriarty, T.; Emery, K.; Chen, C.-C.; Gao, J.; Li, G.; Yang, Y. *Nat. Commun.* **2013**, *4*, 1446.

(101) Kim, J. Y.; Lee, K.; Coates, N. E.; Moses, D.; Nguyen, T.-Q.; Dante, M.; Heeger, A. J. *Science* **2007**, *317*, 222.

(102) Dennler, G.; Scharber, M. C.; Ameri, T.; Denk, P.; Forberich, K.; Waldauf, C.; Brabec, C. J. *Adv. Mater.* **2008**, *20*, 579.

(103) Yang, J.; Zhu, R.; Hong, Z.; He, Y.; Kumar, A.; Li, Y.; Yang, Y. *Adv. Mater.* **2011**, *23*, 3465.

(104) Jo, J.; Pouliot, J.-R.; Wynands, D.; Collins, S. D.; Kim, J. Y.; Nguyen, T. L.; Woo, H. Y.; Sun, Y.; Leclerc, M.; Heeger, A. J. *Adv. Mater.* **2013**, *25*, 4783.

(105) Li, K.; Li, Z.; Feng, K.; Xu, X.; Wang, L.; Peng, Q. *J. Am. Chem. Soc.* **2013**, *135*, 13549.

(106) Meiss, J.; Menke, T.; Leo, K.; Uhrich, C.; Gnehr, W.-M.; Sonntag, S.; Pfeiffer, M.; Riede, M. *Appl. Phys. Lett.* **2012**, *100*, 099901.

(107) Dennler, G.; Prall, H.-J.; Koeppe, R.; Egginger, M.; Autengruber, R.; Sariciftci, N. S. *Appl. Phys. Lett.* **2006**, *89*, 073502.

(108) Green, M. A.; Emery, K.; Hishikawa, Y.; Warta, W.; Dunlop, E. D. *Prog. Photovoltaics Res. Appl.* **2013**, *21*, 1.

(109) Kuo, C.-Y.; Nie, W.; Tsai, H.; Yen, H.-J.; Mohite, A. D.; Gupta, G.; Dattelbaum, A. M.; William, D. J.; Cha, K. C.; Yang, Y.; Wang, L.; Wang, H.-L. *Macromolecules* **2014**, *47*, 1008.

(110) Zen, A.; Pflaum, J.; Hirschmann, S.; Zhuang, W.; Jaiser, F.; Asawapirom, U.; Rabe, J. P.; Scherf, U.; Neher, D. *Adv. Funct. Mater.* **2004**, *14*, 757.

(111) Bao, Z.; Lovinger, A. J. *Chem. Mater.* **1999**, *11*, 2607.

(112) Günes, S.; Neugebauer, H.; Sariciftci, N. S. *Chem. Rev.* **2007**, *107*, 1324.

(113) Iovu, M. C.; Jeffries-EL, M.; Sheina, E. E.; Cooper, J. R.; McCullough, R. D. *Polymer (Guildf).* **2005**, *46*, 8582.

(114) McCullough, R. D.; Lowe, R. D. *J. Chem. Soc. Chem. Commun.* **1992**, 70.

(115) Miyakoshi, R.; Yokoyama, A.; Yokozawa, T. *J. Am. Chem. Soc.* **2005**, *127*, 17542.

(116) Reyes-Reyes, M.; Kim, K.; Carroll, D. L. *Appl. Phys. Lett.* **2005**, *87*, 083506.

(117) Sacco, A.; Mastrorilli, P. *J. Chem. Soc. Dalt. Trans.* **1994**, 2761.

(118) Sirringhaus, H.; Brown, P. J.; Friend, R. H.; Nielsen, M. M.; Bechgaard, K.; Langeveld-Voss, B. M. W.; Spiering, A. J. H.; Janssen, R. A. J.; Meijer, E. W.; Herwig, P.; de Leeuw, D. M. *Nature* **1999**, *401*, 685.

(119) Loewe, R. S.; Khersonsky, S. M.; McCullough, R. D. *Adv. Mater.* **1999**, *11*, 250.

(120) McCullough, R. D. *Adv. Mater.* **1998**, *10*, 93.

(121) Whiting, G. L.; Snaith, H. J.; Khodabakhsh, S.; Andreasen, J. W.; Breiby, D. W.; Nielsen, M. M.; Greenham, N. C.; Friend, R. H.; Huck, W. T. S. *Nano Lett.* **2006**, *6*, 573.

(122) Snaith, H. J.; Whiting, G. L.; Sun, B.; Greenham, N. C.; Huck, W. T. S.; Friend, R. H. *Nano Lett.* **2005**, *5*, 1653.

(123) Inaoka, S.; Collard, D. M. *Langmuir* **1999**, *15*, 3752.

(124) Nakashima, H.; Furukawa, K.; Ajito, K.; Kashimura, Y.; Torimitsu, K. *Langmuir* **2005**, *21*, 511.

(125) Zotti, G.; Zecchin, S.; Vercelli, B.; Berlin, A.; Grimoldi, S.; Groenendaal, L.; Bertoncello, R.; Natali, M. *Chem. Mater.* **2005**, *17*, 3681.

(126) Hains, A. W.; Ramanan, C.; Irwin, M. D.; Liu, J.; Wasielewski, M. R.; Marks, T. J. *ACS Appl. Mater. Interfaces* **2010**, *2*, 175.

(127) Ma, H.; Yip, H.-L.; Huang, F.; Jen, A. K.-Y. *Adv. Funct. Mater.* **2010**, *20*, 1371.

(128) Ayres, N. *Polym. Chem.* **2010**, *1*, 769.

(129) Paoprasert, P.; Spalenka, J. W.; Peterson, D. L.; Ruther, R. E.; Hamers, R. J.; Evans, P. G.; Gopalan, P. *J. Mater. Chem.* **2010**, *20*, 2651.

(130) Prucker, O.; Rühe, J. *Macromolecules* **1998**, *31*, 592.

(131) Li, Y.; Benicewicz, B. C. *Macromolecules* **2008**, *41*, 7986.

(132) Barbey, R.; Lavanant, L.; Paripovic, D.; Schüwer, N.; Sugnaux, C.; Tugulu, S.; Klok, H.-A. *Chem. Rev.* **2009**, *109*, 5437.

(133) Radhakrishnan, B.; Ranjan, R.; Brittain, W. J. *Soft Matter* **2006**, *2*, 386.

(134) Stenzel, M. H. *Macromol. Rapid Commun.* **2009**, *30*, 1603.

(135) Jiang, G.; Ponnapati, R.; Pernites, R.; Felipe, M. J.; Advincula, R. *Macromolecules* **2010**, *43*, 10262.

(136) Kim, N. Y.; Jeon, N. L.; Choi, I. S.; Takami, S.; Harada, Y.; Finnie, K. R.; Girolami, G. S.; Nuzzo, R. G.; Whitesides, G. M.; Laibinis, P. E. *Macromolecules* **2000**, *33*, 2793.

(137) Rutenberg, I. M.; Scherman, O. A.; Grubbs, R. H.; Jiang, W.; Garfunkel, E.; Bao, Z. *J. Am. Chem. Soc.* **2004**, *126*, 4062.

(138) Rastogi, A.; Paik, M. Y.; Tanaka, M.; Ober, C. K. *ACS Nano* **2010**, *4*, 771.

(139) Matyjaszewski, K.; Miller, P. J.; Shukla, N.; Immaraporn, B.; Gelman, A.; Luokala, B. B.; Siclovan, T. M.; Kickelbick, G.; Vallant, T.; Hoffmann, H.; Pakula, T. *Macromolecules* **1999**, *32*, 8716.

(140) Ding, L.; Huang, Y.; Zhang, Y.; Deng, J.; Yang, W. *Macromolecules* **2011**, *44*, 736.

(141) Riachi, C.; Schüwer, N.; Klok, H.-A. *Macromolecules* **2009**, *42*, 8076.

(142) Kim, B. Y.; Ratcliff, E. L.; Armstrong, N. R.; Kowalewski, T.; Pyun, J. *Langmuir* **2010**, *26*, 2083.

(143) Beryozkina, T.; Boyko, K.; Khanduyeva, N.; Senkovskyy, V.; Horecha, M.; Oertel, U.; Simon, F.; Stamm, M.; Kiriy, A. *Angew. Chem. Int. Ed. Engl.* **2009**, *48*, 2695.

(144) Jhaveri, S. B.; Peterson, J. J.; Carter, K. R. *Langmuir* **2009**, *25*, 9552.

(145) Senkovskyy, V.; Khanduyeva, N.; Komber, H.; Oertel, U.; Stamm, M.; Kuckling, D.; Kiriy, A. *J. Am. Chem. Soc.* **2007**, *129*, 6626.

(146) Khanduyeva, N.; Senkovskyy, V.; Beryozkina, T.; Horecha, M.; Stamm, M.; Uhrich, C.; Riede, M.; Leo, K.; Kiriy, A. *J. Am. Chem. Soc.* **2009**, *131*, 153.

(147) Khanduyeva, N.; Senkovskyy, V.; Beryozkina, T.; Bocharova, V.; Simon, F.; Nitschke, M.; Stamm, M.; Grötzschel, R.; Kiriy, A. *Macromolecules* **2008**, *41*, 7383.

(148) Tkachov, R.; Senkovskyy, V.; Horecha, M.; Oertel, U.; Stamm, M.; Kiriy, A. *Chem. Commun. (Camb).* **2010**, *46*, 1425.

(149) Senkovskyy, V.; Tkachov, R.; Beryozkina, T.; Komber, H.; Oertel, U.; Horecha, M.; Bocharova, V.; Stamm, M.; Gevorgyan, S. A.; Krebs, F. C.; Kiriy, A. *J. Am. Chem. Soc.* **2009**, *131*, 16445.

(150) Sontag, S. K.; Marshall, N.; Locklin, J. *Chem. Commun. (Camb).* **2009**, 3354.

(151) Marshall, N.; Sontag, S. K.; Locklin, J. *Macromolecules* **2010**, *43*, 2137.

(152) Sontag, S. K.; Sheppard, G. R.; Usselman, N. M.; Marshall, N.; Locklin, J. *Langmuir* **2011**, *27*, 12033.

(153) Miyakoshi, R.; Yokoyama, A.; Yokozawa, T. *J. Polym. Sci. Part A Polym. Chem.* **2008**, *46*, 753.

(154) Yokoyama, A.; Miyakoshi, R.; Yokozawa, T. *Macromolecules* **2004**, *37*, 1169.

(155) Iovu, M. C.; Sheina, E. E.; Gil, R. R.; McCullough, R. D. *Macromolecules* **2005**, *38*, 8649.

(156) Beryozkina, T.; Senkovskyy, V.; Kaul, E.; Kiriy, A. *Macromolecules* **2008**, *41*, 7817.

(157) Smeets, A.; Van den Bergh, K.; De Winter, J.; Gerbaux, P.; Verbiest, T.; Koeckelberghs, G. *Macromolecules* **2009**, *42*, 7638.

(158) Doubina, N.; Stoddard, M.; Bronstein, H. A.; Jen, A. K.-Y.; Luscombe, C. K. *Macromol. Chem. Phys.* **2009**, *210*, 1966.

(159) Doubina, N.; Ho, A.; Jen, A. K.-Y.; Luscombe, C. K. *Macromolecules* **2009**, *42*, 7670.

(160) Doubina, N.; Paniagua, S. A.; Soldatova, A. V.; Jen, A. K. Y.; Marder, S. R.; Luscombe, C. K. *Macromolecules* **2011**, *44*, 512.

(161) Bronstein, H. A.; Luscombe, C. K. *J. Am. Chem. Soc.* **2009**, *131*, 12894.

(162) Usov, D.; Gruzdev, V.; Nitschke, M.; Stamm, M.; Hoy, O.; Luzinov, I.; Tokarev, I.; Minko, S. *Macromolecules* **2007**, *40*, 8774.

(163) Ishida, N.; Biggs, S. *Langmuir* **2007**, *23*, 11083.

(164) Luscombe, C. K.; Li, H.-W.; Huck, W. T. S.; Holmes, A. B. *Langmuir* **2003**, *19*, 5273.

(165) Ratcliff, E. L.; Zacher, B.; Armstrong, N. R. *J. Phys. Chem. Lett.* **2011**, *2*, 1337.

(166) Sontag, S. K.; Sheppard, G. R.; Usselman, N. M.; Marshall, N.; Locklin, J. *Langmuir* **2011**, *27*, 12033.

(167) Estillore, N. C.; Park, J. Y.; Advincula, R. C. *Macromolecules* **2010**, *43*, 6588.

(168) Jayachandran, K. N.; Takacs-Cox, A.; Brooks, D. E. *Macromolecules* **2002**, *35*, 4247.

(169) Samanta, S.; Locklin, J. *Langmuir* **2008**, *24*, 9558.

(170) Lanni, E. L.; McNeil, A. J. *Macromolecules* **2010**, *43*, 8039.

(171) Lanni, E. L.; Locke, J. R.; Gleave, C. M.; McNeil, A. J. *Macromolecules* **2011**, *44*, 5136.

(172) Bullen, C.; Mulvaney, P. *Langmuir* **2006**, *22*, 3007.

(173) Medintz, I. L.; Uyeda, H. T.; Goldman, E. R.; Mattoussi, H. *Nat. Mater.* **2005**, *4*, 435.

(174) Kagan, C. R.; Murray, C. B.; Nirmal, M.; Bawendi, M. G. *Phys. Rev. Lett.* **1996**, *76*, 1517.

(175) Ning, Z.; Molnár, M.; Chen, Y.; Friberg, P.; Gan, L.; Ågren, H.; Fu, Y. *Phys. Chem. Chem. Phys.* **2011**, *13*, 5848.

(176) Querner, C.; Reiss, P.; Bleuse, J.; Pron, A. *J. Am. Chem. Soc.* **2004**, *126*, 11574.

(177) Mathew, S.; Saran, A. D.; Bhardwaj, B. S.; Joseph, S. A.; Radhakrishnan, P.; Nampoori, V. P. N.; Vallabhan, C. P. G.; Bellare, J. R. *J. Appl. Phys.* **2012**, *111*.

(178) Peng, X.; Manna, L.; Yang, W.; Wickham, J.; Scher, E.; Kadavanich, A.; Alivisatos, A. *Nature* **2000**, *404*, 59.

(179) Webber, D. H.; Brutchey, R. L. *J. Am. Chem. Soc.* **2012**, *134*, 1085.

(180) Park, J.; Joo, J.; Kwon, S. G.; Jang, Y.; Hyeon, T. *Angew. Chem. Int. Ed. Engl.* **2007**, *46*, 4630.

(181) Munro, A. M.; Jen-La Plante, I.; Ng, M. S.; Ginger, D. S. *J. Phys. Chem. C* **2007**, *111*, 6220.

(182) Munro, A. M.; Ginger, D. S. *Nano Lett.* **2008**, *8*, 2585.

(183) Kovalenko, M. V; Scheele, M.; Talapin, D. V. *Science* **2009**, *324*, 1417.

(184) Kuno, M.; Lee, J. K.; Dabbousi, B. O.; Mikulec, F. V.; Bawendi, M. G. *J. Chem. Phys.* **1997**, *106*, 9869.

(185) Liu, I. S.; Lo, H. H.; Chien, C. T.; Lin, Y. Y.; Chen, C. W.; Chen, Y. F.; Su, W. F.; Liou, S. C. *J. Mater. Chem.* **2008**, *18*, 675.

(186) Zhang, Q.; Russell, T. P.; Emrick, T. *Chem. Mater.* **2007**, *19*, 3712.

(187) Xu, J.; Wang, J.; Mitchell, M.; Mukherjee, P.; Jeffries-El, M.; Petrich, J. W.; Lin, Z. Q. *J. Am. Chem. Soc.* **2007**, *129*, 12828.

(188) Liu, J.; Tanaka, T.; Sivula, K.; Alivisatos, A. P.; Fréchet, J. M. J. *J. Am. Chem. Soc.* **2004**, *126*, 6550.

(189) Milliron, D. J.; Alivisatos, A. P.; Pitois, C.; Edder, C.; Frechet, J. M. J. *Adv. Mater.* **2003**, *15*, 58.

(190) Zhao, L.; Pang, X. C.; Adhikary, R.; Petrich, J. W.; Jeffries-El, M.; Lin, Z. Q. *Adv. Mater.* **2011**, *23*, 2844.

(191) Pentzer, E. B.; Bokel, F. A.; Hayward, R. C.; Emrick, T. *Adv. Mater.* **2012**, *24*, 2254.

(192) Zhao, L.; Pang, X.; Adhikary, R.; Petrich, J. W.; Lin, Z. *Angew. Chem. Int. Ed. Engl.* **2011**, *50*, 3958.

(193) Hammer, N. I.; Emrick, T.; Barnes, M. D. *Nanoscale Res. Lett.* **2007**, *2*, 282.

(194) Sudeep, P. K.; Early, K. T.; McCarthy, K. D.; Odoi, M. Y.; Barnes, M. D.; Emrick, T. *J. Am. Chem. Soc.* **2008**, *130*, 2384.

(195) Yu, W. W.; Peng, X. *Angew. Chem. Int. Ed. Engl.* **2002**, *41*, 2368.

(196) Dam, N.; Beerbom, M. M.; Braunagel, J. C.; Schlaf, R. *J. Appl. Phys.* **2005**, *97*, 024909.

(197) Algar, W. R.; Krull, U. J. *Langmuir* **2008**, *24*, 5514.

(198) Aldana, J.; Wang, Y. A.; Peng, X. *J. Am. Chem. Soc.* **2001**, *123*, 8844.

(199) Pilgram, K.; Korte, F. *Tetrahedron* **1965**, *21*, 1999.

(200) Scofield, J. H. *J. Electron Spectros. Relat. Phenomena* **1976**, *8*, 129.

(201) Liang, Z. Q.; Dzienis, K. L.; Xu, J.; Wang, Q. *Adv. Funct. Mater.* **2006**, *16*, 542.

(202) Katari, J. E. B.; Colvin, V. L.; Alivisatos, A. P. **1994**, 4109.

(203) Ruberu, T. P. A.; Albright, H. R.; Callis, B.; Ward, B.; Cisneros, J.; Fan, H.-J.; Vela, J. *ACS Nano* **2012**, *6*, 5348.

(204) Liu, Z.; Sun, Y.; Yuan, J.; Wei, H.; Huang, X.; Han, L.; Wang, W.; Wang, H.; Ma, W. *Adv. Mater.* **2013**, *25*, 5772.

(205) Xu, J.; Wang, J.; Mitchell, M.; Mukherjee, P.; Jeffries-El, M.; Petrich, J. W.; Lin, Z. *J. Am. Chem. Soc.* **2007**, *129*, 12828.

(206) Noone, K. M.; Anderson, N. C.; Horwitz, N. E.; Munro, A. M.; Kulkarni, A. P.; Ginger, D. S. *ACS Nano* **2009**, *3*, 1345.

(207) Sharma, S. N.; Vats, T.; Dhenadhayalan, N.; Ramamurthy, P.; Narula, A. K. *Sol. Energy Mater. Sol. Cells* **2012**, *100*, 6.

(208) Okamoto, K.; Luscombe, C. K. *Chem. Commun. (Camb).* **2014**, *50*, 5310.

(209) Mazzio, K. a; Okamoto, K.; Li, Z.; Gutmann, S.; Strein, E.; Ginger, D. S.; Schlaf, R.; Luscombe, C. K. *Chem. Commun. (Camb).* **2013**, *49*, 1321.

(210) Patil, A. O.; Heeger, A. J.; Wudl, F. *Chem. Rev.* **1988**, *88*, 183.

(211) Yu, W. W.; Peng, X. G. *Angew. Chemie-International Ed.* **2002**, *41*, 2368.

(212) Yu, W. W.; Qu, L.; Guo, W.; Peng, X. *Chem. Mater.* **2003**, *15*, 2854.

(213) Park, Y.; Advincula, R. C. *Chem. Mater.* **2011**, *23*, 4273.

(214) Nelson, J. *The Physics of Solar Cells*; Imperial College Press; 1 edition, 2003; p. 384.

(215) Nalwa, K. S.; Kodali, H. K.; Ganapathysubramanian, B.; Chaudhary, S. *Appl. Phys. Lett.* **2011**, *99*, 263301.

(216) Kuo, C.-Y.; Su, M.-S.; Chen, G.-Y.; Ku, C.-S.; Lee, H.-Y.; Wei, K.-H. *Energy Environ. Sci.* **2011**, *4*, 2316.

(217) Spadafora, E. J.; Demadrille, R.; Ratier, B.; Grévin, B. *Nano Lett.* **2010**, *10*, 3337.

(218) Koppe, M.; Egelhaaf, H.-J.; Dennler, G.; Scharber, M. C.; Brabec, C. J.; Schilinsky, P.; Hoth, C. N. *Adv. Funct. Mater.* **2010**, *20*, 338.

(219) Jasieniak, J.; Califano, M.; Watkins, S. E. *ACS Nano* **2011**, *5*, 5888.

(220) Guchhait, A.; Rath, A. K.; Pal, A. J. *Sol. Energy Mater. Sol. Cells* **2011**, *95*, 651.

(221) Liu, C.-Y.; Holman, Z. C.; Kortshagen, U. R. *Nano Lett.* **2009**, *9*, 449.

(222) Chen, H.-C.; Lai, C.-W.; Wu, I.-C.; Pan, H.-R.; Chen, I.-W. P.; Peng, Y.-K.; Liu, C.-L.; Chen, C.; Chou, P.-T. *Adv. Mater.* **2011**, *23*, 5451.

(223) Kuo, C. Y.; Tang, W. C.; Gau, C.; Guo, T. F.; Jeng, D. Z. *Appl. Phys. Lett.* **2008**, *93*, 033307.

(224) Chen, W.; Chen, Y.; Li, F.; Chen, L.; Yuan, K.; Yao, K.; Wang, P. *Sol. Energy Mater. Sol. Cells* **2012**, *96*, 266.

(225) He, L.; Jiang, C.; Lai, D.; Wang, H. *Appl. Phys. Lett.* **2011**, *99*, 021104.